Università degli Studi di Napoli Federico II

Dipartimento di Ingegneria Chimica, dei Materiali e della Produzione Industriale

Dottorato di Ricerca in Ingegneria Chimica (XXVII ciclo)

Ph.D. Thesis

Manufacture and Characterization of Nanoparticles for Energetic Applications

2012-2015

Supervisor:

Prof. ANDREA D'ANNA
Dipartimento di Ingegneria Chimica, dei Materiali
e della Produzione Industriale
Università degli Studi di Napoli Federico II

Ph.D. Student:

GIANLUIGI DE FALCO

Scientific committee:

Prof. ANDREA D'ANNA
Dipartimento di Ingegneria Chimica, dei Materiali
e della Produzione Industriale
Università degli Studi di Napoli Federico II

Dott. PATRIZIA MINUTOLO
Istituto di Ricerche sulla Combustione
Consiglio Nazionale delle Ricerche

Dott. Ing. MARIO COMMODO
Istituto di Ricerche sulla Combustione
Consiglio Nazionale delle Ricerche

CONTENTS

Abstract

It is established nowadays in combustion science and technology that every flame can produce particles, even when it appears to be particle-free. Starting from this assumption, flames are considered no longer only as a reactive flow with internal energy transfer, but also as a reactor for synthesizing gaseous and solid species. Traditional combustion aerosol technology is focused on studying nanosized particulate matter formation during combustion of hydrocarbons, considered as unwanted pollutants, in order to understand the onset of their formation and minimize their emissions. On the other hand, in flame aerosol synthesis nanoparticles are desired products, and the knowledge of their formation is the starting point to set up cheap flame reactors.

The main objective of this Ph.D. thesis is the development and control of specific aerosol flame synthesis (AFS) systems for the production and the subsequent characterization of engineered nanomaterials. The work was focused on metal oxides based nanomaterials, carbonaceous nanomaterials and carbon-metal oxides nanocomposite.

The flame reactors used for the synthesis of carbon nanomaterials were constituted by undoped flat laminar ethylene/air premixed flame, operated in fuel-rich condition, in which vapor carbon precursors are given by the unburned fuel. Different carbonaceous particles were produced by changing flame equivalent ratio and particle residence time (i.e, sampling position). Properties of synthesized nanoparticles, such as 2D/3D character, optical features, chemical structure, electrical behavior and interaction forces, were characterized with respect to the flame reactor characteristics.

Regarding the production of metal oxides nanoparticles and carbon-metal oxides nanocomposites, an Aerosol Flame Synthesis (AFS) system was developed and successfully operated in VAFS mode to produce pure, monodisperse nanoparticles of magnesium oxide and titanium dioxide, by feeding magnesium and titanium precursors to a fuel-lean hydrocarbon flame reactor.

Finally, the AFS system was operated in fuel-rich flame reactor conditions, in order to synthesize pure TiO_2 and carbon-TiO_2 nanoparticles with similar dimension and compositions. A characterization of nanoparticle health effects, for personal care products applications, in terms of Reactive Oxygen Species (ROS) production was performed, showing that flame-synthesized titania produces a lower amount of ROS with respect to commercial TiO_2. The presence of carbon induces a further decrease of ROS production, leading to a reduction of nanopowder skin toxicity.

1. Introduction: nanomaterials and nanotechnology

In its broadest definition, nanotechnology refers to the production, development and use of materials, structures and devices that range in size from 1 to hundreds of nanometers. This term can be applied to many areas of research and development, from medicine to manufacturing and computing, and even to textiles and cosmetics (Pagliaro, 2010). Even though interest and investments from researchers and industries have grown faster during the last 30 years, leading to significant advantages in nanomaterials knowledge, nanotechnology can be considered yet a not-fully explored field.

The most attractive behavior that nanostructured materials exhibit are their size-effects, i.e., changes in properties compared to the bulk material. As an example, gold is usually a chemically inert material, but it can be used as an excellent catalyst if produced as 1-5 nm particles (Roth, 2007). The reason for these size effects is the excess of surface area, due to the reduced dimensions, with respect to the bulk material. For a 4 nm particle, half of the molecules forming the nanostructure are actually at the surface, altering the lattice structure (Sardar et al., 2009). This is the cause of dramatic changes in physical and chemical properties, such as melting temperature, mechanical, magnetic and optical properties, optical band gap for semiconducting particles, as well as catalytic behaviors. The main goal is then the production of particles with a very narrow size distribution and well controlled phase composition and morphology, called “functional nanoparticles” (Sardar et al., 2009).

Nanoparticles are prepared mostly by wet-phase chemical methods or gas-phase (aerosol) processes (Camenzind et al., 2010). The former methods include hydrothermal synthesis, precipitation route and sol-gel synthesis. These offer a good control on polidispersity, resulting in perfect monodisperse particles (Hyeon et al., 2001), but they usually need various post-treatment steps (Schwartz, 1995). Compared to wet-chemical routes, gas-phase methods provide a direct and continuous process with few waste and by-product generation. Furthermore, they offer easier collection of particles from gases than from liquids, and any further post-processing is required. Aerosol methods include plasma and laser reactors, gas-condensation methods and laser ablation (Minterer, 2002), hot-wall reactors (Okuyama and Lenggoro, 2003) and flame aerosol reactors.

1.1. Flame aerosol synthesis

It is established nowadays in combustion science and technology that every flame can produce particles, even when it appears to be particle-free. Starting from this assumption, flames are

considered no longer only as a reactive flow with internal energy transfer, but also as a reactor for synthesizing gaseous and solid species (Roth, 2007). Traditional combustion aerosol technology is focused on studying nanosized particulate matter formation during combustion of hydrocarbons (Bockhorn, 1994), considered as unwanted pollutants, in order to understand the onset of their formation and minimize their emissions. On the other hand, in flame aerosol synthesis nanoparticles are desired products, and the knowledge of their formation is the starting point to set up cheap flame reactors for the production of nanomaterials with specific physical properties (Strobel and Pratsinis, 2007).

Unlike other gas-phase processes, flame synthesis does not involve an external source of energy (such as plasmas, lasers or electrically heated walls). Indeed, energy is generated in-situ by combustion, driving precursor conversion to particle, and is then rapidly removed by radiation and convection. Temperature in flame reactors are usually higher than those found in hot-wall, evaporation-condensation and laser reactor, and residence times are shorter. Also, low cost precursors can be used, and systems are simple and relative inexpensive to build and operate. These features make flame synthesis a cheap and continuous process with proven scalability (Pratsinis, 1998).

1.2. Mechanisms of particle formation in flames

Flame-made nanoparticles are formed by gas-to-particle conversion route of appropriate precursors injected into the unburnt gases either in the gaseous state or as liquid droplets (Li et al., 2010). When fed as liquid droplets, precursors quickly evaporate due to the temperature increase in the fluid flow deriving from the exothermic oxidation reactions. Heat of combustion then starts decomposition reactions of vapor precursors, which can also interact with the kinetics of the combustion process and form product molecules. These monomers subsequently undergo homogeneous nucleation phenomena, and generate the first nuclei (i.e., the first solid species), which can grow by two different mechanisms: addition of molecules to their surface by condensation (usually labeled as heterogeneous nucleation) and gas kinetic collisions due to their Brownian motion. This pattern is usually identified as inception, and the result is the formation of nearly spherical primary particles. The typical time scale of the inception phenomena is usually shorter than the time scale of the subsequent particles evolution (Roth, 2007). Such primary particles continue to develop, forming larger structures by surface growth, due to chemical reaction and condensation of vapour phase compounds on the surface of primary particles, and by coagulation phenomena. Coagulation of colliding particles can occurs either as full coalescence, i.e., sintering of two primary particles forming a larger spherical particle in which they are no longer identifiable, or as aggregation of primary particles, stuck together preserving their identity. Particle sintering is favored by high temperature and

small particles diameter. As temperature drops down and particles grow in size, their sintering stops, leading to agglomeration of particles. Processes involved in particle formation in flames are schematically showed in Figure 1.1.

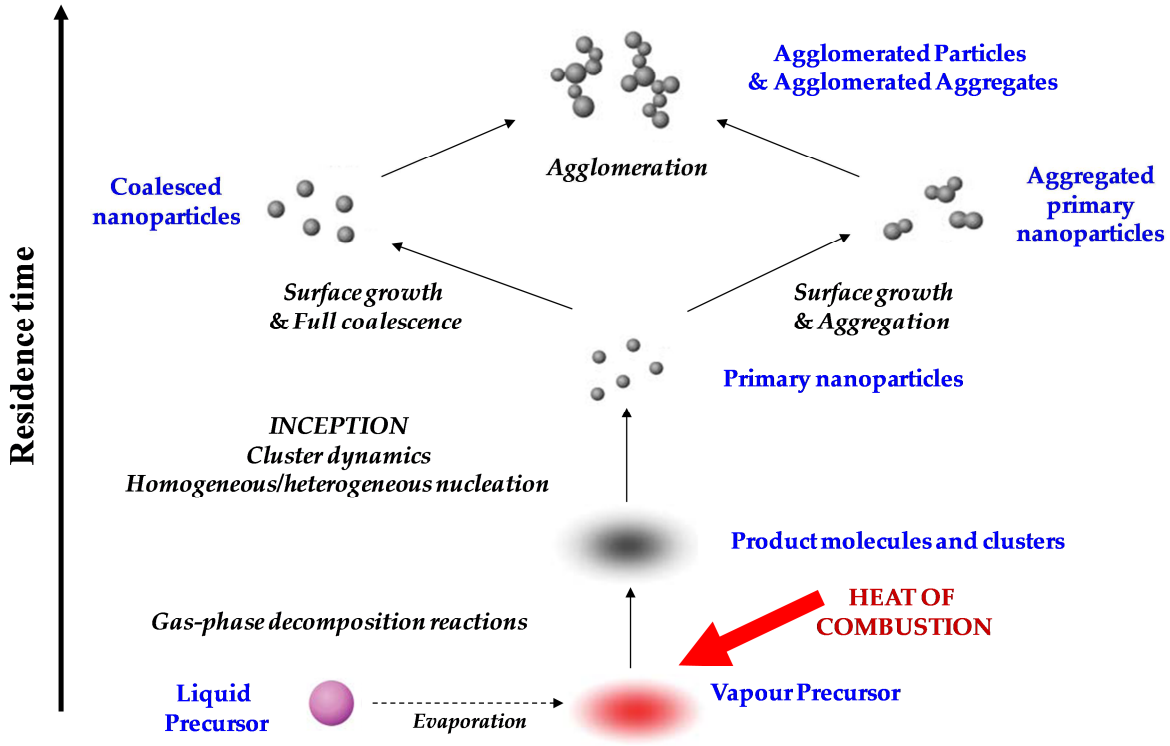

Figure 1.1. Schematic of particle formation mechanism in flames (adapted from Strobel and Pratsinis, 2007 and Roth, 2007).

Characteristics nanoparticles reflecting their performances are: size, morphology, shape, crystal structure and phase-mixing. In the case of flame-made nanoparticles these properties are affected by the concentration of precursors and the combined influence of flame temperature (and hence particles temperature) and residence time of the particles (Strobel and Pratsinis, 2007). The influence of these key parameters can be summarized following the simplified schematization reported by Roth (2007):

- an increase of precursor concentration lead to an increase of primary particle size;
- an increase of temperature inside the reactor leads to an increase of precursor decomposition, thus to a sub-sequential increase in monomer formation rate;
- an increase of temperature inside the reactor also lead to higher coalescence rate, with finally production of smaller primary particles;
- the formation of compact spherical particles is favored by high temperature and short residence time;

- the formation of highly structured agglomerates is favored by low temperature and long residence time.

2. Flame synthesis of nanoparticles: state of the art

2.1. Inorganic nanoparticles

Flame aerosol technology for the production of inorganic nanoparticles is used nowadays to realize a large variety of commodities (Stark and Pratsinis, 2002) such as: titania (2 Mt/year) is mainly used for pigments and as ultra-violet light photocatalyst. Zinc oxide (0.6 Mt/year) is an activator of rubber vulcanization and a pharmaceutical additive. Fumed silica (0.2 Mt/year) is a powder flowing aid in cosmetics and pharmaceutical industries. Fumed alumina is used as solution for chemical mechanical polishing in microelectronics (SRI International, 2001).

Development of flame reactors started in the second half of the 20th century. Fumed silica was the first flame-made materials, produced by Degussa in the 1940's and marketed as Aerosil (Pratsinis, 1998). In the early 1970's, Degussa realized the first flame-made TiO_2-based photocatalyst, labeled as P-25. A decade later, Ulrich was the pioneer in the academic research on ceramic powders by making SiO_2 powders through $SiCl_4$ oxidation in premixed flames (Ulrich, 1984). In 1991, Zachariah and Huzarewicz proposed a diffusion flame configuration for synthesizing high-temperature superconducting particles of yttrium-barium-copper oxide. Thereafter, different flame processes were studied and developed, especially for heterogeneous catalytic materials, such as ceria-based catalyst (Mädler et al., 2002), zinc oxide photocatalyst (Jang et al., 2006) and perovskites (Chiarello et al., 2005). Titanium dioxide-based nanomaterials for semiconducting gas sensors have been prepared by flames (Sahm et al., 2004; Teleki et al., 2006). Flame synthesis was successfully used to realize nanocomposites such as carbon-coated copper nanoparticles for optical humidity sensors (Athanassiou et al., 2006), silica-ytterbium oxide mixture incorporated into a polyacrylate matrix for dental industry (Mädler et al., 2006) and solid solution of CeO_2–GdO_2 for solid oxide fuel cells (SOFC) (Seo et al., 2006).

2.1.1. Reactor configurations for metal oxide nanoparticles production

Different aerosol reactors and methods based on combustion have been developed during the last decades for the production of a wide variety of metal and metal oxide nanosized particles. Flame reactors can be classified according to the state and the enthalpy content of the supplied precursors (Strobel et al., 2006) when they reach in the flame front.

Vapor-fed aerosol flame synthesis (VAFS) is the combustion of volatile metal precursors (e.g., chlorides) in a hydrocarbon or hydrogen flame. Precursors form small particles by nucleation

from the gas phase, which then can grow by surface reaction, coagulation and sintering (Fig. 1.1), as described in section 2.1. VAFS is a very simple and scalable process (Wegner and Pratsinis, 2005), and it is still used industrially for the manufacture of several commercial nanoparticles, but is limited by the need of cheap volatile precursors.

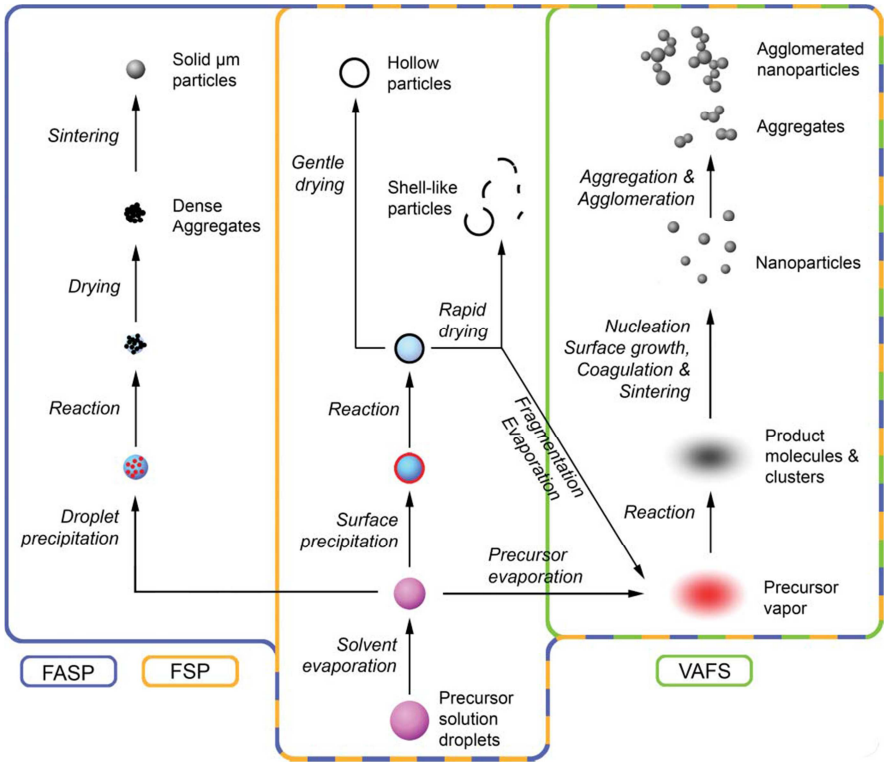

Figure 2.1. Schematic of particle formation during FSP, FASP and VAFS (Strobel and Pratsinis, 2007).

In liquid-fed aerosol flame synthesis (LASF) a non-volatile liquid precursor solution is delivered as fine, monodisperse droplets. This configuration is much more versatile with respect to VAFS, since non-volatile precursors can be supplied. LASF is called flame spray pyrolysis (FSP) if the precursor solution is a combustible liquid that is sprayed and ignited, driving the flame process (Strobel and Pratsinis, 2007). If the precursor solution is a combustible or a non-combustible liquid fed into an external flame, used as a heat source, LASF is called flame-assisted spray pyrolysis (FASP). When complete precursor evaporation occurs, solid nanoparticles are formed following the same patterns as in VAFS. On the other hand, incomplete droplet evaporation and precursor precipitation could lead to the formation of hollow nanoparticles, shell-like and micron-sized particles (Fig. 2.1).

2.1.2. Titanium dioxide nanoparticles

Among several materials produced by flame synthesis, titanium dioxide TiO_2 can be considered as one of the most important and, more generally, as one of the most used materials in the modern era, since it is suitable for a large number of applications in several different fields. As bulk material, TiO_2 is produce in the order of millions of tons per year, and it is mainly used as a white pigment in plastics and paintings. As a nanomaterial, its unusual properties entail a wide range of applications (Kamat, 2012), which span from photocatalyst for water splitting and air purification (Ni et al., 2005) to food color additive and component in personal care products (Weir et al., 2012).

A huge number of flame synthesis configurations have been used over the years to produce titanium dioxide nanostructures, showing that the experimental set-up and the operating conditions can be varied to gain a control on crystalline phase, size and morphology of synthesized nanoparticles.

Formenti et al. (1972) reported first the production of titania by oxidation of $TiCl_4$ in an oxygen–hydrogen diffusion flame reactor and the dependence of precursor concentration and residence time on particles size (10–200 nm) and morphology.

Hung and Katz (1992) observed the formation and growth of primary titania particles (10-60 nm) through collision and coalescence in a counter flow diffusion flame of hydrogen and oxygen.

Pratsinis et al. (1996) investigated the effect of different C_2H_4/Air co-flow diffusion flame configurations on the properties of TiO_2 particles and found that a better mixing of oxidant and precursor results in a decrease of particle size and an increase of anatase phase content.

Vemury and Pratsinis (1995) employed a co-flow diffusion flame reactor in the presence of a gaseous electric discharge (corona) for the synthesis of ultrafine primary particle with controlled size and cristallinity. Lately, Yeh et al. (2004) studied the formation of titania nanoparticles in premixed flame using titanium tetraisopropoxide (TTIP) as precursor. They reported the increase of anatase phase content with increase in oxygen concentration. On the other hand, rutile phase content was found to increase with both particle residence time and fuel equivalent ratio from 0.7 to 1.0, the latter causing an overall rise in flame temperature which, in turn, favors the anatase-to-rutile phase transformation.

Wegner and Pratsinis (2003) developed a critical-flow nozzle method for the collection of titania nanoparticles from a CH_4/O_2 co-flow diffusion flame, using TTIP as precursor. They showed that the position of the quenching nozzle can enable precise control of both the anatase content from 5 to 97 wt % and the particle size from 5 to 60 nm.

More recently, a premixed stagnation flame reactor was employed by Zhao et al. (2005), burning an ethylene-oxygen-argon mixture with TTIP. Starting from this configuration, Tolmachoff

et al. (2009) proposed an innovative method, called flame stabilized on a rotating surface (FSRS), for the synthesis and deposition into a thin film of TiO_2 nanoparticles in a single step. This method was successfully applied to prepare mesoporous film of titania nanoparticles for applications as CO sensor (Tolmachoff et el., 2011), and photoanode into dye sensitized solar cells (Nikraz et al., 2012). Tolmachoff et al. (2009) proposed a premixed stagnation swirl flame configuration for the synthesis of anatase particles with an average diameter of 5–10 nm. The growth of highly crystalline TiO_2 nanoparticles (20–35 nm) with tunable polymorphic content by rapid flame spray pyrolysis was demonstrated by Kho et al. (2011).

2.2. Carbonaceous nanoparticles

Carbon black is probably the most prominent example of carbonaceous flame-made material, and at the same time the first kind of particles produced by flame in mankind's history, since it was already used for drawings in caves during prehistoric age.

More recently, flame synthesis have been widely adopted for fullerene production, since it was discovered and isolated in 1985 by Kroto et al. The peculiar physical properties of fullerenes allow them to be used for several applications, including superconductors, sensors, catalysts and organic solar cells. Flame can easily provide both the high temperature and the hydrocarbon reactants for fullerenes synthesis. In order to have high yields low pressure conditions, a rich equivalence ratio close to stoichiometric are used, starting from precursors like highly unsaturated hydrocarbons such as acetylene and benzene (Pope et al., 1993).

The diffusion of carbon nanotubes (CNTs) came just after fullerenes discovery (Iijima, 1991). Flame configurations for CNTs involve the use of a metallic catalyst on which nanotubes grow, starting from many different fuels in both premixed and diffusion flames (Vander Wal, 2000).

Recently, great attention has been given by the scientific community to graphene during the last years, due to its unique two-dimensional structure (Novoselov et al., 2005). Since graphene is younger than the other related materials, growth mechanisms that can lead to the formation of isolated and stable graphene sheets in flame are not yet well understood, but some flames synthesis method for graphene films are already available (Memon et al., 2013a).

Finally, an additional class of nanomaterials produced in flames is constituted by combustion-generated solid particulate matter, which comprises solid nanocompounds resulting from incomplete combustion conditions. Those compounds are mainly produced in fuel-rich flames, defined as flames burned with an amount of fuel exceeding stoichiometric conditions, and characterized by a flame equivalent ratio (Φ), i.e., the ratio of the fuel-to-oxidizer ratio to the stoichiometric

fuel-to-oxidizer ratio, higher than one. The study of particulate matter formation in combustion systems has led to several progresses during the last decades (Jander and Wagner, 2009). Modeling and experimental activities have demonstrated that fuel-rich flame conditions produce particles with a wide size range roughly grouped, on the basis of the bimodal shape of the size distribution function, in two classes of nanoparticles (Bockhorn, 1994; Sgro et al., 2003; D'Anna, 2009a; Echavarria, et al. 2009; Wang, 2011; Commodo et al., 2013). In addition to their sizes, these two classes of particle differentiate by chemical structure, morphology, optical and spectroscopy behaviors.

The first class of particles, which are usually referred to as organic carbon nanoparticles (NOC), has a mean size approximately in the range 2-4 nm which remains almost constant changing the fuel equivalence ratio and the flame residence time, and possesses intermediate properties between gas-phase compounds and solid particles. These particles have molecular-like spectroscopic behavior, absorbing in the Ultra Violet region and giving a fluorescence signal when excited with a laser source (Commodo et al., 2007). Their structure is likely a composite of aromatic rings liked together by aliphatic bonds (D'Alessio et al., 2009), with an hydrogen/carbon ratio ranging from 0.5 to 1. Due to their chemical composition and morphological arrangement, these particles are partially soluble in water, and soluble in some organic solvents, such as dichloromethane.

The second class of particles has a mean size which shifts from about 4-10 nm to 10-100 nm and more as the flame equivalence ratio and the flame residence time are increased. The larger size particles, those with sizes in the range 10-100 nm, are usually referred to as soot particles. They are prevalently composed by large aromatic carbon compounds (Haynes and Wagner, 1981). Other principal constituents are oxygen and hydrogen, with a hydrogen-to-carbon ratio ranging from 0.05 to 0.33. Soot particles are characterized by a turbostratic internal disposition for the aromatic planes, similar to that of graphite, with a larger interplanar spacing (soot ~ 0.35-0.5 nm, graphite ~ 0.33 nm), due to internal structure defects that leads to less ordered spatial disposition. Soot particles absorb light in the visible, are insoluble in water and in main organic solvents.

Soot particles are formed in quite fuel-rich flame conditions characterized by a strong yellow-red luminosity (sooting fuel-rich flames, $\Phi > 2.1$). Carbon nanoparticles with equivalent diameter of about 2-4 nm (NOC) are generated both in sooting conditions, where they coexist with larger primary soot particles and soot aggregates, and in less fuel-rich bluish flame conditions (non sooting fuel-rich flames, $1.7 < \Phi < 2.1$), where they are formed alone or coexist with the larger 4-10 nm particles (Dobbins 2007; Maricq 2004; Maricq 2005; Commodo et al., 2014). Nascent particles were reported to be liquid-like or bi-dimensional structures which assume an atomically thin disk-like shape when deposited on a substrate (Abid et al. 2008; Dobbins 2007; Barone et al. 2003; Minutolo et al. 2014).

The mechanisms of carbon particle formation flame are schematically represented in Figure 2.2. Gas-phase precursors of freshly nucleated nano-sized particles have been identified in polycyclic aromatic hydrocarbons (PAHs) (Richter et al. 2005; Sirignano et al., 2010). PAHs are subjected to molecular mass growth in the post-flame region, leading these molecules to form larger structure. These structures are later transformed into incipient organic nanoparticles through a molecule-to-cluster nucleation process. When they assume a three dimensional shape, they stop to behave like gas-phase species and start to exhibit properties typical of condensed phases, e.g., density, viscosity, plasticity. The exact dynamic of the inception mechanism is still debated (Wang, 2011), and probably represents the less understood step in the soot formation route.

Once the first clusters/particles are nucleated, a series of high-temperature chemical and physical processes lead to particle mass/size growth, and chemical transformation (D'Anna, 2009b).

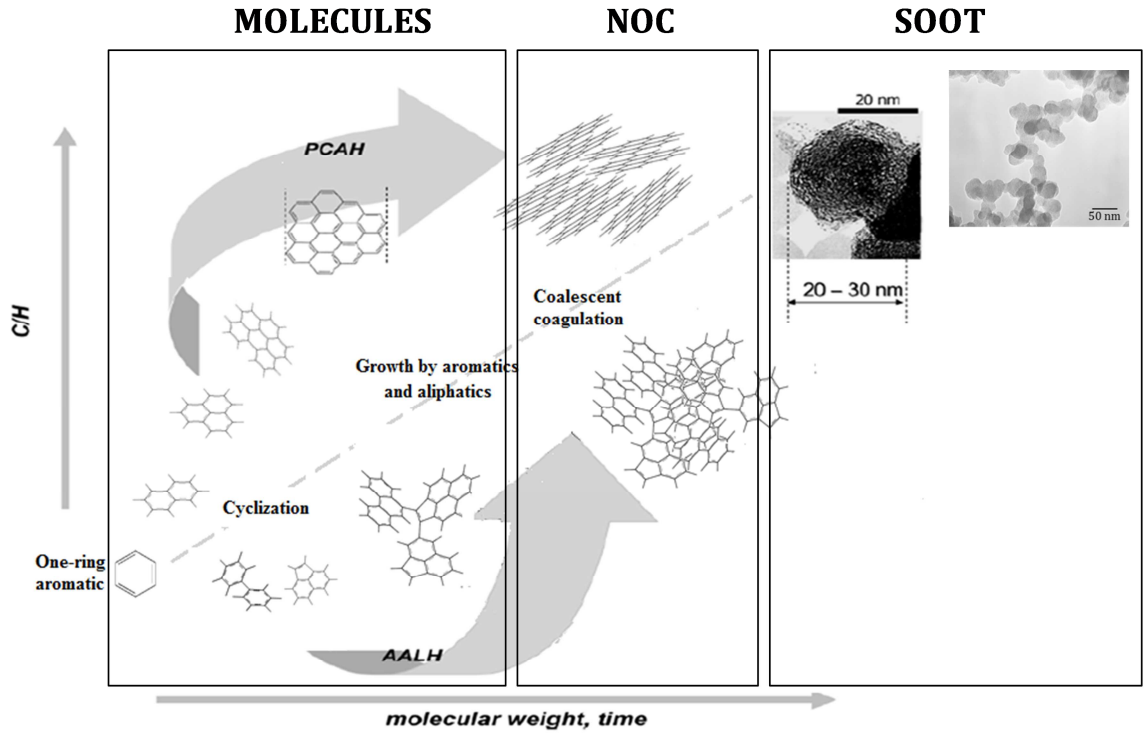

Figure 2.2. Schematic of carbon particles formation routes in flame (adapted from D'Anna, 2009b).

Soot formation in flame is a well-studied process and involves all the particle formation pathways in flames showed in Section 1.2, unless some differences occurring to carbonaceous particles like internal structure rearrangements and surface oxidation. As a matter of fact, understanding of particle dynamics and particle diagnostics and their interaction with the fluid flow mostly comes from studying soot formation (Roth, 2007).

2.2.1. Fuel-rich flames as materials synthesis reactors

Combustion-generated solid particulate matter is generally considered as unwonted by-products of energy production and significant atmospheric pollutant. Several studies have been conducted, during last decades, on the chemical-physical mechanisms responsible for the formation of carbon compounds in flames (D'Anna, 2009a; Wang, 2011), with the aim of improving the combustion efficiency and reducing the emission of pollutants from combustion devices. Since such species have many features similar to carbon compounds used in new technologies (fullerene, graphite, carbon blacks and so on), fuel-rich flames can be considered, from material science and engineering point of view, as challenging reactors for the production of large variety of carbon nanostructures. The deeply knowledge that has been gained on the key steps controlling the formation and growth of such species can be a starting point to develop new synthesis routes for specific and tailored carbonaceous structures designed for innovative technologies.

2.3. Carbon-metal oxides nanocomposites

The coating and/or the modification of metal oxides nanoparticles with carbon is a field of great interest, since nanoparticle properties like electrical conductivity, dispersibility in polymers, opacity, UV protection and so on can be substantially modified by carbon adding. These products are typically produced by separate synthesis of the nano-oxide and the carbon particles, followed by mixing of the two powders (Kammler and Pratsinis, 2003). Flame technology is an alternative route for the synthesis of nanocomposite products, furnishing a closely control on composition and properties without involving multiple steps like wet-chemical methods and long processing time like solid state reaction methods (Pratsinis, 1998).

The production of carbon-silica particles, for example, has been extensively studied during last decades, since they are used as reinforcing agent for rubbers (Francis et al., 1996), and precursor powder for production of silica aerogels and silicon carbide (Koc and Cattamanchi, 1998). Regarding flame synthesis method, carbon-coated silica nanoparticles were produced in acetylene/$SiCl_4$ premixed flames by Spicer at al. (1998). Kammler et al. (2001) synthesized silica-carbon particles with carbon content up to 5 wt. % in a ring-shaped double-diffusion flame of hexametyl disiloxane and oxygen at production rate up to 130 g/h.

More recently, a great deal of attention has been paid to the production of carbon-titania structure, since the coating of TiO_2 surface with carbon can improve the absorbance in the visible region, and so the photocatalytic efficiency. A number of methods that do not involve flame synthesis have been used to prepare carbon-titania nanoparticles, such as heating commercially available titania in a furnace at 800 °C together with glucose (Zhang et al., 2008). However, as stated before,

the key advantage of developing a flame synthesis system is the possibility to have a one-step process for both the TiO_2 nanoparticles synthesis and the carbon coating. Khan et al. (2002) first reported the growth of carbon-modified rutile TiO_2 by the combustion of Ti metal in natural gas, which resulted in increased photocatalitic efficiency for water splitting. Kammler and Pratsinis (2003) reported the growth of TiO_2 coated with carbon in an acetylene diffusion flame, using TTIP as the precursor. This configuration allowed a control in a wide range of both particle surface area and phase composition. Bhanwala et al. (2009) reported the growth of carbon-coated titania in a liquid petroleum gas (LPG) laminar diffusion flame, using titanium chloride ($TiCl_4$) as the precursor. The flow rate of LPG showed to have a strong influence on particle surface area, phase composition, and average particle size. Memon et al. (2013b) first used a multi-element diffusion flame burner (MEDB) for studying the growth of pure anatase and carbon-coated titanium dioxide using hydrogen, oxygen and argon to establish the flame, whereas titanium tetraisopropoxide was used as the precursor. They found that the growth of highly crystalline TiO_2 nanoparticles is dependent on the gas flow rate of the precursor carrier and carbon coating occurs only on crystalline nanoparticles.

3. Aim and contents of the thesis

The main objective of this Ph.D. thesis is the development and control of specific aerosol flame synthesis (AFS) systems for the production and the subsequent characterization of engineered nanomaterials. The work was focused on metal oxides based nanomaterials, carbonaceous nanomaterials and carbon-metal oxides nanocomposite.

Several diagnostic techniques were chosen to perform the characterization of synthesized nanomaterials properties, as described in Paragraph 4.3.

Particle size distributions were investigated by differential mobility analyzer (DMA) and electrical low pressure impactor (ELPI), which are two on-line techniques that do not require the preventive knowledge of any particle properties.

Atomic Force Microscopy (AFM) was used to investigate particle size and morphology in addition to Scanning Electron Microscopy (SEM) imaging. . Furthermore, AFM is also a powerful tool for several spectroscopic techniques, like Force-Distance Spectroscopy, which has been herein employed for the first time on combustion-generated nanoparticles to gain surface properties information.

Furthermore, spectroscopy methods were utilized to explore the crystalline phase composition of synthesized inorganic nanoparticles (X-Ray diffraction, XRD), the nanostructure of carbon materials and the phase composition of inorganic materials (Raman Scattering) and the light absorption and band gap features of both organic and inorganic nanoparticles (UV-Vis Absorption).

A four probe technique based on a picoammeter/voltage source allowed to carry out I-V measurements for the characterization of flame-formed carbonaceous nanoparticle electrical properties.

The flame reactors used for the synthesis of carbon nanomaterials were constituted by undoped flat laminar ethylene/air premixed flame, operated in fuel-rich condition, in which vapor carbon precursors are given by the unburned fuel (Paragraph 4.1). Referring to ethylene/air flames, previous experiences on the characterization of combustion-generated particles showed that flames with equivalent ratio $\Phi < 1.90$ ($C/O < 0.63$) produce unimodal size particles, with mean diameter of about 2.5 nm. In these flame conditions, particle inception occurs near the flame front, and coagulation and surface growth phenomena are not yet present. As equivalence ratio increases, particle-particle coagulation became relevant and mean particle diameter slightly increase, even though it is still unimodal. Finally, in fuel richer conditions, usually stated as sooting conditions, particle dynamics is largely controlled by coagulation. Unimodal size particles are measured just in inception region; at higher residence times, when particle size had grown larger than 7 nm, size distributions

are bimodal, and persistent nucleation phenomenon can be observed. Such background knowledge has represented the basis to select appropriate flame conditions for the flame synthesis of different carbon nanostructure, whose results are reported in Chapter 5.

Particularly, the synthesis of atom-thick planar nanostructures, that we defined carbon 2-D nanodisks, is presented in Paragraph 5.1, together with their characterization in terms of morphology and size, by means of AFM and DMA, and chemical and internal structure, by means of Raman spectroscopy. Paragraph 5.2 reports the results of the synthesis of flame-formed carbon nanoparticles (FFCNPs) in different sooting flame conditions (from slightly to fully sooting), moving to equivalence ratios larger than those relative to the carbon nano-disks synthesis conditions. The dependence of their chemical composition and optical properties, by Raman spectroscopy and UV-Vis absorption, with respect to their electrical conductivity was investigated. The understanding of such properties can be fundamental in conductometric sensors for particulate matter detection and also to calibrate these sensors on the different FFCNPs classes. Paragraph 5.3 describes the synthesis of a wide pool of FFCNPs from different flame conditions (from non-sooting to fully sooting), which were then characterized in terms of morphology and surface properties (interaction forces and Hamaker constant), with the aim to better understand the role played by coagulation in their formation routes, and to gain a control of the stacking of graphitic planes during FFCNPs synthesis process. A technique based on AFM force spectroscopy, a new tool in the field of combustion, was used.

Regarding the synthesis of inorganic nanomaterials, a specific aerosol flame synthesis system was manufactured by combining a droplet generator and a honeycomb burner (Paragraph 4.2) similar to the burner realized by Arabi-Katbi et al. (2002), adopting an experimental configuration previously developed in our laboratories by Carbone (2010) and Carbone et al. (2011). This flame reactor configuration is based on the addiction in laminar premixed flames of appropriate precursors dissolved into solvents, and allows to operate in both vapour-fed aerosol flame synthesis mode and flame-assisted spray pyrolysis mode. The main advantage is that a wide range of precursors with different features can be used (volatile, nonvolatile, solid, liquid), and also the effect of precursor state on particles formation can be investigated. Moreover, the system can be operated in safety condition, and it possible to switch from one kind of nanomaterials to another, by simply changing precursor and/or solvent, keeping constant the main features of the flame in which they are fed. The AFS system was operated in fuel-lean conditions to produce ultra-fine, monodisperse nanoparticles of magnesium oxide and titanium dioxide, which were then characterized in terms of size, morphology, crystal structure and optical properties. Obtained results are reported in Chapter 6.

Finally, the designed AFS system was also operated in fuel-rich conditions, with the aim to

synthesize both pure titania nanopowder and carbon-titania nanopowder for application in personal care products, from two experimental flame conditions with very similar parameters and very similar residence times, by only varying the global equivalent ratio Φ, and so the amount of carbon available in the system. Chapter 7 describes the operating flame conditions, and the characterization of particle phase composition by XRD, particle carbon content by Raman spectroscopy, particle size and morphology by AFM and SEM and particle optical properties by UV-Vis Absorption. An analysis of reactive oxygen species (ROS) production was performed, in order to investigate the possible reduced health effects in terms of ROS production given by the addition of carbon to titania nanopowder.

4. Experimental apparatus and diagnostics

4.1. Premixed laminar flame reactor

For carbonaceous nanoparticles synthesis, a premixed flat laminar flame at atmospheric pressure, generated on a commercial burner, is used as reactor. In this configuration, fuel and oxidant are mixed before the flame front, and the maximum temperature value is reached after a preheating zone, and then post-combustion zone starts. Laminar premixed flame is a one-dimensional reactor, whose characteristics correspond to those of a plug flow reactor PRF. It is possible to assume an absence of gradients in radial direction (perpendicular to the gas flow), and so spatial coordinate univocally corresponds to particle residence time in flame. The burner is a McKenna type (Fig. 4.1), able to produce flat and high-stable flames, with a porous plug of 60 mm in diameter and a forced water circulation cooling system, allowing to stabilize flames with several cold gas velocities and equivalence ratios. A further device used to improve the stability of the flame is the so-called stabilization plate, positioned at a certain height above the burner.

Figure 4.1. Picture of McKenna type flame reactor.

4.2. Aerosol flame synthesis system

The Aerosol Flame Synthesis (AFS) system realized for the production of metal oxides nanoparticles and carbon-metal oxides nanocomposites was obtained by combining a droplet genera-

tor and a honeycomb burner, adopting an experimental configuration previously developed in our laboratories by Carbone (2010) and Carbone et al. (2011). A scheme of the AFS system is illustrated in Fig. 4.2.

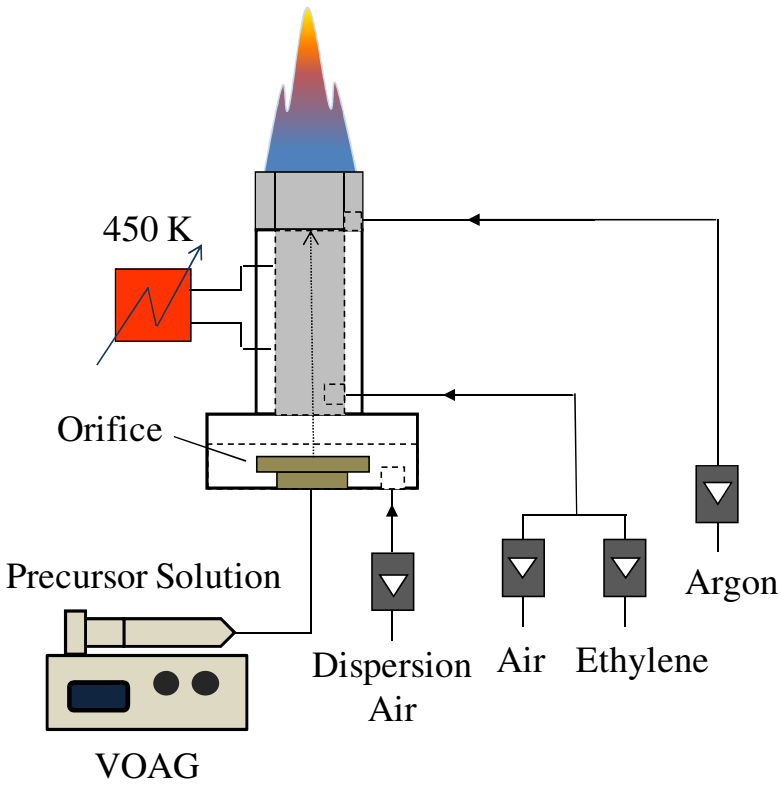

Figure 4.2. Experimental configuration of AFS system.

The aerosol generator is a Berglund Liu type Vibrating Orifice Aerosol Generator (VOAG), model 3450 manufactured by TSI. VOAG can produce a high quality monodisperse aerosol of known particles size and concentration from any material which is in form of solution (TSI, 2002). It is constituted by a syringe pump, an orifice and a signal generator; the solution is sent from the syringe pump through the orifice, in order to generate a cylindrical liquid jet. The signal generator applies a periodic disturbance of an appropriate frequency to the orifice disc, inducing a controlled break-up in the liquid jet that generates droplets of uniform size. Droplets diameter can be adjusted by varying the orifice oscillation frequency, the syringe run speed and the orifice diameter. Droplets jet is dispersed into an air stream and injected directly into the burner, an 18 mm inside diameter (ID) stainless steel tube; a 26 mm long Mullite Zirconia Honeycomb (400 CPSI) is placed on its top, and it is used to stabilize the flame and homogenously feed the aerosol (see Fig. 4.3). The burner had an outside ring (ID 24 mm, OD 34 mm) used to flow sheath Argon to isolate the flame from the surrounding air. This honeycomb burner is quite similar to that used by Arabi-Katbi et al. (2002), and allows the realization of a perfect plug flow.

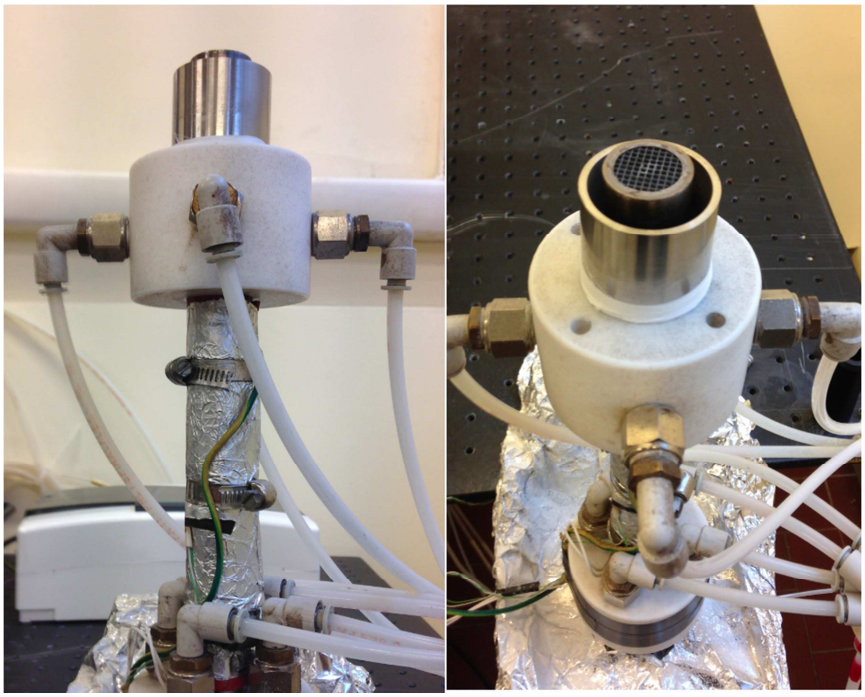

Figure 4.3. Picture of the honeycomb burner.

As mentioned above, the system is designed to work both as vapour-fed aerosol flame synthesis reactor and flame-assisted spray pyrolysis reactor. The burner is equipped with electrical resistances controlled by a proportional-integrated controller, whereby burner's walls can be heated up to 450 K. If the heat controller system is switched on, precursor solution droplet evaporate into the burner before reaching the flame front, and so the reactor works in VAFS operation mode. On the contrary, if the heat controller system is switched off, precursors solution droplet reach the flame front in the liquid state, and evaporation starts inside the flame, so reactor works in FASP operation mode.

4.3 Experimental techniques and sampling methods for particle characterization

4.3.1. Differential mobility analyzer

The Differential Mobility Analyzer (DMA) is an on-line real time detection system used to determine the size distribution of charged particles, classified according to their electrical mobility. The electrical mobility (Z) is defined to be the ratio between the speed (u) of a charged particle in a gas, induced by an electric field E, and the electric field itself.

$$\vec{u} = Z \cdot \vec{E} \tag{4.1}$$

The relationship between particles electrical mobility and diameter, in the size range below 5 nm, was the subject of many theories existing in literature, all assuming particles spherical shape (Makela et al., 1996). Typically, the diameter reported in size distributions obtained from electrical mobility measurements is the mobility diameter d_M, which is calculated from the well-known Millikan-Fuchs equation:

$$Z = \frac{q \cdot e \cdot C_c}{3 \cdot \pi \cdot \mu \cdot d_M} \tag{4.2}$$

Where q is the number of charges in the particle, e is the unit charge and μ is the viscosity of the carrier gas. The Cunningham factor C_c is a function of the Knudsen number (Hinds, 1999). Anyway, experimental results showed that the Millikan-Fuchs theory falls in predicting the electrical mobility for d_M smaller than 5 nm (Fernandez de la Mora et al., 1998). So, in this thesis work, the size distributions was calculated in terms of the volume equivalent diameter, d, calculated from the electrical mobility, Z, measured by DMA in a sheath flow of a carrier gas with molecular mass, m, temperature, T and pressure, p, using the following semi-empirical equation (Fernández de la Mora et al., 1998; Sgro et al., 2011):

$$Z = 0.441 \frac{q \cdot \left(\frac{kT}{m}\right)^{0.5}}{p(d_0 + d_M)^2} \tag{4.3}$$

Where d_0 is an effective diameter of the gas molecules in which the aerosol is immersed (d_0 = 0.5 nm for air at 273 K).

DMA is generally constituted by three components: a neutralizer, an electrostatic classifier and a detector. The neutralizer provides to charge particles with a known steady state charge distribution, which are then selected with respect to their electrical mobility in the electrostatic classifier, and divided into different monodisperse aerosols. The detector is used to count the number of particles per unit volume of each monodisperse aerosol. A Condensation Particles Counter (CPC), based on an optical counting of particles, or an Electrometer, that is a very sensitive ampere-meter which directly measure the charges, can be used as detectors.

The Differential Mobility Analysis system used for this research activity was a TapCon 3/150 Wien Type, equipped with a bipolar radioactive (Am-241) diffusion charger and a DMA 3/150, characterized by a wide range of applicable aerosol (1-10 L/min) and sheath gas flows (10-50 L/min); with the aerosol flow at 5 L/min and the sheath flow at 50 L/min, the particle size regions achieved by the instrument are 0.6-28 nm and 2-100 nm with high voltage respectively at 1250 V and at 12500 V. The classified particles are measured by a Faraday Cup Electrometer (FCE-

08). The EMSSYS operating software converts the measurement data to the size distributions, calculated as dN/dlnD.

4.3.2. Electrical Low Pressure Impactor

The Electrical Low Pressure Impactor (ELPI) is an on-line system for real-time measurements of particle size distribution and concentration in the size range of 6 nm – 10 μm. The operating principle can be divided into three major parts: particle charging in a unipolar corona charger, size classification in a cascade impactor and electrical detection with sensitive electrometers (Keskinen et al., 1992). The particles are first charged into a known charge level in the corona charger. After charging, the particles enter a cascade low pressure impactor with electrically insulated collection stages. The particles are collected in the different impactor stages depending on their aerodynamic diameter, and the electric charge carried by particles into each impactor stage is measured in real-time by sensitive electrometers. This measured current signal is directly proportional to particle number concentration and size, thus the instrument gives particle concentration and size distribution in real-time. By switching the charger unit off, the ELPI can be used for particle charge distribution measurements. The instrument used for this thesis work was a Dekati Classic ELPI^{TM}.

4.3.3. Atomic Force Microscopy

The Atomic Force Microscopy AFM is a Scanning Probe Microscopy SPM technique designed by Binning, Qatar and Gerber in 1986; it has recently proved to be very attractive for studying size and morphology of submicron particles (Friedbacher and Grasserbauer, 1995), also in the field of combustion-generated nanoparticles (D'Alessio et al., 2005). A Scanning Probe Microscope NTEGRA Prima from NT-MDT, coupled with NOVA SPM post-processing software, is available in our laboratories.

The AFM has several advantages with respect to other microscopy techniques. This instrument can easily operate in ambient condition, with a fast imaging procedure, and furnishes 2-D and 3-D topological maps of the samples, with an imaging resolution up to the Angstrom scale. A typical AFM system consists of a cantilever probe and a sharp tip mounted to a Piezoelectric (PZT) actuator and a position sensitive photo detector for receiving a laser beam reflected off the end-point of the beam to provide cantilever deflection feedback. The AFM working principle is based on the interaction between the nanometric probe at the end of the cantilever and the sample surface; the probe carries out a scanning of the surface interacting with the sample through attractive or repulsive forces.

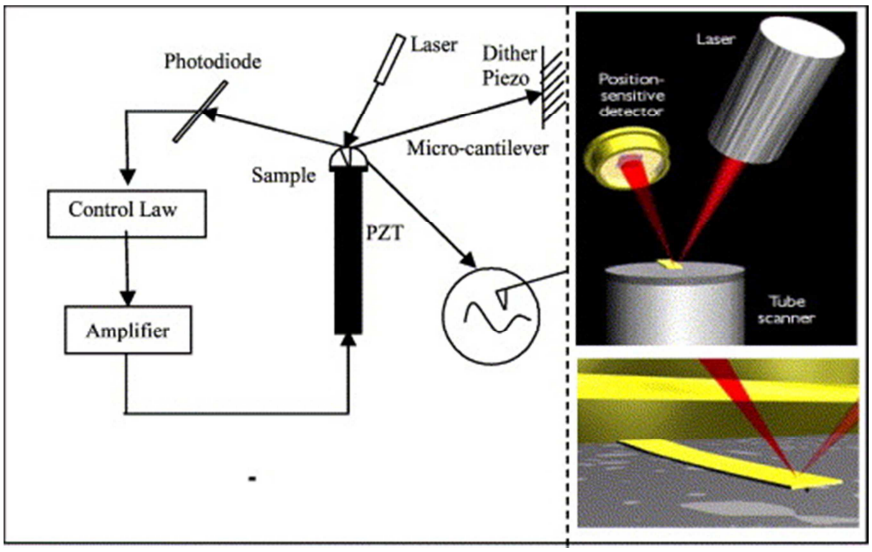

Figure 4.4. Schematic of basic AFM operation (N. Jalili and K. Laxminarayana, 2004).

Semi-contact AFM operation mode is one of the most useful techniques for surface topography measurements. Those kinds of measurements are performed oscillating the probe close to the sample surface at its mechanical resonance frequency, avoiding any strong tip-sample interaction. This mode allow to obtain 3-D images of collected material with a resolution of about 1-2 nm along X and Y axes and below 0.1 nm along Z axis in low noise conditions. Furthermore, in semi-contact mode it is possible to investigate other properties of the samples by means of the phase shift detection, that measures the phase shift between the oscillation input signal and the deflection/oscillation output signal of the cantilever. Changes in the phase of cantilever oscillation are caused by changes in the investigated material properties like viscoelasticity, hardness, stickiness.

In addition to surface topography characterization, AFM is also a powerful tool for several spectroscopy techniques measurements, like Scanning Spreading Resistance Microscopy (SSRM) and Force-Distance Spectroscopy. Local electrical conductivity measurements can be performed operating the AFM in SSRM mode (De Wolf et al., 2001). A conductive probe is used to scan the sample in contact mode, while a DC bias is applied between the tip and a second contact. Resulting current flowing through the sample is measured using a lock-in logarithmic amplifier. Unlike other scanning probe-based techniques, SSRM offers the possibilities of measuring independently topography and conductivity of the samples. In Force-Distance Spectroscopy, the forces acting between the AFM tip and the surface under investigation are recorded during approach and retract of cantilever to e from the sample, and plotted as force-distance curves (Butt et al., 2005). From these measurements, short-range attractive and adhesive forces can be quantitatively evaluated.

Mica muscovite disks (9 mm in diameter, 0.15 mm tick) are the ideal substrates for AFM analysis of thermophoretic-collected particles (Barone et al., 2003), due to unique features such as low roughness, elevated mechanical and chemical resistance to high temperatures, and the possibility to obtain extremely clean surface by cleaving process.

4.3.4. Scanning Electron Microscopy

A Philips XL30 Scanning Electron Microscopy (SEM) with a LaB6 filament, equipped with an EDS DX-4i microanalysis, was used to perform imaging of generated nanoparticles. Two different kind of analysis may be performed, both based on scattering of the electron beam focused on the sample and generated by a LaB6 filament: secondary electron detection and backscattered electron detection. The secondary electrons technique is based on low energy electrons (<50eV) generated at a distance of a few nanometers from the surface. The electrons are detected by a photomultiplier, and the two-dimensional intensity distribution is converted in a digital image. The backscattering technique consists in generating high energy electrons which are reflected or backscatter by the sample. Obviously the analysis involve a sample surface layer some tens of microns in thickness. The sample elemental chemical analysis can be performed by detecting the reflected X-rays energy spectrum through the use of the EDXS.

4.3.5. Optical spectroscopy: UV-Vis Absorption, Raman Scattering and X-Ray Diffraction

Ultraviolet-visible (UV-Vis) spectroscopy is used to obtain the absorbance spectra of a material in solution or as a solid, by measuring the absorption of electromagnetic radiation in the UV-Vis region (200-800 nm), which excites electrons from the ground state to higher-energy excited states. UV-Vis spectroscopy can be used to characterize optical and electrical properties of flame-produced nanoparticles and their dependence on size, morphology and synthesis conditions, for potential applications as materials in the areas of solar energy conversion, optoelectronics and photocatalysis. The optical band-gap, defined as the energy difference between the highest occupied molecular orbital and the lowest unoccupied molecular orbital, can be derived from the absorption spectra by means of the well-know Tauc's procedure (Tauc et al., 1966; Tauc, 1968). The instrument used to perform UV-Vis spectroscopic analysis is a Spectrophotometer Agilent 8453, coupled with Agilent UV-Vis ChemStation.

Raman scattering is a spectroscopic technique based on the inelastic scattering of monochromatic light, usually from a laser source. When photons of the laser light hit the sample surface and excite sample molecules into virtual energy states, there are three different potential outcomes. First, molecules can relax back down to the ground state and emit a photon of equal energy to that

of the incident photon, resulting in an elastic process, which is referred to as Rayleigh scattering. Second, molecules can relax to a real phonon state and emit a photon with less energy than the incident photon (Stokes shifted Raman scattering). The third potential outcome is that molecules are already in an excited phonon state, so are excited to a higher virtual state, and then relaxe back down to the ground state emitting a photon with more energy than the incident photon (Anti-Stokes Raman scattering). The energy transitions associated to Rayleigh and Raman scattering are schematically represented in the Jablonski Diagram (J.R. Lakowicz, 2006) of Fig. 4.5.

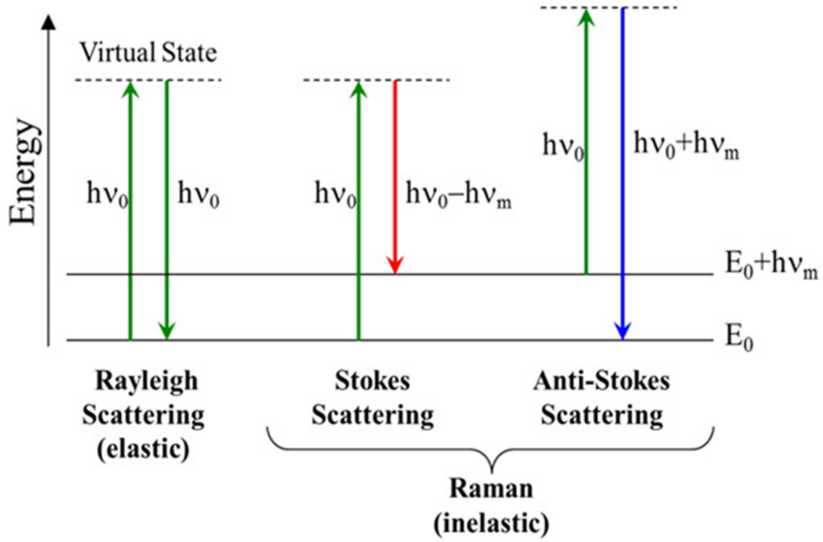

Figure 4.5. Schematic representation of energy transitions for Rayleigh and Raman scattering.

Due to the fact that most molecules will be found in the ground state at room temperature, there is a much lower probability that a photon will be Anti-Stokes scattered. As a result, most Raman measurements are performed considering only the Stokes shifted light.

The energy shift of the scattered photons provides information about vibrational, rotational and other low frequency transitions in molecules. Raman spectroscopy is a powerful method for investigating structural properties of nanoparticles, since the variations in Raman spectra induced by a decrease in particle size can be easily detected (Choi et al., 2005). Raman spectra can also furnish phase information for crystalline and amorphous pure nanomaterials and nanocomposites (Choudhury et al., 2013). The instrument used to perform Raman scattering analysis is Horiba Xplora Raman Microscopes, coupled with LabSpec+ software, with a 100x objective (NA 1.4, Olympus). The laser source is a frequency doubled Nd:YAG-solid state laser (k= 532 nm, 12 mW maximum laser power at the sample). All the spectra reported in this thesis were multipoint baseline corrected, normalized at the G peak around 1600 cm^{-1} and fitted using Nonlinear Curve Fit function of Origin 8.5 package. The best fit, based on the Levenberg–Marquardt method, was performed us-

ing a combination of both Gaussian and Lorentian curves following the work by Sadesky et al. (2005). The first order spectra were fitted with six peaks whereas the second order spectra were fitted with four peaks. The quality of the fitting procedure was tested in terms of the reduced chi-square (χ^2/DoF) and adjusted coefficient of determination (adjusted R^2).

X-ray diffraction is a non-destructive standard quantitative tool for identifying crystalline phases in nanostructured powder or film samples (Kodas and Hampden-Smith, 1999). Different phases diffract incident X-rays according to Bragg's equation, which correlates lattice spacing to X-ray wavelength. In addition, the well-known Scherrer equation (Cullity et al., 1978) can be used to relate the widths of the peak to crystallite size, and to calculate the unit cell dimensions. In the presence of several phases, the relative amount of each phase can be determined by comparing the width and the height of the diffraction peaks (Spurr and Myers, 1957). In routine work, XRD relies on the availability of standards that allow the identification of peaks in the diffraction patterns. Bruker D2 Phaser X-Ray Powder Diffractometer is available.

4.3.6. Current-Voltage characteristics

Electrical properties of synthesized particles were measured by depositing the material on quartz substrates provided with aluminum metal electrodes. Such substrates were prepared depositing an aluminum film directly on the substrate surface by d.c. magnetron sputtering technique at room temperature, and defining electrodes geometry by photolithography technique. The contact geometry was chosen to be in-line. The I-V measurements were carried out at room temperature by a four probe technique using a Keithley Model 6487 picoammeter/voltage source (Keithley Instruments, USA), connected to a Signatone H-150 probe station (Signatone Corporation, USA).

4.3.7. Probe sampling for on-line diagnostics

The sampling device adopted in order to dilute, quench and transport the aerosol collected from the flame to the DMA and the ELPI is a horizontal on-line sampling probe, ad reported I Fig. 4.6. A great number of probes were developed during the last decades to reduce and minimize any sampling artifact. The first probe placed horizontally above the burner was designed by Kasper et al. (1997) and it was made of a straight stainless tube with a small orifice for sample intake. Flame gas sample was rapidly diluted by nitrogen gas in the probe, with the main purposes to quench chemical reaction, prevent the particles from coagulating or growing through condensation, and therefore avoid alteration of particle size distribution during the sampling process. A sample probe similar to that of Kasper was used by Zhao et al. (2003) to measure the size distribution of flame-made TiO_2 nanoparticles, furnishing also further experimental information.

The probes used in this research activity were developed in our laboratories (Sgro et al., 2007), starting from that designed by Zhao. They are 1 mm thin, 260 mm long stainless steel tubes with an internal diameter of 8mm, placed horizontally on the burner and connected to a water-cooled heat exchanger. The heat exchanger is required in order to cool sampled aerosol before it reaches the instrument. Probes pinhole diameters are 0.2 mm, 0.3 mm and 0.8 mm.

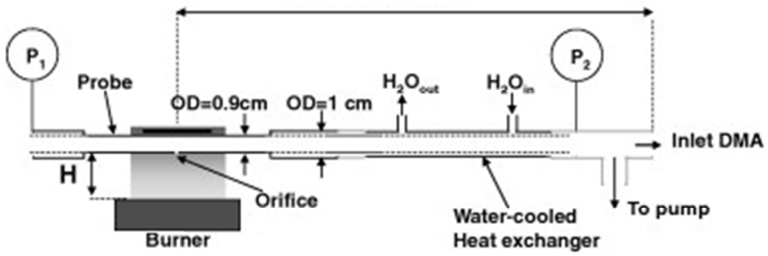

Figure 4.6. Sketch of on-line probe sampling line (De Filippo et al., 2009).

The aerosol is sampled from the flames by creating an appropriate under-pressure near the hole and it is suddenly diluted in pure nitrogen. Nitrogen flow is used to prevent particle-particle coagulation in the sampling line, with the aim to study particle properties as they exist in the flame. Depending on pinhole diameter, under-pressure and nitrogen flow rate, the Dilution Ratio (DR) can vary from 1000 to 30000. Coagulation phenomena in the sampling line are avoided when a critical DR is reached, beyond which size distributions remain almost constant even if DR is further changed.

4.3.8. Probe sampling for ex-situ characterization

A probe-sampling method, similar to that used for DMA analysis, was developed to perform *ex-situ* analysis. It is based on a dilution probe tube with a 2.5 mm-diameter orifice, placed horizontally above the burner, and connected to a water-cooled heat exchanger and a filter holder. Particles in the sampling line are collected by impact on quartz, Teflon or silver filters placed inside the holder. Nitrogen is used as diluent in order to quench the flame chemical reactions. A lower dilution ratio (~100) was used as compared to probe sampling for DMA analysis, since it is not necessary to avoid particle-particle coagulation in the sampling line.

In addition, a colloid of as-synthesized particles in water, ethanol or other dispersion liquids can be prepared by immersing filters in the desired medium and dispersing particles with the aid of an ultrasonic cleaning bath Elmasonic E15H.

4.3.9. Thermophoretic sampling techniques

A thermophoretic sampling method for *ex-situ* AFM analysis was used during this research. It consists of a double-acting pneumatic cylinder (see Fig. 4.7) equipped with a substrate holder mounted over a mobile extension, used to insert a tin holder in flame with a constant sampling time for each insertion, ranging from 10 ms to 100 ms. Different holders, able to accommodate different substrates such as mica muscovite disks, aluminum sheets and copper TEM grids, were prepared.

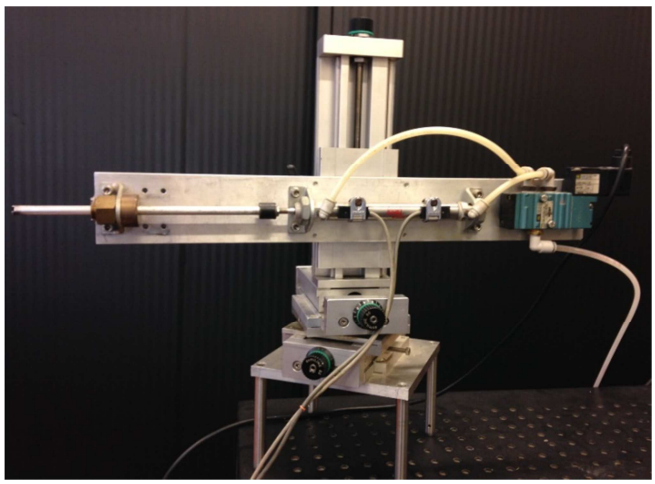

Figure 4.7. Picture of pneumatic actuator used for thermophoretic sampling.

The cold surface of the substrate contained in the holder produces a strong temperature gradient with respect to the hot combustion gases. Particles suspended in the gaseous medium move towards the substrate surface, where they impact and deposit, due to a net force which tends to push them away from high-temperature region towards the lower temperature zone, called thermophoresis force (Hinds, 1999).

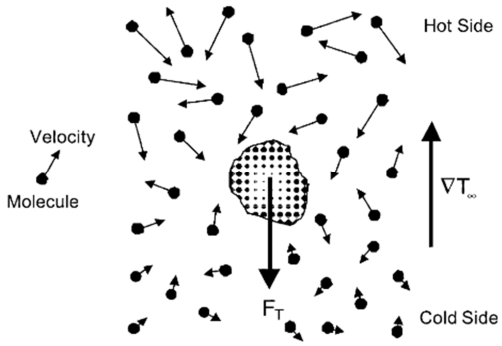

Figure 4.8. A particle immersed in a gas with a temperature gradient (Zheng, 2002).

The main advantage of this sampling system is that thermophoretic drift velocity is independent from particle size in a wide range of diameters (Dobbins and Megaridis, 1987). For this

reason, thermophoretic sampling with short insertion times (10-30 ms) and a few numbers of insertions, up to 3, allows to collect enough single and isolated particles, representative of particles population into the aerosol, on which a size and morphology AFM analysis can be performed. On the other hand, thermophoretic sampling with longer insertion times (100 ms) and a very high number of insertions, more than 100, is a possible way to obtain a quite homogenous coating of the whole substrate, in order to investigate film properties of collected material by means of AFM.

A further sampling technique based on the thermophoresis effect was used to collect nanopowders synthesized in the flame reactors for batch *ex-situ* analysis, i.e. SEM, XRD, UV-Vis and Raman. This technique involves the use of a chilled stainless steel plate, placed downstream from the burner, on which nanopowders are collected by thermophoresys and then removed and characterized.

5. Production and characterization of carbonaceous nanoparticles

In this chapter, the results concerning the production via flame synthesis and the subsequent dimensional and physical-chemical characterization of different carbon nanostructures are presented.

5.1. Two-dimensional carbon nano-disks

This part of the thesis work was spent on selecting and investigating, on the base of previous studies conducted by our research group (Sgro et al., 2010; Commodo et al., 2013), appropriate flame conditions in order to produce just primary carbon compounds subject to minimal particle-particle interaction in flame, i.e. coagulation and coalescence phenomena. These conditions are intermediate between near-stoichiometric fuel rich flames, which generate chemically-excited small molecules, and sooting flames, where incomplete oxidation reactions brings about the formation of solid compounds, whose thermal emission is responsible of the typical yellow-orange flame luminosity. The aim was to synthesize planar nanostructures preserving the original structure of the incepted particles, and avoiding possible stacking of graphitic planes which may be caused by coagulation processes.

5.1.1. Experimental set-up

The reactor we chose was an atmospheric pressure ethylene/air flat laminar premixed flames, with the equivalent ratio fixed at Φ=1.83 (C/O=0.61) and a cold gas velocity of 10 cm/s, stabilized on a McKenna burner, as described in Section 4.2. The maximum flame temperature was 1770 K at about 1 mm height above the burner (HAB) and decreased to about 1600 K at the sampling location, 15 mm.

Carbon compounds were collected on freshly cleaved mica sheets by means of the thermophoretic pneumatic actuator, with a sampling time of 30 ms necessary to collect isolated compounds.

AFM was operated in semicontact mode in air with NANOSENSORS^{TM} SSS-NCHR supersharp silicon probes with nominal tip radius of 2 nm, a half cone angle at 200 nm from tip apex less than 10° and a 125-μm long cantilever with a spring force constant of 42 N/m and a range of resonance frequency 204–497 kHz. The level of tapping force used during imaging is given by the set-point ratio, i.e., the ratio between the set-point amplitude and the free-oscillation amplitude. All the images were acquired with a set-point ratio equal to 0.25. The AFM images were obtained with a

scan rate of 0.3–0.5 kHz over a selected area of 2 μm x 2 μm and 1 μm x 1 μm (1024 x 1024 pixel resolution). The calibration of AFM scanner vertical movement was performed by means of NT-MDT SiC/0.75 calibration sample, which has a uniform distribution of 0.75 nm – height steps on its surface. All the images were not filtered.

For chemical and structural analysis, flame products were collected by probe sampling method for *ex-situ* analysis on quartz filters. The sampling time was about one hour to allow the collection of enough material for the Raman analysis (0.7 mg).

Raman spectra were obtained with a laser beam power of 10%, and accumulation-exposure times of 5 cycles of 30 s each. For each sample, 7–10 spots were randomly selected and averaged. Spectra were then fitted following the procedure reported in Section 4.3.4.

On-line measurements of the size distribution of the sampled particles were performed by using a differential mobility analyzer DMA (see Section 4.3.1).

5.1.2. Morphological analysis

Morphological analysis was conducted on isolated carbon compounds collected by thermophoretic sampling after 1 insertion of 30 ms sampling time. The AFM image of the sample deposited on a mica plate over an area of 2 x 2 μm^2 is shown in Fig. 5.1. During the sampling time of 30 ms a large number of nanosized compounds is deposited on the mica substrate. The compounds are disk-like with base diameter of the order of tens of nanometers and height lower than 1 nm.

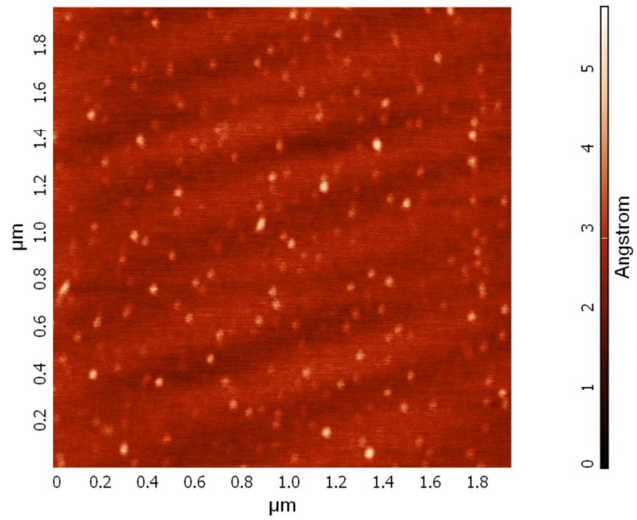

Figure 5.1. AFM image of the sample deposited on a mica plate over an area of 2x2 μm^2.

A more clear view of their size and shape is shown in Fig. 5.2, in which the image of a typical carbon disk measured with a larger resolution and zoomed to 200 x 200 nm^2 is reported together

with the height profile along the green line. The in-plane shape is spherical, with a diameter of few tens of nanometer, whereas the height is of about 3.5 Ångströms.

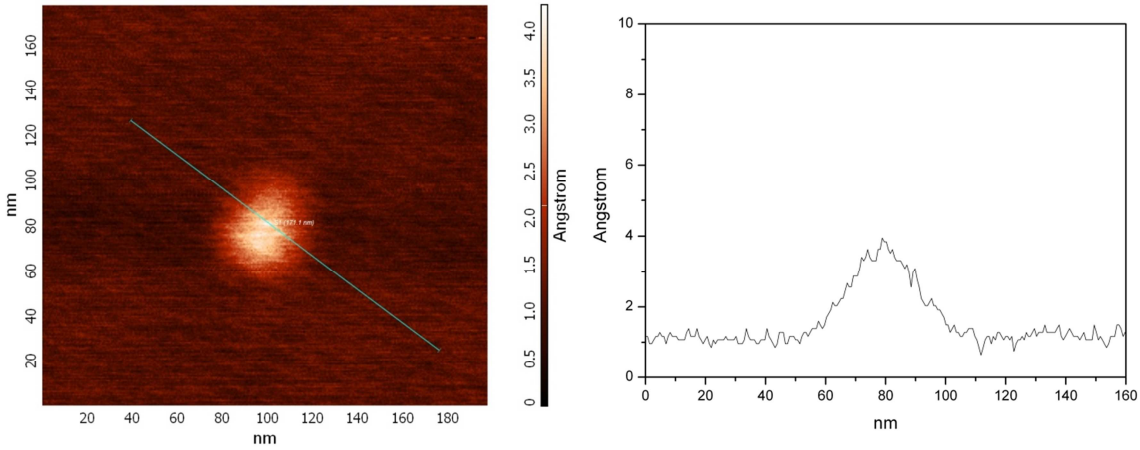

Figure 5.2. (Left) AFM image of a flame generated carbon disk deposited on mica substrate, and (right) height profile along the green line.

Image analysis conducted on a statistically representative sample furnished the distributions of height and base diameter reported in Figs. 5.3a and 5.3b, respectively. The height of the particles (h) is distributed over an interval smaller than 2 Å, the distribution is unimodal with an average value of <h> = 0.28 ± 0.04 nm. This value is indicative of a single-atom thickness. The base diameters (D) are distributed over a broader range, from 5 to 40 nm with a mean value of <D>=22 ± 5 nm.

It is well known that AFM images are measured along vertical axes with the larger resolution, even less than one Ångström, whereas the lateral resolution is limited by tip convolution effects. To improve lateral resolution, tip artifacts have been minimized by using a super-sharp tip. Nevertheless, the measured images are always a convolution of the probe geometry and the shape of the features being imaged, resulting in an overestimation of the sample size. This effect might be corrected given the knowledge of the shape of the probe and apex, but this procedure does not take into the account of manufacture defects, damaged or messy probes, so that the base diameter can never be determined with a precision better than few nanometers. We therefore considered that base diameter was overestimated by 5 nm, about two tip radii, and subtracted this value in the evaluation of the base diameter of the measured objects.

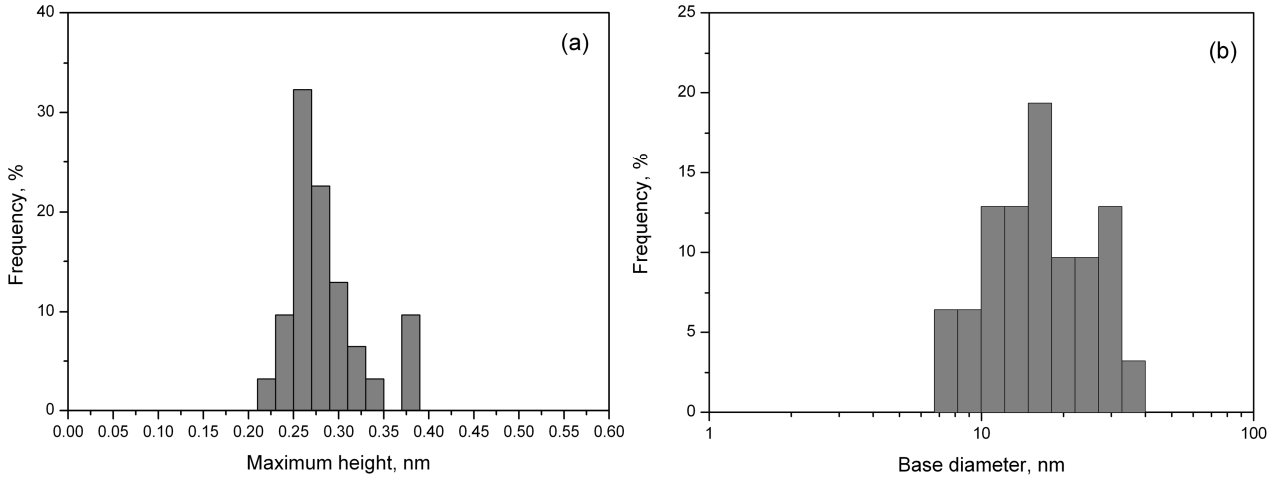

Figure 5.3. Distribution of a) maximum height (h), and b) base diameter (D) of flame nano-disks.

In order to verify that the results of AFM measurements were not affected by artifact, we compared the size of the sampled compounds with that of the compounds in aerosol phase. To this aim, for each object measured by AFM the volume was evaluated from the base diameter and height considering a conical shape, and the distribution of the diameter of spheres with equal volume was finally determined. Flame products were also collected from the flame by a suction probe and the aerosol analyzed on line by a differential mobility analyzer (DMA) for measuring the size distribution of the solid compounds suspended in the gas. DMA determines the diameter of the compounds, assuming a spherical shape, by the measure of their mobility in an electric field; from the mobility diameter we estimated the diameter of the particles using the correction expression reported in Equation 4.3. The comparison of these size distributions, the DMA-diameter and the AFM-sphere equivalent diameter, is reported in Fig. 5.4.

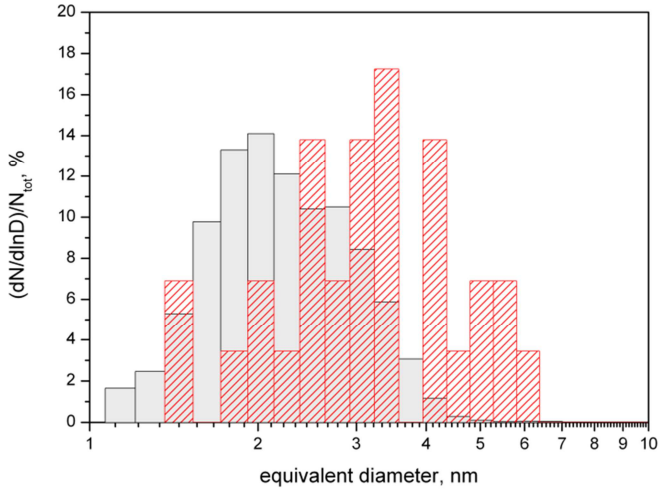

Figure 5.4. Size distribution of flame formed compounds. Full gray bars: aerosol based DMA-diameter; Red line bars: AFM-sphere equivalent diameter.

The size distribution measured on line in aerosol phase (full gray bars) consists in a monomodal distribution of diameters smaller than 5 nm with a mean diameter equal to $<D_{DMA}>=2.4 \pm 0.7$ nm. The distribution of the deposited compounds is slightly broader; the maximum is shifted towards larger diameter and the mean diameter is equal to $<D_{AFM}>=3 \pm 1$ nm. Considering that the two measuring methods are based on a different definition of diameter and considering the experimental uncertainties, the results are in good agreement confirming that the compounds measured by AFM are representative of the species produced in flame and are not due to artifact during sampling.

5.1.3. Raman analysis

The chemical characterization has been performed by Raman spectroscopy on materials collected by probe sampling on quartz filters. The Raman spectrum of flame-formed nano-disks is reported in Fig. 5.5, together with the spectrum of Highly Ordered Pyrolytic Graphite (HOPG) and of single layer graphene.

The most prominent features in the spectrum of nano-disks are two peaks centered at 1340 and 1614 cm^{-1}. The most intense one corresponds to the G peak, which is produced by phonon modes with E_{2g} symmetry and is Raman active for every sp^2 carbon networks. The position of the G peak in carbon compounds in not unique since it is very sensitive to the carbon network (Ferrari and Robertson, 2001). The central position shifts upwards in nanocrystalline-graphite up to a maximum of ~ 1600 cm^{-1}. The G peak is located at above 1600 cm^{-1} in amorphous networks in the presence of sp^2 chains under UV excitation. An opposite trend, with a downshift towards 1510 cm^{-1}, is produced by the increase of bond-angle and bond-bending disorder and the presence of non-six fold rings (Ferrari and Robertson, 2001).

The G peak of flame-formed nano-disks is clearly upshifted with respect to HOPG and graphene, whose maxima appear at about 1580 cm^{-1}, and is also sensibly broader. Both features are consistent with a small size of aromatic zones, L_a.

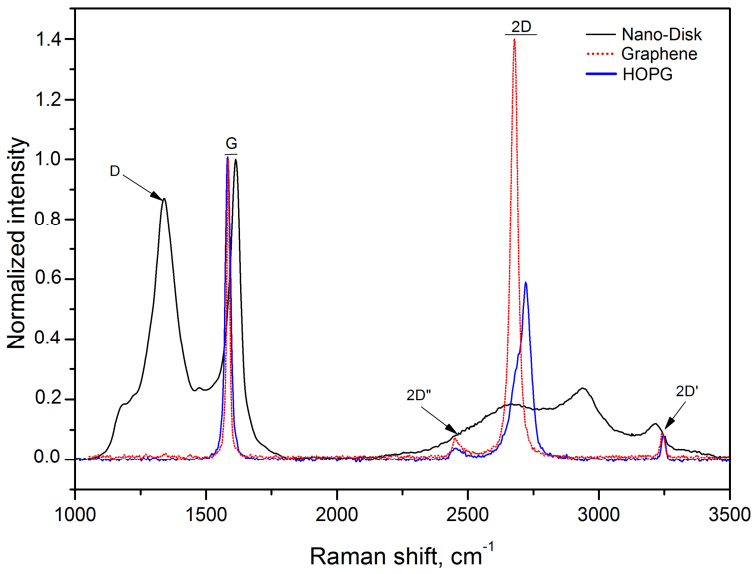

Figure 5.5. Raman spectrum of carbon disks sampled from the flame (black line), of HOPG (blue line), and of single layer graphene (red dotted line).

The band near 1340 cm^{-1} is the so-called D band, since it is a defect induced Raman feature that it is not observed in the spectrum of the highly crystalline HOPG and in a perfect graphene, whereas it becomes strong in nano-crystalline graphite, due to edge effects, or in defected and amorphous carbon (Ferrari and Robertson, 2000).

The ratio of the D and G peak intensity can be used to estimate the in-plane correlation length of aromatic island, L_a. Tuinstra and Koening (1970) reported that the intensity of the D band is inversely proportional to the effective crystallite size, L_a, in the direction of the graphite plane, or to the average distance between defects, L_d, in graphene, up to a minimum L_a or L_d of about 2 nm; when the effective crystallite size or the distance between defects further decreases, I(D)/I(G) decreases to zero. Since the Raman spectrum of flame-formed nano-disks has the G band clearly upshifted and broader compared to HOPG and graphene, a relevant phonon confinement due to very small crystallite size is occurring. We can then conclude that the correct regime for our sample is that one with I(D)/I(G) proportional to L_a^2.

Table 5.1 reports values of L_a obtained using the various expressions reported in the literature. The in-plane size of aromatic island in our sample results to be about 1.3 nm.

Table 5.1. L_a calculation based on different equations

Reference	Equation	Parameters	Band ratio	L_a (nm)
Ferrari and Basko, 2013 (eq.7)	$\frac{I_D}{I_G} = aE_L^{-4}L_a^2$	a= 18.5 E_L = 2.33 eV	I_D/I_G = 0.86[a]	1.2
Cançado et al., 2011 (eq.1)	$\frac{I_D}{I_G} = C_A\frac{r_a^2-r_s^2}{r_a^2-2r_s^2}\left[\exp\left(-\frac{\pi r_s^2}{L_D^2}\right) - \exp(-\frac{\pi r_a^2 r_s^2}{L_D^2})\right]$	$C_A = 160/E_L^4 = 5.42$ r_A = 3.1 nm r_S = 1.0 nm	I_D/I_G = 0.86[a]	1.3
Lucchese et al., 2010 (eq. 8)	$\frac{I_D}{I_G} = C_A\frac{r_a^2-r_s^2}{r_a^2-2r_s^2}\left[\exp\left(-\frac{\pi r_s^2}{L_D^2}\right) - \exp\left(-\frac{\pi r_a^2 r_s^2}{L_D^2}\right)\right] + C_s(1 - \exp\left(-\frac{\pi r_s^2}{L_D^2}\right))$	$C_A = 4.2*(2.41/E_L)^4$=4.82 Cs = 0.87 r_A = 3.0 nm r_S = 1.0 nm	I_D/I_G = 1.58[b]	1.3
Martins Ferreira et al., 2010 (eq. 9)	$\frac{A_D}{A_G} = C_A\frac{r_a^2-r_s^2}{r_a^2-2r_s^2}\left[\exp\left(-\frac{\pi r_s^2}{L_D^2}\right) - \exp\left(-\frac{\pi r_a^2 r_s^2}{L_D^2}\right)\right] + C_s(1 - \exp\left(-\frac{\pi r_s^2}{L_D^2}\right))$	$C_A = 3.6*(2.41/E_L)^4$=4.13 Cs = 2.4 r_A = 4.1nm r_S = 2.6 nm	A_D/A_G = 2,39[c]	<1.7

[a] I_D/I_G ratio evaluated from the maximum of the two bands.

[b] I_D/I_G ratio calculated at a fixed frequency: I_D at1345 cm^{-1} and I_G at 1585 cm^{-1} (or I_{1345}/I_{1585})

[c] A_D/A_G ratio evaluated from the areas of the two bands.

Because of the superposition of the lines, the spectrum has been fitted with a multiple line function for a detailed analysis, as shown in Fig. 5.6. Two different regions of the spectrum have been fitted separately: the first order region, between 1000 and 1800 cm^{-1}, was fitted with 5 Lorentian and 1 Gaussian curves, and the second order region, between, 2000 and 3600 cm^{-1}, with 4 Lorentian curves. The values of the parameters resulting from the fitting procedure are reported in Table 5.2 for the first order Raman region and in Table 5.3 for the second order Raman region.

Table 5.2. Curve fitting analysis results for the first order Raman region.

Sample	*Peak Index*	*Peak Type*	*Area Fit*	*Center Max*	*Max Height*	*FWHM*
Flame Nano-disk	Peak 1175	Lorentz	5.6 ± 0.5	1176 ± 4	0.07 ± 0.01	49 ± 2
	D"	Lorentz	4.2 ± 0.3	1222 ± 6	0.048 ± 0.003	56 ± 2
	D	Lorentz	148 ± 3	1340 ± 4	0.87 ± 0.03	109 ± 2
	D3	Gaussian	22 ± 2	1529 ± 4	0.13 ± 0.03	163 ± 6
	G	Lorentz	32 ± 2	1598 ± 4	0.43 ± 0.03	47 ± 2
	D'	Lorentz	31 ± 1	1618 ± 4	0.66 ± 0.03	30 ± 1
HOPG	G	Lorentz	41 ± 1	1583 ± 4	1.01 ± 0.02	25 ± 1
Graphene	G	Lorentz	19 ± 1	1584 ± 4	1.01 ± 0.02	12 ± 1

Table 5.3. Curve fitting analysis results for the second order Raman region.

Sample	*Peak Index*	*Peak Type*	*Area Fit*	*Center Max*	*Max Height*	*FWHM*
Flame Nano-disk	2D"	Lorentz	1.7 ± 0.2	2469 ± 4	0.096 ± 0.003	934 ± 1
	2D	Lorentz	97 ± 4	2667 ± 4	0.17 ± 0.01	367 ± 3
	G+D, D+D'	Lorentz	57 ± 3	2939 ± 4	0.18 ± 0.02	203 ± 4
	2D', G+D'	Lorentz	17 ± 1	3213 ± 4	0.088 ± 0.003	121 ± 5
HOPG	2D"	Lorentz	2.8 ± 0.2	2461 ± 4	0.038 ± 0.001	42 ± 1
	$2D_{3DA}$	Lorentz	18 ± 1	2684 ± 4	0.21 ± 0.02	54 ± 3
	$2D_{3DB}$	Lorentz	31 ± 1	2723 ± 4	0.56 ± 0.02	60 ± 1
	2D'	Lorentz	2.7 ± 0.2	3247 ± 4	0.086 ± 0.002	15 ± 2
Graphene	2D"	Lorentz	3.1 ± 0.2	2460 ± 4	0.058 ± 0.002	39 ± 1
	2D	Lorentz	67 ± 1	2679 ± 4	1.45 ± 0.02	29 ± 1
	2D'	Lorentz	2.5 ± 1	3245 ± 4	0.087 ± 0.002	18 ± 2

In the first order region, the result of the fitting evidences that the G peak position of our sample is shifted to larger wavenumbers by about 15 cm^{-1} respect to the G band of both HOPG and graphene. As discussed previously, this is explained by the nanosize of graphitic islands; in addition, the presence of C=C bonds in olefinic small chain cannot be excluded, also because of the presence of the 1175 cm^{-1} band. Indeed, this band has been reported in Raman spectra of amorphous hydrogenated carbon a:C-H and was attributed to the CC–H bending mode of the ring in neutral poly (p-phenylenevinylene) (PPV) chain inclusions (Rybachuka and Bell, 2009).

Since the G band is active in every sp^2 structure, indications about the presence of aromatic islands can be derived from the two stronger signals in nano-disks spectrum, D band and D' bands. These bands are particularly intense in Raman spectrum of flame formed carbon nano-disks (see Fig. 17b) indicating that such material is characterized by an aromatic network, even though with a relevant amount of disorder. It is worth noting that D and D' bands are particularly strong and well-defined in graphene and graphitic materials with defects; by contrast, in amorphous carbon or in strongly defective graphene the D and G peaks are not well defined and merge in one broad feature (Jorio et al., 2010). The rather sharp feature of D and D' bands in the spectrum of Fig. 17c with a FWHM of about 100 cm^{-1} and 30 cm^{-1} respectively, indicate that the carbon nano-disks produced in our flame condition are not very much disordered. In a defect-free graphene, the D and D' lines can only be activated by edges; so, in our sample, edges may contribute sensibly to the disorder necessary to activate these bands. In fact, AFM analysis has evidenced that our sample is composed by very small bi-dimensional nano-disks with an average lateral dimension of about 20 nm. Thus, each nano-disk has a relevant part of the area constituted by the D band activation region due to the edge. In addition to the edge effect, other kinds of defects, typical of amorphous carbon, are probably present in flame nano-disks, evidenced by the presence of weak D3 and D'' bands in our sample.

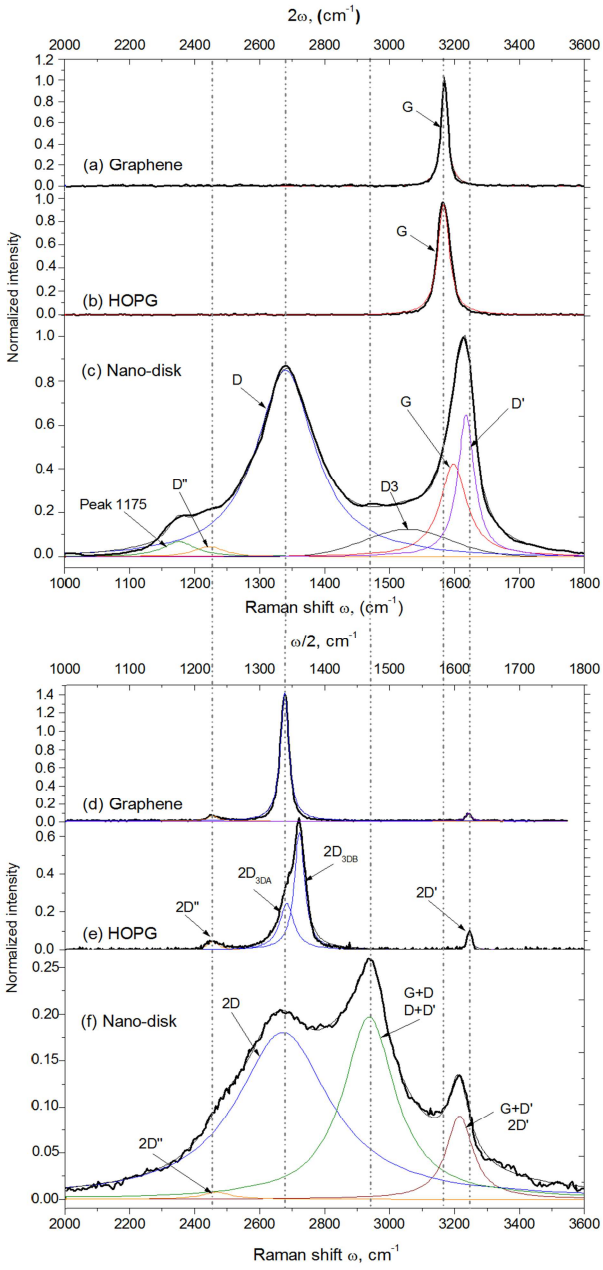

Sample	first order		second order	
	(χ^2/D_OF)	adjusted R^2	(χ^2/D_OF)	adjusted R^2
Nano disk	3.07×10^{-4}	0.9951	2.86×10^{-5}	0.9940
HOPG	1.72×10^{-4}	0.9899	4.02×10^{-5}	0.9933
Graphene	1.09×10^{-4}	0.9954	1.35×10^{-5}	0.9942

Figure 5.6. Measured Raman spectra (thick black line) and multiple best fit lines (thin black line) of graphene, HOPG, and flame nano-disk. (a), (b), (c) refer to the first order region; (d), (e), (f) refer to the second order region. The single peak functions of the fits are also reported by colored lines

Further information can be derived by the analysis of the second order spectrum. The most intense band in all the spectra (HOPG, graphene and nano-disk) is positioned at about 2700 cm^{-1}.

This band is very strong in graphene and graphitic carbon due to a double resonance process involving the same phonons involved in the D band. If the conduction and valence bands are symmetric, like in the case of single-layer graphene, resonance might occur for electrons and holes giving a triple resonance process and a particularly intense line. This band has been defined 2D (Ferrari and Basko, 2013), 2D1 (Sadezky et al., 2005), or also G′ (Malard et al., 2009) to indicate that it is not properly an overtone of the D band since it does not require a disorder to be activated. The most interesting property of this band is that the shape is very sensitive to the number of graphene layer and three-dimensional ordering. In single-layer graphene it consists of a single band, symmetric and very narrow, centered at 2679 cm^{-1} and its intensity is larger than the G band. In bi-layer graphene, due to the splitting of electronic bands, it is composed by four bands, two of which are more intense. Increasing the number of staked layers, up to 3–4, the number of sub-bands continues to increase, so that it broadens and becomes asymmetric (Malard et al., 2009; Ferrari et al., 2006). Whereas, in the limit of AB staked graphite only two component are present: the most intense line at 2720 cm^{-1}, denoted by subscript 3DB, and a shoulder at 2650 cm^{-1} denoted by subscript 3DA (Cancado et al., 2008; Lespade et al., 1984) (the band has an asymmetric shape as can be observed in Fig. 5.6e for HOPG). With decreasing the interlayer interaction, the two lines get closer and in turbostratic graphite, which is an intermediate case between a three-dimensional structure and an ensemble of two-dimensional graphitic planes, the band is again symmetric, centered at about 2700 cm^{-1}, in an intermediate position respect to the $2D_{3DA}$ and $2D_{3DB}$ of graphite, but it is broader, less intense and shifted to larger frequencies than that of a perfect graphene (Mafra et al., 2007).

In our nano-disks the 2D band is much broader than that of HOPG and graphene. Its maximum occurs at a frequency close to the one of graphene and the $2D_{3DA}$ band of HOPG. This is a clear evidence of the absence of carbon–carbon interaction along the z axis, and supports the bi-dimensionality of the nano-disks measured by AFM.

In addition to the 2D band, three additional features can be observed in the second order region of flame-formed nano-disks spectrum. A rather sharp band, which was assigned to G+D phonons by Wrightet al. (1976) and to D+D’ phonons by Nemanich and Solis (1979), is present at 2950 cm^{-1}, and is activated by disorder. The strong intensity of this peak indicates that edges are not the only source of disorder in our nano-disks, but lattice distortion has a relevant part in activating the Raman lines. Such lattice distortion can be caused by the presence of sp^3 components or penta-rings, which might also explain the not perfectly flat shape of the disk measured by AFM. Two weaker features are present, centered at 3240 cm^{-1} and 2450 cm^{-1}, and can be assigned to the overtone of the D’ band and the D’’ band, respectively.

5.2. Flame-formed carbon nanoparticles: optical and electrical properties

In this part of the research activity, we focused on the synthesis of carbon nanostructures in different sooting flame conditions (from slightly to fully sooting), moving to equivalence ratios higher than carbon nano-disks synthesis conditions. The aim was to characterize the dependence of composition and optical properties of such flame-formed carbon nanoparticles (FFCNPs) with respect to their electrical conductivity. It is a matter of fact that the electrical characterization of carbon materials, such as graphite, coke, carbon fibers and especially carbon blacks, have been yet conducted by several researchers over the years (Chung, 2004); also, it is established that soot and carbon black derive from similar formation processes and possess similar composition and properties. Nevertheless, recent studies about the correlation between soot structure and conductivity (Grob et al., 2012) highlighted differences in both microstructure and electrical properties between soot particles and commercial carbon blacks. That being so, a deeply knowledge of structural and conductivity properties of FFCNPs can be useful to realize conductometric sensors for the detection of particulate matter emitted from engines (Hagen et al., 2010; Grob et al., 2012), and also to calibrate these sensors on the different classes of FFCNPs, with different electrical behavior.

5.2.1. Experimental set-up

The combustion reactor consists of a flat, atmospheric pressure, laminar premixed flame of ethylene and air, stabilized on a McKenna burner. Particles are produced by changing the reactor characteristics, i.e., residence time (sampling position) and equivalent ratio, maintaining unchanged the other parameters, such as the maximum flame temperature. Table 5.4 reports the operating conditions used in this work.

Table 5.4. Investigated flame reactor parameters

	Flame 1	*Flame 2*	*Flame 3*	*Flame 4*
C/O ratio	0.72	0.77	0.85	0.85
Equivalence ratio Φ	2.18	2.33	2.58	2.58
Cold gas velocity (cm/s)	10	10	10	10
Sampling position (mm)	6	10	10	15
Particle Residence time (ms)*	6.4	14.4	13.7	25.2

* Particle residence time was calculated from the flame residence time at the sampling position respect to the flame residence time at particle inception, assuming that particle velocity is equal to hot gas velocity. This last is determined measuring particle volume fraction from the time evolution of the thermocouple junction temperature as described in McEnally et al. (1997), Basile et al. (2002) and Abid et al. (2008).

Flame 1 is slightly-sooting; the sampling position is located below the soot inception point as determined by visible luminosity. Flame 2 and Flames 3-4 are sooting and fully-sooting flames,

respectively. In those flames, the sampling position is in the soot loading region, just after particle inception (see Section 2.2.1).

Two different procedures have been used to withdrawn particles from the flame and deposit them on the desired substrates. For Flame 1 condition, due to the very low particle concentration produced in such flame conditions, the probe sampling method for ex-situ analysis was used, while for Flame 2-4 conditions the thermophoretic pneumatic actuator method was used.

Flame temperature was measured by a fast insertion procedure using a 125 μm R-type thermocouple (Pt/13%Rh vs. Pt, Omega Engineering). Temperature measurements are corrected for radiation losses (McEnally et al., 1997). The profiles are reported in Fig. 5.7.

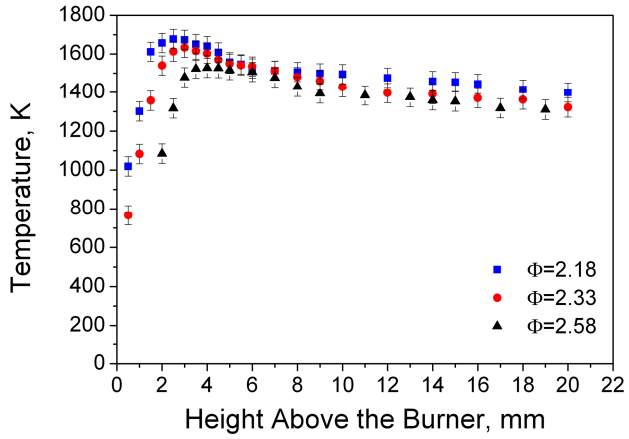

Figure 5.7. Temperature profiles measured for the studied flames. Error bars report the uncertainty in the temperature of ± 50 K.

For optical analysis, the carbon materials were collected on quartz substrates (25 x 75 x 1 mm). UV-visible spectra were measured in the wavelength range 190–1100 nm. Raman spectra were obtained with a laser beam power of 10%, and accumulation-exposure times of 5 cycles of 30 s each. For each sample, 7–10 spots were randomly selected and averaged. Spectra were then fitted following the procedure reported in Section 4.3.4.

Electrical properties of the carbon samples were measured by depositing the material on quartz substrates provided with aluminum metal electrodes (the size was 5 x 2 mm and the distance between electrodes was 1 mm).

AFM images were acquired on particles collected on freshly cleaved mica substrates, operating the instrument in semi-contact mode in air and equipped with NANOSENSORS™ SSS-NCHR super-sharp silicon probes (nominal tip radius 2 nm).

5.2.2. Optical and chemical characterization

UV-visible absorption spectra of Flame 1-4 samples are reported in Fig. 5.8 (left side). FFCNPs from Flame 1 were collected for a total sampling time ranging from t_{samp}=10 min to t_{samp}=30 min. FFCNPs from Flames 2-4 were collected by rapidly inserting the quartz substrate in flame several times, varying the total number of insertions (I). The residence time of each insertion was fixed at 100 ms, so that we increased the total sampling times by simply increasing the number of insertions in the flame. By increasing the total sampling time, the amount of particulate matter deposited on the substrates increases linearly, as proved by the rise in the light absorption signal shown in Fig. 5.8. The absorption spectra of collected material present a maximum value in the UV and decreasing values in the visible spectral region. Moving from Flame 1 to Flame 4, the maximum in the spectrum shifts to longer wavelengths, from λ_{max}=209 nm to λ_{max}=227 nm, and the absorption in the visible increases by a larger quantity with respect to the UV absorption, resulting in an increase of the ratio Abs(λ=500nm)/Abs(λ_{max}) from 0.13 (Flame 1) to 0.33 (Flame 4).

From the light absorption spectra, particle optical band gap was determined following Tauc's procedure (Tauc et al., 1966). For amorphous carbon compounds the dependence of the absorbance, Abs, on optical band gap, E_g, and photon energy, E, is given by the following equation (Robertson, 2002):

$$\sqrt{Abs * E} \propto (E - E_g) \tag{5.1}$$

Figure 5.8 (right side) reports the Tauc plots obtained by plotting the quantity (Abs*E)^0.5 versus E. The spectra refer to a condition of t_{samp}=20 min for Flame 1, and 40 substrate insertions (I=40) for Flames 2-4. E_g values were obtained by a linear fit of the Tauc plots in the range 2.5-4 eV. The same values of the optical band gap, with an experimental uncertainty of about 10% were obtained when data from different sampling times/number of insertions were used.

The analysis of the E_g values shows that in the four flame conditions carbonaceous nanoparticles with different band gaps are formed. Particularly, the optical band gap decreases from about 1.38 eV, typical of carbon materials with a low graphitic composition (Flame 1) (Robertson et al., 2002), down to about 0.74 eV in Flame 4, indicating a higher percentage of sp^2 hybridization and a higher graphitization for such samples. These results evidence the possibility to produce a wide variety of carbonaceous particles, with specific and tailored optical properties, by changing flame conditions, i.e., the flame stoichiometry and the particle residence times.

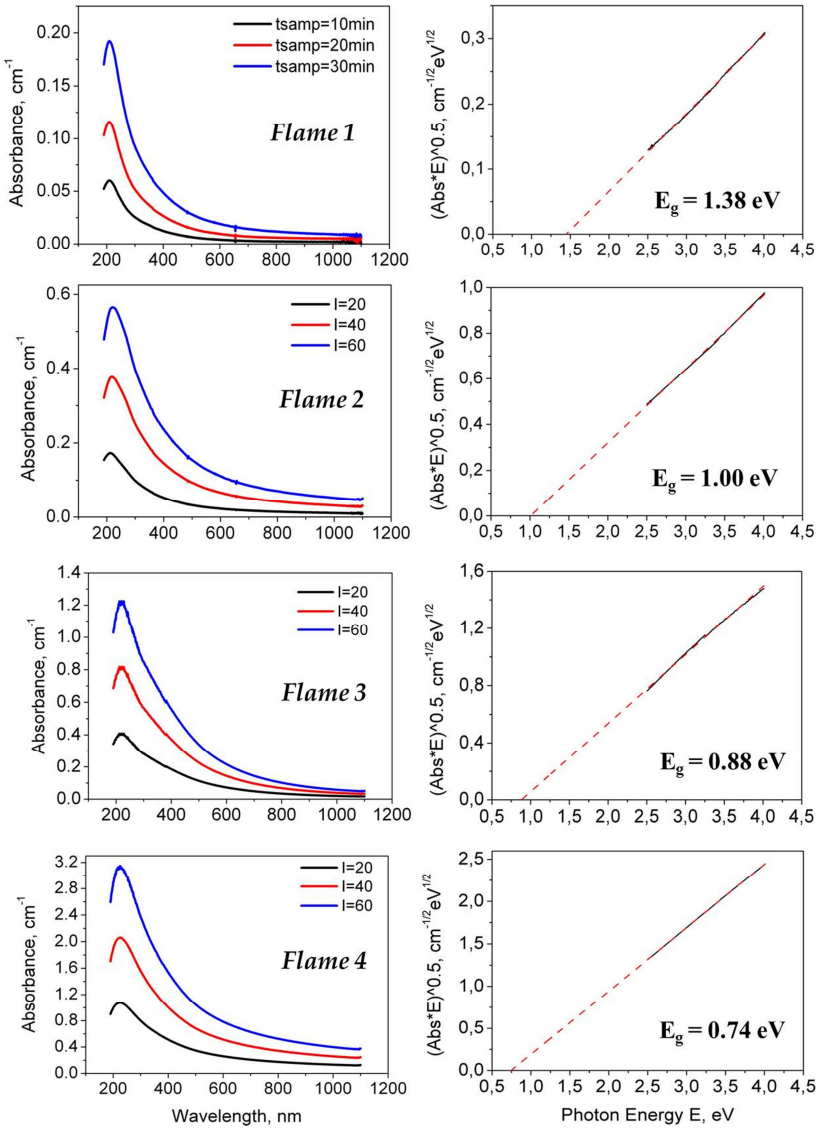

Figure 5.8. Absorption spectra of collected FFCNPs (left side). The spectra were recorded for different total sampling times. Tauc plots for tsamp=20 min (Flame 1), and I=40 (Flame 2, Flame 3 and Flame 4) (right side).

Structural and chemical characterization of the three samples has been conducted by Raman spectroscopy. Fig. 5.9 shows the first order and second order Raman spectra, and the results of a multiple peak fitting of the data performed using a procedure similar to that proposed by Sadezky el al. (2005).

The first order region is mostly dominated by two peaks, named as D and G peaks; additional Raman contributions (D3 and D" bands) can also be observed as shoulders in the first order region of spectra. The main difference found in spectra is an increase in the intensity of D band, compared to the G band, moving from Flame 1 sample to Flame 4 sample.

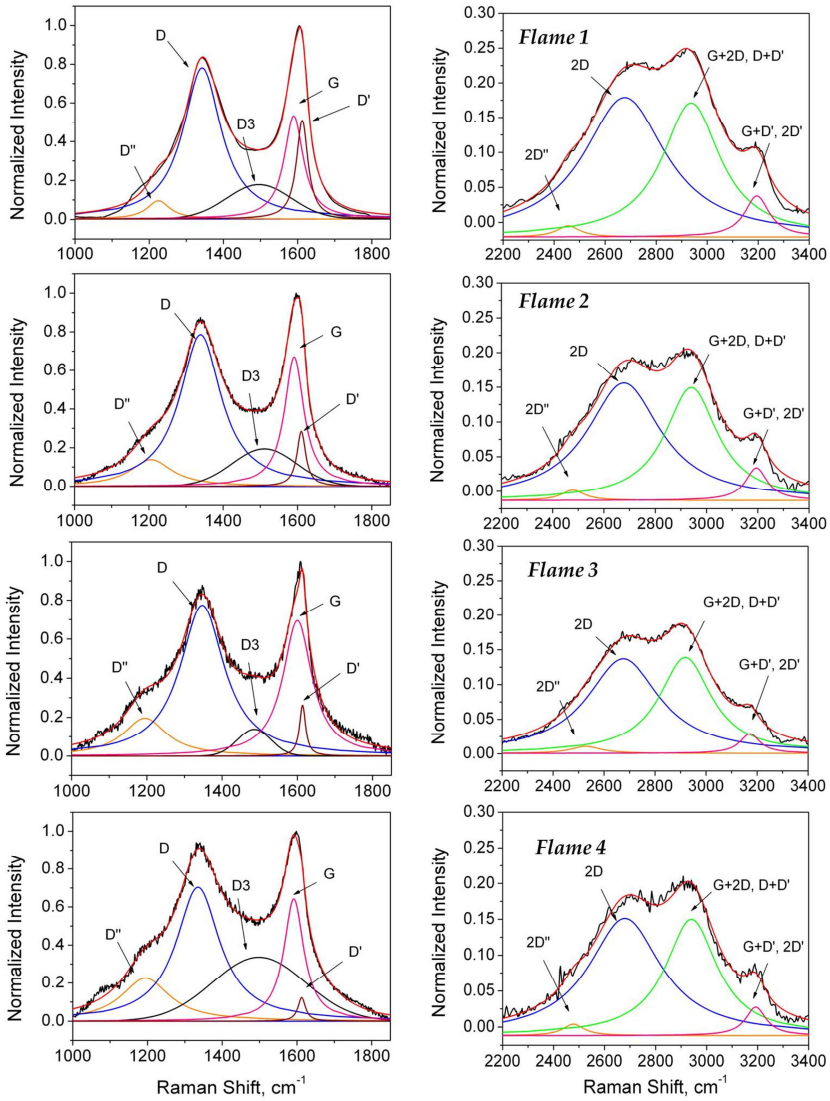

Figure 5.9. Curve fitting deconvolution for first order Raman spectra (left side) and for second order Raman spectra (right side). The single peak functions of the fit are also reported.

The second order region spectra are governed by a modulated bump, composed by three peaks (2D at ~2700 cm^{-1}, G+2D or D+D' at ~2950 cm^{-1}, and G+D' or 2D' at ~3200 cm^{-1}) and a shoulder (2D''or D+D'' at ~2450 cm^{-1}). Here, the main difference among samples is that the intensity of the modulated bump is reduced from Flame 1 to Flame 4. Different from 2D and 2D', the other two bands (G+2D and G+D') are defect activated, so that their presence can be always found in samples with a prevalence of nanoparticles, since particle border itself may contribute to edges effects and relevant distortion in the lattice may be expected as a consequence of the particle curvature (Nemanich and Solin, 1979).

All the investigated samples are characterized by very broad Raman bands, indicating highly disordered materials (Ferrari and Basko, 2013). In the first order Raman region, the ratio between the absolute intensity of the D peak and the G peak, I(D)/I(G), gives information about the degree

of ordering of the samples, as well as provides an estimation of the average size of the graphitic domain L_a. As reported in left side of Fig. 5.9, the ratio I(D)/I(G) increases moving from Flame 1 to Flame 4 sample. In the case of highly disordered materials, such as our samples, this trend indicates an increase of the probability to find aromatic rings in the sp^2 network and an increase of nanocrystalline order following a graphitization trajectory from Flame 1 to Flame 4 materials.
This trend can be quantified by evaluating the in-plane size of the aromatic islands, L_a, given by the following equation (Ferrari and Basko, 2013):

$$L_a^2 = 5.4 \cdot 10^{-2} \cdot E_L^4 \frac{I(D)}{I(G)} \tag{5.2}$$

with L_a in nm and E_L, the laser photon energy, in eV. The results are reported on top of each bar of the left graph of Fig. 5.10, showing a slight increase in L_a from Flame 1 to Flame 4.

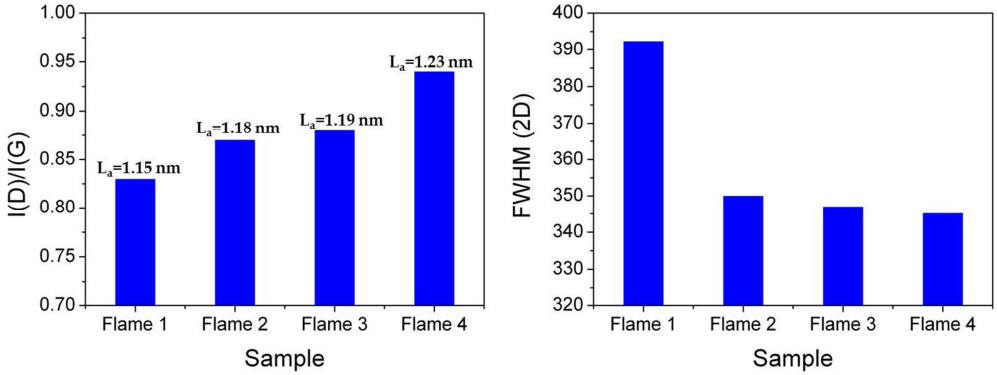

Figure 5.10. Intensity ratio I(D)/I(G) and L_a for the four flame sample (left side). Full Width at Half Maximum of the 2D band for the four flame samples (right side).

In the second order spectrum, the bandwidth of 2D line gives information about the stacking order of carbonaceous materials. Numerous works show that as the number of layers increases from graphene to multilayer graphene, the 2D band changes from single-line to multiple-line and, in the limit of a graphitic crystal, it becomes a doublet (Ferrari, 2007). The effect of a turbostratic arrangement of graphitic layers, or the increase of interlayer spacing, brings about the formation of a single line, which becomes broader the larger the interlayer spacing is. The correlation between the broadening of 2D band and the d_{002} interlayer distance measured by X ray technique was reported by Laspade et al. (1984), who therefore identified FWHM (2D) as a good graphitization index. In right side of Fig. 5.10 the FWHM (2D) is reported for the three flame-samples. Even though these values are larger than those reported for the graphitized materials by Lespade, variation of FWHM (2D) confirms that the three flames follow a graphitization trajectory: the reduction of FWHM(2D)

from Flame 1 to Flame 4 sample indicates an increase of the interlayer interaction, and so an increase of 3-dimensional order of the graphitic planes. It is interesting to note that in Flame 1 sample, I(D)/I(G) is the lowest while the I(2D)/I(G) is the largest, furthermore, the whole second order spectrum is sensibly more intense than that of the other two samples. In order to verify that such differences were not due to the different sampling method adopted for Flame 1 sample, we collected Flame 4 sample also on a filter with the same sampling probe used for Flame 1 sample. We did not observed significant differences in the spectra of the two samples collected from the same flame changing the sampling procedure. Thus, the peculiarities in Flame 1 sample spectrum are due to difference in the material itself. To analyze this point, we can go back over the origin of these Raman bands: both D and 2D bands are produced by the same phonons which are associated to vibrations of the whole aromatic ring. In the case of D band, the process involves one inelastic scattering by a phonon, and one elastic scattering event by a disorder, whereas in the case of 2D band the process involves two inelastic scattering events by phonons. In light of this, the lower extension of the aromatic network of the sample characterized by the lower I(D)/I(G) seems to be in contrast with the larger I(2D)/I(G). An explanation can be given considering how these bands appear in graphene, graphite and amorphous carbon. In a perfect graphene I(D)=0 and I(2D) is particularly intense (I(2D)/I(G) about 4) since it is due to a triple resonance process involving real states. In the three dimensional graphite, because of the change in the band structure, I(2D)/I(G) decreases to about 0.5; whereas, in disordered or turbostratic carbon compounds a further relaxation of the resonance occurs causing a strong broadening and reduction of 2D band intensity (Pimenta, 2007). In this light, the Raman features of the Flame 1 sample can be explained by the effect of a stronger resonance respect to the other samples, which should therefore reflect a significant difference in the electronic bands. It is likely that in this sample, which contains smaller aromatic islands, the lower three-dimensional order, responsible of the broadening of 2D line, reflects the presence of planar graphene-like nanoislands (Minutolo et al., 2014), which causes a stronger resonance than that exhibited by disordered turbostratic-like compounds, in Flames 2-4 samples.

5.2.3. Electrical characterization

We investigated also the electrical transport properties of our samples by measuring the current-voltage characteristics.

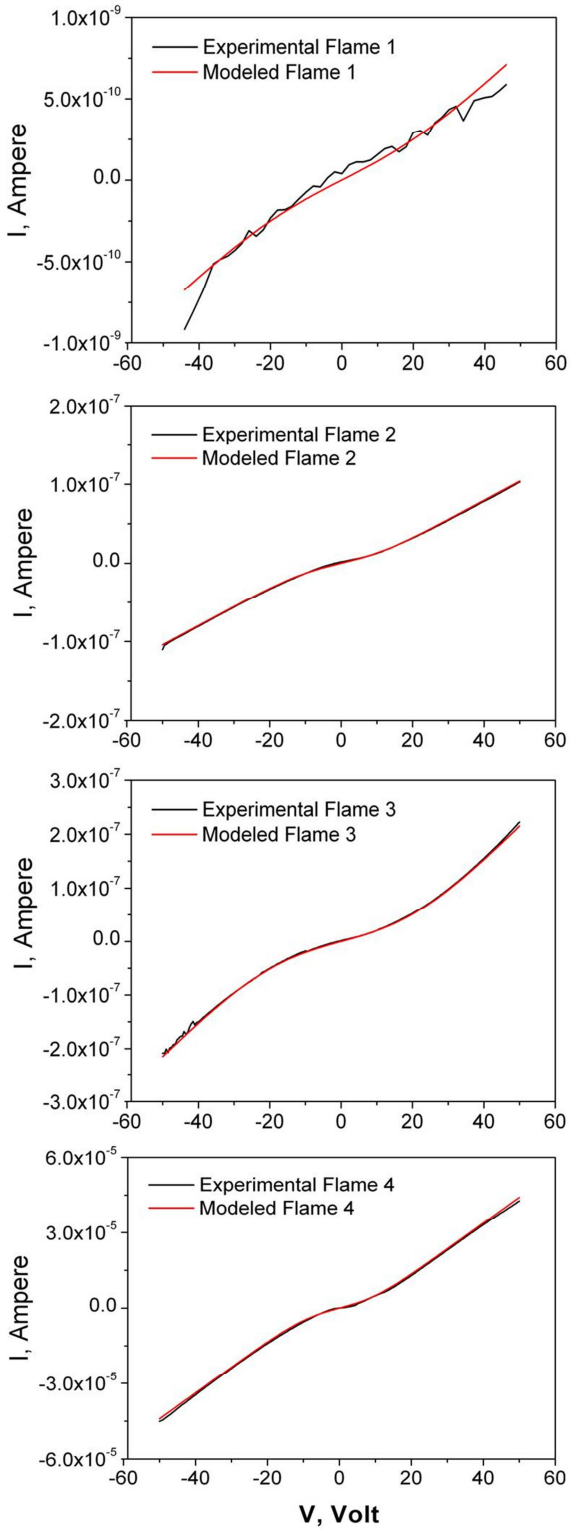

Figure 5.11. Experimental I-V characteristics (black lines) and best fits from Eq. (4) (red lines) for the four samples.

The I-V plot measured in the voltage range -50 V to 50 V is showed in Fig. 5.11 for samples collected from Flame 1, with a sampling time t_{samp}=20 min, and from Flames 2-4, with a number of

insertions I=40. The curves have a similar shape for the four samples. They are symmetrical and exhibit a non-linearity which addresses to a non-ohmic electrical behavior.

Since the four samples contained a different amount of material, we compared the electrical conductance of the samples by estimating the thickness of the carbon material deposited on the substrate, δ, from light absorbance Abs(λ) by means of Beer-Lambert law, and the imaginary part of the refractive index k(λ), using the following expression:

$$\delta = \ln(10)\lambda \frac{Abs(\lambda)}{4 \cdot \pi \cdot k(\lambda)} \tag{5.3}$$

Two wavelengths, namely 266 and 532 nm, have been used since at these wavelengths the refractive indexes are known for analogous materials. In particular, k(λ=266 nm)=0.08, typical of nanoparticles of organic carbon, has been used for Flame 1 and k(λ=532 nm)=0.56, typical of mature soot particles, has been used for Flames 2-4 (Cecere et al., 2010; Dalzell and Sarofim, 1969). It is worth noting that the k values adopted for the estimation of the δ are in good accordance with the absorbance per mass unit measured in the actual flame conditions. For the four samples, δ is: 52 nm (Flame 1), 40 nm (Flame 2), 42 nm (Flame 3) and 136 nm (Flame 4).

Electrical conductivity σ of the four materials has been estimated from Equation 5.4:

$$\sigma = G \frac{l}{d \cdot \delta} \tag{5.4}$$

where G is the electrical conductance, calculated as the slope of the I-V curves in the interval between 20 and 50 V, δ is the thickness of the deposit, l is the distance between the electrodes (l=0.1 cm) and d is the length of each electrode (d=0.5 cm). Figure 5.12 shows the electrical conductivity σ compared with the I(D)/I(G) ratio, derived from Raman spectra, for the four carbon materials.

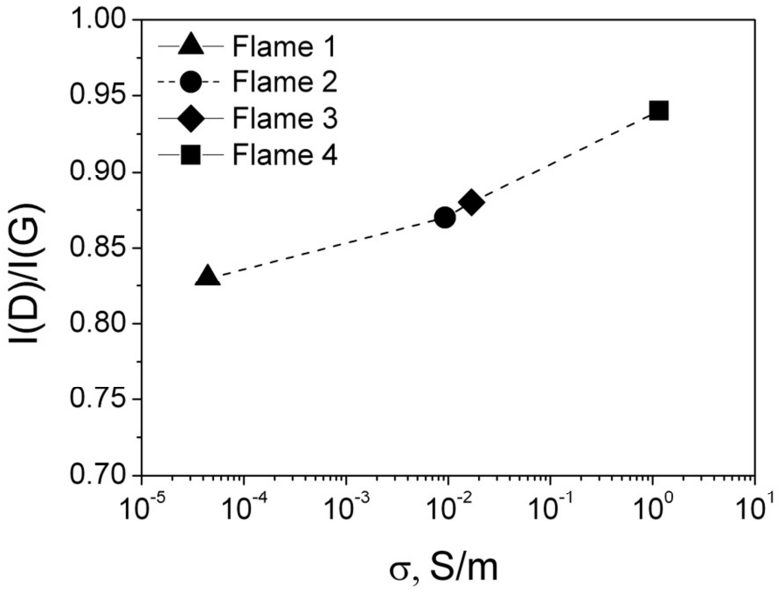

Figure 5.12. Intensity ratio I(D)/I(G) of Flames 1-4 samples as a function of electrical conductivity.

The increase of conductivity from Flame 1 to Flame 4 sample follows the increase of I(D)/(IG) and can be therefore correlated to the increase of the in plane size of graphitic crystallites within the particles, L_a, in agreement with the graphitization trajectory derived from Raman and optical band gap results.

In addition to a change in conductivity of the samples, current/voltage characteristics reported in Fig. 5.11 show that all the samples present a non-ohmic behavior typical of granular systems (Adkins, 1982). In these materials, the phenomenon of local electrical conduction can be described as tunneling of electrons between two neighboring particles in a percolative network (Balberg et al., 1990; Stauffer et al., 1994). Based on these assumptions, Bruschi and Nannini (1991) derived a theoretical equation that predicts the bulk I/V characteristic of a granular material in which the electrical conduction is governed by tunneling effect. In this model, the transfer of electrons from a particle to another, spaced by the so-called tunneling distance S, was associated to a variation in the electrostatic energy of the pair of particles E_{act}, which can be assumed to be the activation energy of the process. Thus, the bulk material, consisting of a layer of several particles packed together, as schematically shown in the picture of Fig. 5.13, can be approximated to a network of resistors from the electrical percolation theory and an exponentially decaying tunneling conductance between particles.

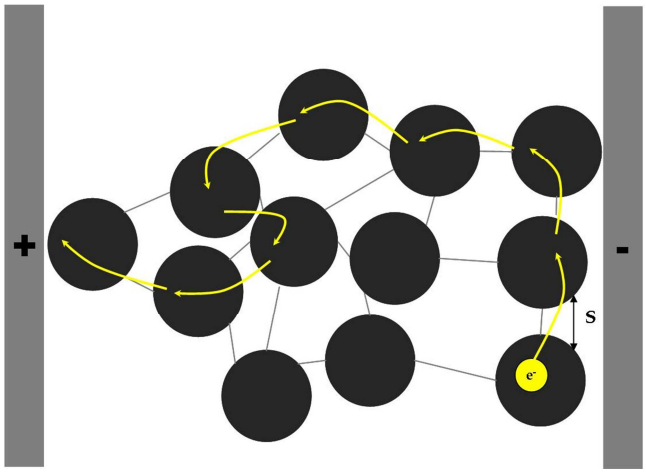

Figure 5.13. A schematic illustration of the electrical conduction phenomenon in a layer of particles, based on tunneling effect and percolation theory.

The I/V characteristic of a granular material derived by this model is given by:

$$I = C\left[\frac{A - BV}{\exp\left\{\frac{(A - BV)}{T} - 1\right\}} - \frac{A + BV}{\exp\left\{\frac{(A + BV)}{T} - 1\right\}}\right] \tag{5.5}$$

where A is proportional to the activation energy of the process E_{act} through the Boltzmann constant k_B, B is a constant dependent on both temperature and kind of material, and C has an inverse exponential dependence on the tunneling distance S.

Equation 5.5 at a temperature of 298 K has been used to fit the experimental I/V characteristics. As reported in Fig. 5.11, modeled curves furnish an excellent fit of the experimental data, proving that the model can be successfully applied to combustion-formed materials. The values of the parameters A and C obtained from the fit are reported in Fig. 5.14. The parameter A can be considered constant for the four samples within the experimental uncertainties. Consequently, the activation energy E_{act} is of the order of 50.0 ± 10.0 meV. On the other hand, moving from Flame 1 to Flame 4, the C parameter shows an exponential increase, which can be explained by a linear decrease of the tunneling distance.

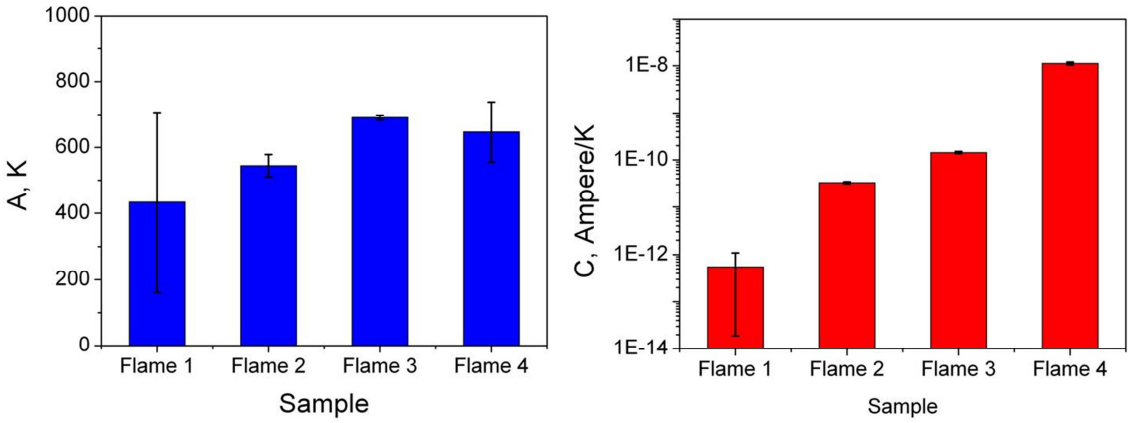

Figure 5.14. Parameter A (left side) and parameter C (right side) from the fit of I-V characteristics by Eq. (5.4) for the four samples.

To verify if the variation in tunneling distance could be a consequence of the different amount of material present on the substrates, we plotted in Fig. 5.15 the parameter C as function of the thickness of carbon deposit, δ. Furthermore, two additional points have been evaluated for the material collected for Flame 4 changing the number of insertions to cover a broader range of δ.

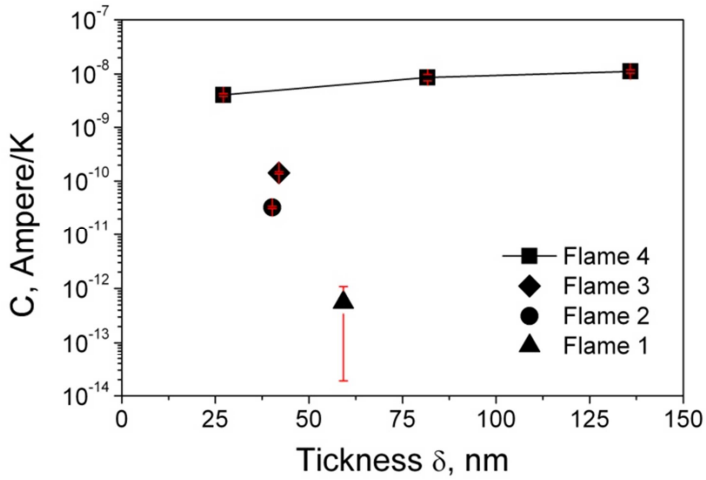

Figure 5.15. Parameter C obtained from the fit of I-V characteristics by Eq. (5.4) versus the thickness of the sample, δ.

From Fig. 5.15 it is clear that the C parameter is not strongly dependent on the amount of deposited material and a different thickness cannot justify the observed differences in the C parameter for the samples collected in the four flames. One possible explanation is that the electron percolation can be significantly affected by particle shape. To support this finding, AFM images of particles collected by thermophoresys on mica substrates in the four flame conditions are reported in Fig. 5.16. AFM images show that the shape of FFCNPs changes from single and isolated particles

to chain-like aggregates of primary particles moving from Flame 1 to Flame 4 samples, which can favor an increase in conductivity due to a closer inter-grain connection. One further possibility is that, besides inter-grain tunneling/percolation, intra-grain conduction also influences the macroscopic conductivity. Indeed, conduction in organic materials is often described in terms of Poole-Frenkel (P-F) emission (Stallinga et al., 2011). This mechanism is based on localized charges in trap centers and a field enhanced excitation of trapped electrons into the conduction band by means of a "hopping" mechanism that may be regarded as a percolation process, by which charges are transferred to neighboring trap centers. P-F mechanism in case of sparse ionization sites is described by the following relation (Pabst et al., 2007):

$$\sigma_{PF} = c\exp\left[-\frac{E_I}{k_B T} + \frac{1}{k_B T}\sqrt{\frac{q^3 V}{\pi\varepsilon_0\varepsilon_\infty d}}\right] \tag{5.6}$$

where c is a constant, E_I is the trap ionization energy, q is the electron charge, ε_0 is the vacuum permittivity, ε_∞ is the relative dielectric permittivity and d is the distance between electrodes. Conductivity vs. voltage experimental data were fitted by Equation 5.6 and the values of the barrier height of the P-F mechanism, i.e., the trap ionization energy, and dielectric permittivity were extracted from fitting results. Values of E_I are in the same order of magnitude of the activation energy E_{act} derived from tunneling model fitting, while dielectric permittivity ε_∞ was equal to $(7.2\pm0.75)*10^{-3}$ for Flame 1, $(1.3\pm0.02)*10^{-3}$ for Flame 2, $(1.2\pm0.07)*10^{-2}$ for Flame 3 and $(1.1\pm0.04)*10^{-2}$ for Flame 4. Since these parameters deviates significantly from dielectric permittivity derived from refraction index reported in literature (Cecere et al., 2010; Dalzzell and Sarofim, 1969), which is in the order of 10^{-1}, it is possible to conclude that Poole-Frenkel mechanism is not relevant in describing the macroscopic conductivity of FFCNPs. This result is consistent with the picture of the conductive network in our material as represented by sp^2 islands, and trap centers produced by disorder and sp^3 sites. Thus, contrarily to P-F theory, in our case the increase of trap center brings to a lower extension of the conductive sp^2 islands and a reduction of conductivity. We can therefore conclude that the governing mechanism for macroscopic conductivity in flame samples is the inter-grain conduction by a percolation/tunneling model.

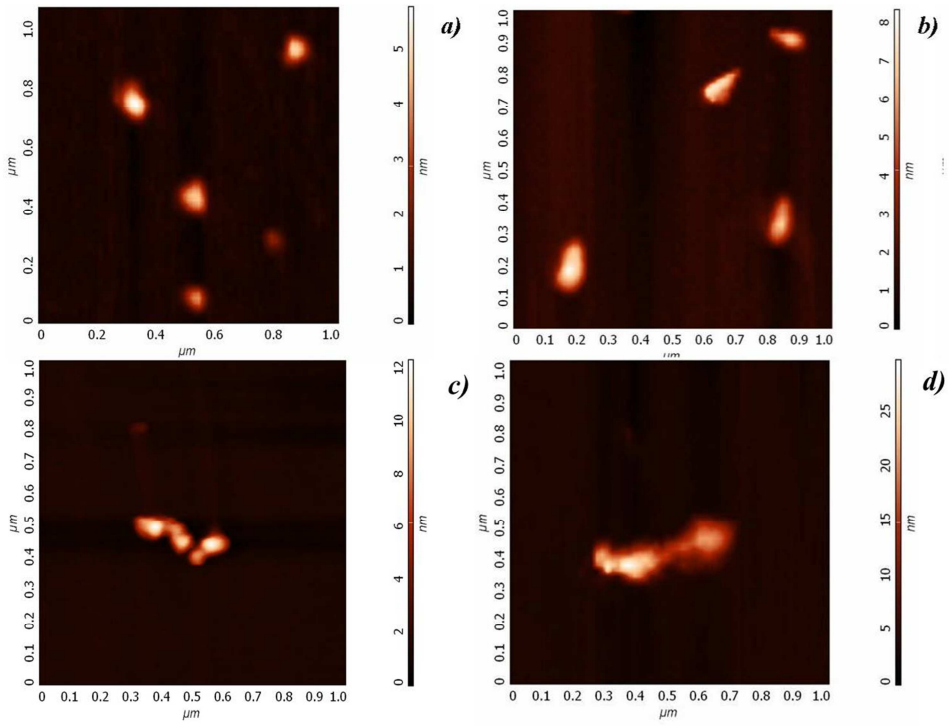

Figure 5.16. AFM images of isolated particles collected from Flame 1 (a), Flame 2 (b), Flame 3 (c) and Flame 4 (d).

What remains to be discussed is the effect of the flame parameters on particle conduction. The Flame 1 sample corresponds to the hottest flame, with a lowest C/O and particle residence time. The particles contain the smallest polyaromatic units, possibly arranged in planar graphene-like nanoislands within the carbon network, and particle coagulation produces single spherical particles by coalescence. It is likely that the extremely low conductivity of this sample is due to the low degree of both particle graphitization and inter-grain connections. Flame 2 and Flame 3 conditions have a similar particle residence time, but their C/O ratio is different. Particles have a similar composition in terms of degree of disorder, L_a extension and presence of crystallites; also, their shape suggests that particle agglomeration does not prevail over coalescence yet. The values of the electrical conductivity are very similar too, considerably larger than the previous case, but orders of magnitude lower than that of Flame 4 sample. It is likely that the conduction properties of primary soot particles are not strongly dependent on the flame stoichiometry. On the other hand, flame residence time seems to be a relevant parameter affecting particle conductivity. Indeed, the conductivity of particles collected in Flame 4 conditions, i.e. same equivalent ratio of Flame 3 sample but higher residence time, is orders of magnitude larger. Particles in these two samples have a similar graphitization degree while their main difference is the chain-like shape of the particles collected at a higher residence time, which is produced by particle agglomeration. The governing mechanism for conductivity in flame soot samples is thus probably the inter-grain conduction by percola-

tion/tunneling. Although the activation energy of this mechanism has been found to be rather constant for all conditions, it remains to verify if the improved percolation/tunneling observed is merely related to the chain-like shape of the particles or it is also due to changes in their surface properties.

5.3. Flame-formed carbon nanoparticles: morphology, interaction forces and Hamaker constant from AFM

This section reports the results concerning the work conducted by means of AFM on size, morphology and attractive and adhesive forces of flame-formed carbon nanoparticles.

The aim was to synthesize a wide pool of FFCNPs from an ethylene-air flame reactor operated in different flame conditions (from non-sooting to fully sooting), and to characterize their morphology and surface properties. Some of these properties, including particle size, aspect ratio, surface area and functional groups have been already investigated (Vander Wal and Tomasek 2004, Barone et al. 2003, Koch and Friedlander 1990). However, little is known about the forces, particularly van der Waals interactions, acting between carbon nanoparticles. Also, the Hamaker constants for FFCNPs (Minutolo et al. 1999; Sgro et al. 2003; D'Alessio et al. 2005), usually used in the calculation of the particle interaction potential, have been so far mainly retrieved theoretically based on particle chemical nature, since no direct experimental measurement can be found in the literature. So, the study we performed represents the first attempt to overcome the lack of experimental information in the literature about the interaction forces acting between FFCNPs, and also to furnish direct experimental measurements of Hamaker constant for FFCNPs.

Furthermore, it is widely accepted that particle coagulation represents a relevant controlling step in the process of FFCNPs synthesis. Several studies have been conducted over the years regarding the coagulation tendency of combustion-generated particles. The mechanism of collision and sticking of small particles can be viewed as due to a balance between the particle kinetic energy and the particle mutual interactions (van der Waals forces) (Narsimhan and Ruckenstein 1985); when particles are in the free molecular regime, at high temperature, such as those reached in flames, the particle kinetic energy may be higher than the interaction energy, resulting in a thermal rebound effect after collision (Wang and Kasper, 1991). Experimental results (Minutolo et al. 1999; Sgro et al 2003; D'Alessio et al. 2005) have confirmed this simple model showing that flame-formed nanoparticles with d=2-5 nm possess a rate of coagulation which is lower than that of larger soot particles (d=20-50 nm) and well below the value predicted by the gas-kinetic theory showing that the coagulation efficiency depends on particle size and morphology, and particle chemical structure. Moreover, temperature has been demonstrated to play a key role in determining the rate of coagulation of different sized nanoparticles (Sirignano and D'Anna 2013), also in different tem-

perature regimes. Characterization of FFCNPs surface properties is a way to deeply understand the role played by coagulation in their formation routes, and so to gain a control of the stacking of graphitic planes during FFCNPs synthesis process. Also, the knowledge of interaction forces can be useful to predict and control the tendency to agglomerate of synthesized nanoparticles when collected as films, and their physical interaction with solid and liquid interfaces.

5.3.1. Experimental set-up

The combustion reactor consists of a flat, atmospheric pressure, laminar premixed flame of ethylene and air, stabilized on a McKenna burner. Flame conditions and sampling position are reported in Table 5.5. Flame equivalence ratio Φ was changed in order to move from flame conditions with unimodal particle size distributions with average size of 2-4 nm (Φ=1.85 and 1.89), to flames with bimodal size distribution with a first particle mode at 2-4 nm and a second mode at 4-10 nm (Φ=1.95), up to fully-sooting conditions (Φ=2.16 and 2.58), in which 2-4 nm nanoparticles and 10-100 nm soot primary particles and aggregates are mainly produced. Table 1 reports the size ranges of the first and second mode of the size distribution measured by on-line Scanning Mobility Particle Sizer in previous works (Echavarria et al., 2009; Sgro et al., 2011; Commodo et al., 2013).

Table 5.5. Investigated flame conditions.

C/O Ratio	Equivalent Ratio Φ	Sampling Position, mm	Cold Gas Velocity, cm/s	D 1st mode, nm*	D 2nd mode, nm*
0.61	1.85	15	10	2-3 (Commodo et al., 2013)	
0.63	1.89	15	10	2-4 (Commodo et al., 2013)	
0.65	1.95	15	10	2-4 (Commodo et al., 2013)	4-8 (Commodo et al., 2013)
0.72	2.16	15	10	2-4 (Sgro et al., 2011)	10-50 (Sgro et al., 2011)
0.85	2.58	15	10	2-4 (Echavarria et al., 2009)	> 20 (Echavarria et al., 2009)

* The diameters reported for the first and second mode were measured by means of Scanning Mobility Particle Sizer, in similar experimental conditions.

Particles were collected at a fixed height above the burner (HAB=15 mm, corresponding to a residence times ranging from 27 to 33 ms as Φ increases from 1.85 to 2.58) by means of the thermophoretic pneumatic actuator. Residence time of the substrate in flame was kept constant at 30 ms. A single insertion of the substrate in flame was performed to collect particles for semicontact AFM morphological analysis, while multiple insertions (up to five) were performed for contact

AFM force spectroscopy measurements. Freshly cleaved mica muscovite disks, with a diameter of 9 mm, were used as substrates.

AFM measurements were performed at room temperature and 30% relative humidity.

For morphological imaging of samples, the instruments was operated in semi-contact mode in air, using NANOSENSORS™ SSS-NCHR super-sharp silicon probes with nominal tip radius of 2 nm, a 125-μm long cantilever with a spring force constant of 42 N/m and a range of resonance frequency 204 – 497 kHz. The AFM images were obtained with a scan rate of 0.3 – 0.5 kHz over selected areas of 2 μm × 2 μm and 1 μm × 1 μm (1024 × 1024 pixel resolution). All the images were not filtered.

For force-distance spectroscopy experiments, an NT-MDT CSG10/TiN contact probe was used, with a nominal tip radius of 35 nm and a titanium nitride coated silicon cantilever (length 225 μm, resonance frequency range 8 - 39 kHz, typical spring force constant 0.11 N/m). The correct value of the cantilever spring constant K_c was confirmed to be 0.11 N/m using the Sader Normal Script included in Nova Software, based on the dimensional approach method developed by Sader et al. (1999). The procedure to perform AFM force spectroscopy measurements involved two different steps. First, for each sample a topographical image of particles on substrate was acquired in contact mode over an area of 2 μm x 2 μm, in order to locate carbonaceous nanoparticles. Then, force measurements were performed on selected particles and repeated at least three times for each particle under the same conditions. More than 20 particles were selected for each flame condition, in order to have statistically relevant results.

5.3.2. AFM force-distance spectroscopy

In AFM force measurements, a sample is mounted on a holder attached to the piezoelectric element of the instrument. By applying a voltage to the piezoelectric translator, the sample is moved up and down, and the resulting cantilever deflection is measured by the optical lever method (Butt et al., 2005). This method is based on a laser beam which is pointed onto the cantilever, and the deflection leads to a shift of the reflected beam. This shift is detected by a four quadrant photodiode as an electrical signal called DFL, which is the difference between signals from top and bottom halves of the photodiode, and recorded as a function of the piezo displacement. The cantilever deflection δ_c can be then obtained dividing the DFL signal by the photodetector sensitivity, which is derived from the slope, in the hard repulsive contact region, of the curve obtained using cleaved mica as a hard material (Touhami et al., 2003). Knowing the cantilever spring constant K_c, the interaction force F acting between the probe and the sample can be simply obtained from the well-known Hooke's law as:

$$F = K_c \cdot \delta_c \tag{5.7}$$

The interactive force-piezo displacement curve, measured on a particle collected at Φ = 2.58, is reported in Fig. 5.17. Initially, the tip is far away from the sample. When the piezoelectric translator starts moving toward the probe, there is no measurably interaction between the probe and the sample, thus the cantilever is not deflected and only the physical separation between the two bodies changes, point (a) in Fig. 5.17. As the sample approaches the tip, they experience an attractive force that results in an instability called "Jump-to-contact" and the cantilever undergoes a rapid deflection when the force gradient exceeds the spring constant, point (b) in Fig. 5.17, (Senden 2001).

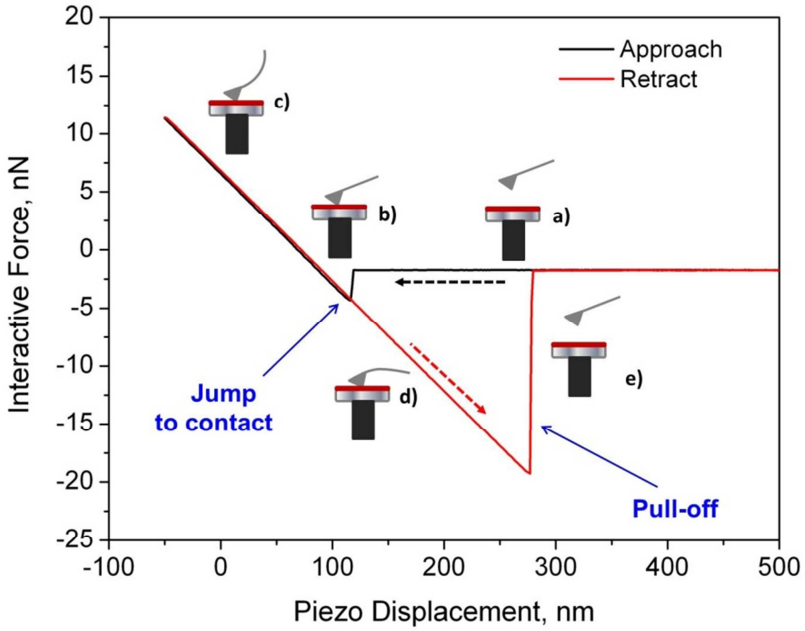

Figure 5.17. A typical force distance curve, as obtained from AFM. The black line refers to approach of the cantilever to the sample surface, while the red line refers to retraction from the sample surface.

The measure of the cantilever deflection caused by the "Jump-to-contact" gives the value of the attractive force, F_{att}, acting between the sample and the tip according to eq. 1. Then, the translator moves further, and the deflection of the cantilever is linearly proportional to the movement of the piezo, point (c) in Fig. 5.17. Subsequently, the sample surface is retracted, point (d) Fig. 5.17, and the adhesive forces between the two bodies hold the probe to the sample until the spring constant overcomes the force gradient (Lomboy et al. 2011) and the "Pull-off" instability occurs, point (e) in Fig. 5.17. The adhesive force, F_{adh}, can be acquired from the cantilever deflection during the "Pull-off".

5.3.3. Morphological analysis

Before measuring attractive and adhesive forces, an accurate characterization of particle morphology and dimension has been performed running AFM in semi-contact operation mode. This technique allows achieving a higher resolution along vertical and lateral axes, compared to the contact mode, since it avoids strong tip-sample interactions and attenuates undesirable convolution effects (Barone et al. 2003). For all the experimental flame conditions, particles were collected by single insertion. This procedure ensured to collect a sufficiently high number of particles for a statistical analysis, but low enough to avoid interaction between the collected particles on the substrate.

Figure 5.18 shows AFM typical topographical images of isolated particles collected from the different flames, together with corresponding height profiles. The vertical axis is reported as a color-map scale.

Topographic images were used to measure the maximum height H_{max} and the base diameter D_{base} of the particles, which were used to estimate the particle volume by assuming a cone shape for the impacted particle with a base diameter corresponding to D_{base} and a height corresponding to H_{max}. The particle equivalent diameter was then calculated from the measured particle volume, under the hypothesis of a spherical shape. AFM images are measured along vertical axes with a large resolution, of the order of 0.1 nm, as compared to the lateral resolution which is limited by tip convolution effects. We considered that base diameter was overestimated by about two tip radii, and subtracted this value in the evaluation of the base diameter of the measured objects (see Section 5.1.2). Even so, particle height is always much lower than particle base diameter showing that the shape of the particles collected on the sampling plate is not spherical. In order to obtain results that may be compared to the diameter of the particles measured in aerosol phase by Scanning Mobility Particle Sizer, the particle volume equivalent diameter was therefore calculated from the measured particle volume, under the hypothesis of a spherical shape. Particles sampled in flames with equivalence ratios ranging from 1.85 to 1.95 have a volume equivalent diameter in the range of 2.3 - 5 nm. Richer flames, namely those with Φ=2.16 and 2.58, show a bimodal size distribution function with the first mode centered at about 2.5 nm and the second particle mode which moves from 11 to 25.2 nm as flame richness increases. These results are consistent with the size distribution of the particles in aerosol phase measured by SMPS and reported in literature (see Table 5.3). Such agreement confirms that the sampling procedure allows collecting the same particles which are formed in flame and that the flat shape measured by AFM is the result of particle deformation caused by their impact on the substrate during the sampling and by adhesion forces on the mica.

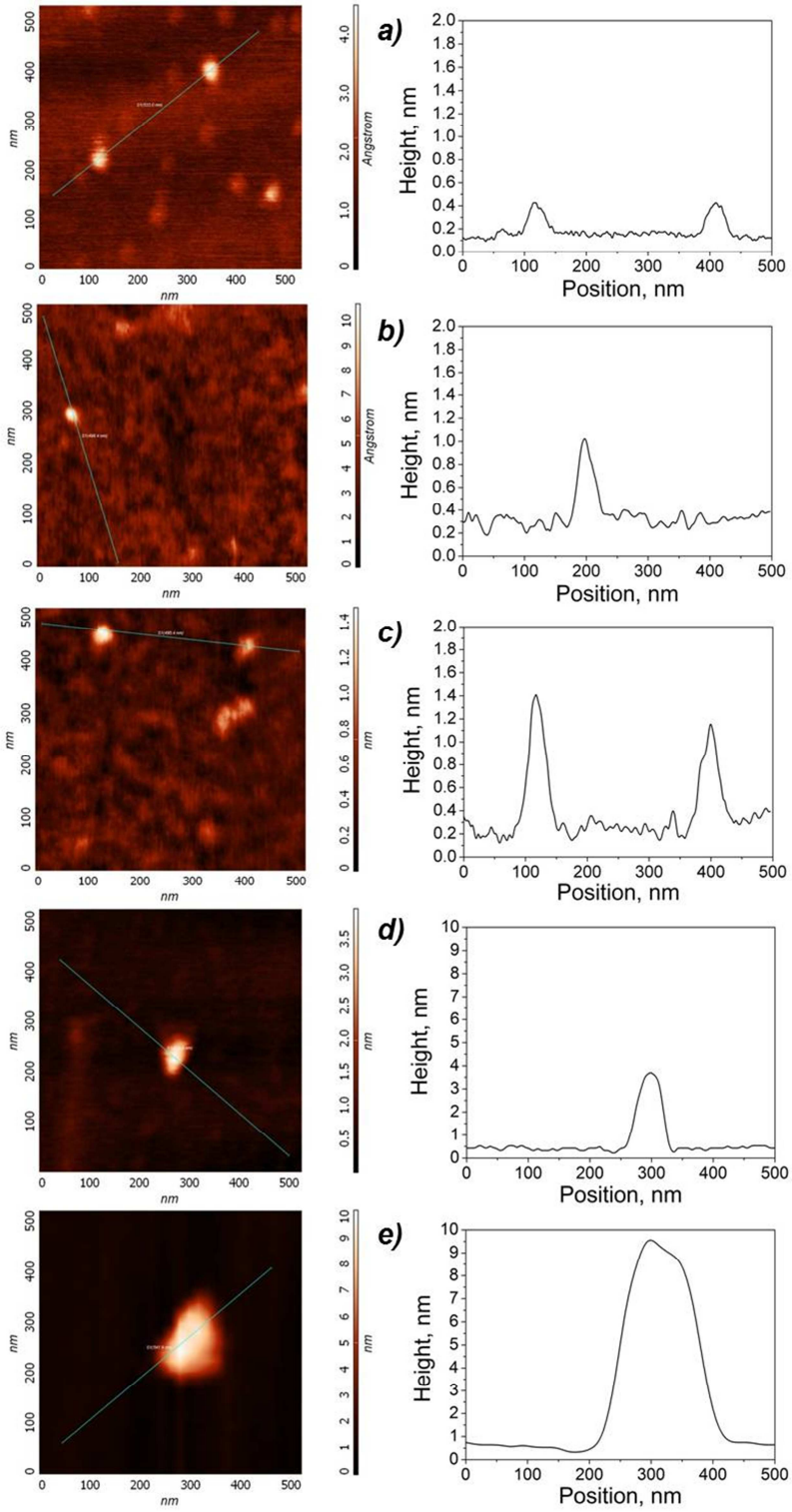

Figure 5.18. AFM semicontact images of isolated particles collected from different flames (left), and corresponding height profiles along the green line (right): a) Φ=1.85; b) Φ=1.89; c) Φ=1.95; d) Φ=2.16; e) Φ=2.58.

Figure 5.19 reports the measured maximum particle height H_{max} as a function of the estimated particle equivalent diameter. Particle height is always much lower than particle base diameter showing that the shape of the particles collected on the sampling plate is not spherical. For the larger-size particles the height reaches values of about 0.4 times the equivalent diameter, whereas for the smaller ones, the height is of the order of 0.05 - 0.1 times the particle equivalent diameter, i.e. heights are of few angstroms (see the expanded plot, Fig. 5.19b).

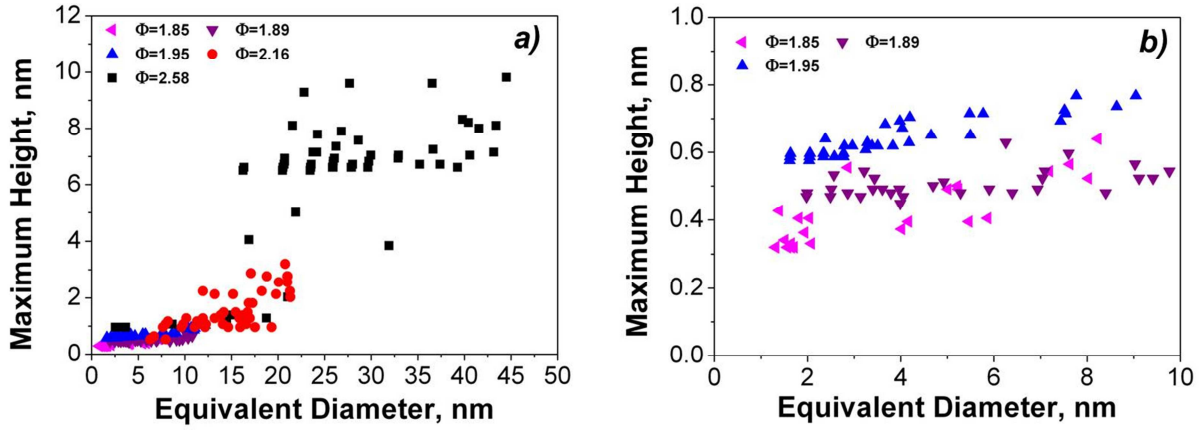

Figure 5.19. Distributions of particle maximum height as a function of equivalent diameter (a). Magnification of plot (a) in the range H_{max} = 0-1 nm for flames at Φ=1.85, Φ=1.89 and Φ=1.95 (b).

As discussed in Section 5.1, the reasons why they have an almost atomic-thick and disk-like shape may be a consequence of the particle molecular structure and the deposition/sampling procedure. Indeed these compounds are probably small, defective graphene-like sheets which have a crumbled, three dimensional shape in the aerosol phase, due to the possibility of twisting and bending around non-aromatic bonds at the high temperatures of the flame, but they assume a plane, atomic-thick morphology when they collide and deposit on the mica support (Minutolo et al. 2014). It is worth to note that moving from the less rich flames (Φ=1.85 and 1.89) where the particles typically have a height of about 0.45 nm, i.e., they are atomically thick, to the flames with Φ=1.95, the particle height increases to 0.70 nm, thus indicating the formation of stacked molecular clusters.

5.3.4. Attractive and adhesive forces

To perform force-distance spectroscopy measurements, thermophoretic sampling was carried out inserting up to five times the substrate in the flame keeping constant the residence time at 30 ms.

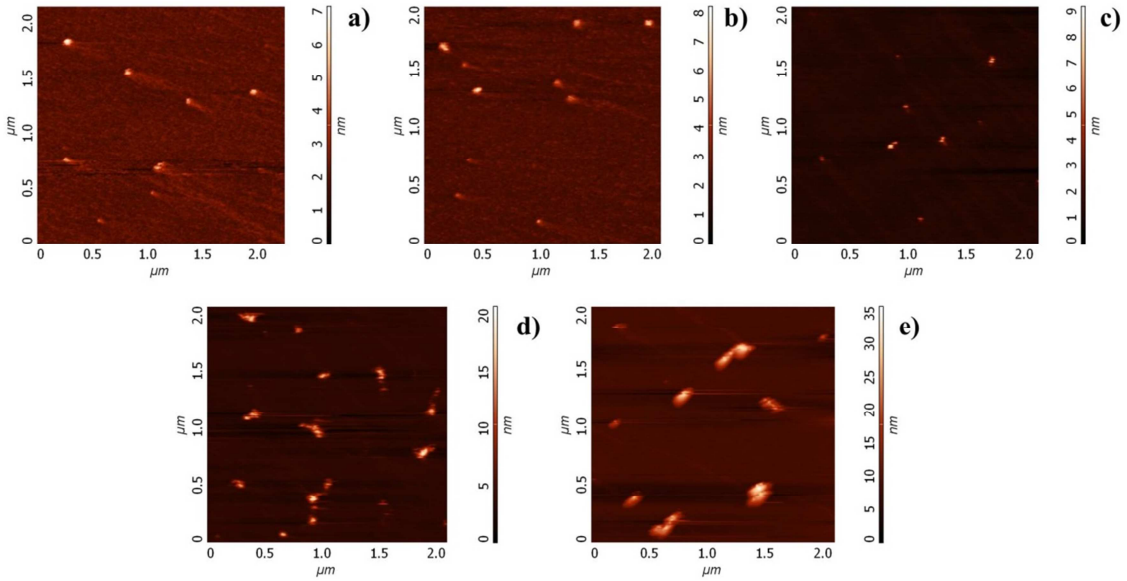

Figure 5.20. AFM contact images of isolated particles collected from different flames: a) Φ=1.85; b) Φ=1.89; c) Φ=1.95; d) Φ=2.16; e) Φ=2.58.

This procedure was used to accumulate more material, in order to have a thickness of the material deposited on the substrate high enough to avoid that interaction forces between the AFM tip and the mica muscovite substrate may affect the measurement of the interaction between the AFM tip and sampled particles. Furthermore, as explained in the experimental section, force spectroscopy is a two-step procedure since a preliminary topographic imaging is needed to locate particles on which force measurements are performed in the second step. With a multiple insertions sampling, the accumulation of larger quantities of particles on the substrate allows a more accurate positioning of the tip on the selected portion of material for force measurements. It is worth noting that this sampling procedure induces agglomeration and aggregation of the particles on the substrate and hence it is used only for retrieving surface properties of the sampled material and not morphological and size properties. Figure 5.20 shows contact mode AFM topographic images of particles collected from the different flame conditions. The entire ensemble of particles clearly has higher base diameter and heights, with respect to those estimated from semi-contact images.

The experimental force-distance curves measured during the approach phase on two particles collected respectively from flame Φ=1.85 and flame Φ=2.58 are reported in Fig.5.21 as representative of the two extreme experimental flame conditions. For both conditions the "Jump-to-contact" phenomenon is observed. The values of the attractive forces between the particle and the probe-tip, as derived from the curves, are indicated by arrows.

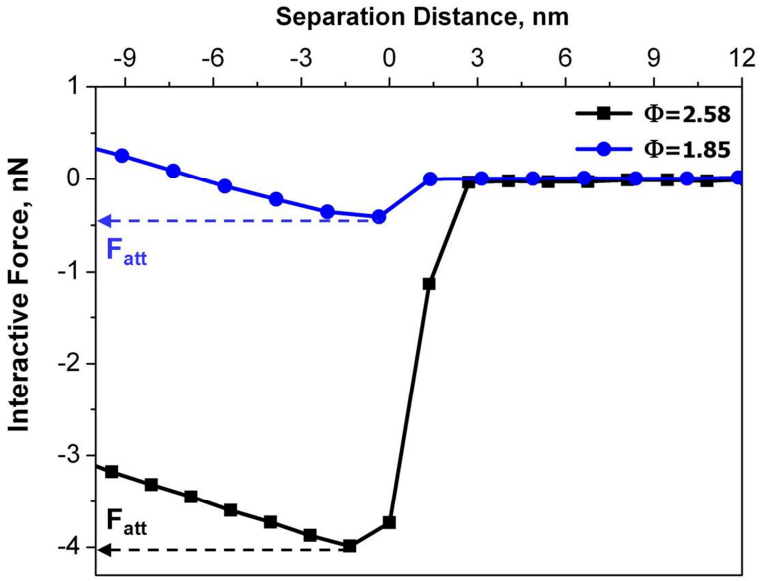

Figure 5.21. Experimental force-distance approach curves measured for a particle collected at Φ=1.58 (blue dots) and a particle collected at Φ=2.58 (black squares). Arrows indicate the values of the attractive forces.

Attractive forces have been also measured collecting different amounts of the aggregated material deposited on the mica substrates for all the experimental flame conditions, by varying the total residence time of the substrate in flame. Measured attractive forces clearly show that forces are independent on the amount of the collected material, i.e. the volume of the sampled material under investigation, while they are sensitive only to particle nature.

Figure 5.22 reports the measured attractive forces for the investigated experimental conditions as a function of the flame equivalence ratio. Attractive forces were measured also for both freshly cleaved mica disk and highly ordered pyrolytic graphite (HOPG) samples, and reported in the same figure for comparison. Cleaved mica is the material on which particles are deposited whereas HOPG is a high purity graphitic structure and can be considered as a reference in the analysis of the properties of mature soot.

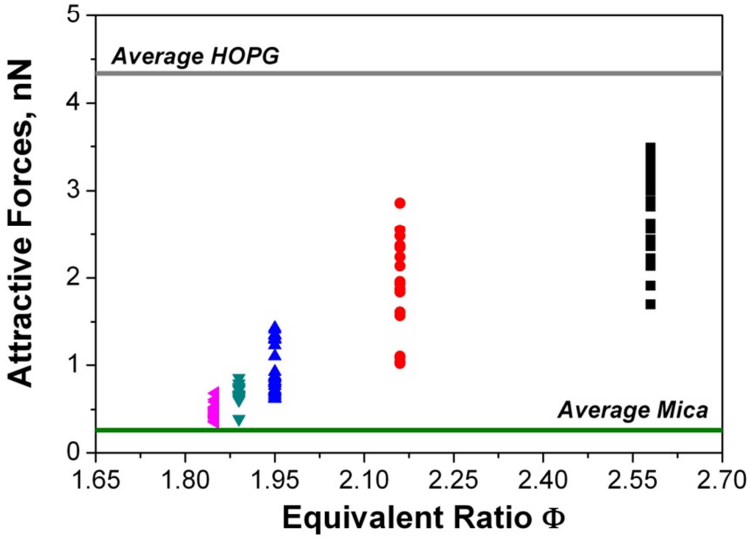

Figure 5.22. Attractive forces between the particle and the probe-tip as a function of flame equivalence ratio (bottom axis). The average values measured on mica and HOPG are also reported as green and grey line respectively.

As discussed above, particles produced in flames with equivalence ratios Φ less than 2 possess a very narrow distribution of diameter well below 10 nm. In these conditions, a distribution of attractive forces of the order of 0.5 ± 0.2 nN for Φ=1.85, and 0.6 ± 0.2 for Φ=1.89 is measured. These values are slightly higher than mica average attractive force which is of the order of 0.3 ± 0.1 nN (continuous green line in Fig. 5.22). Flame with Φ=1.95 shows a broader distribution of diameters, with a mean size of 5 nm (as derived from semi-contact measurements) and attractive forces of the order of 1.0 ± 0.4 nN. Particles generated from flames with Φ=2.16 and Φ=2.58, which comprise both nanoparticles and soot particles, have a very broad distribution of attractive forces, 2.0 ± 0.9 nN for Φ=2.16 and 2.6 ± 0.9 nN for Φ=2.58. The highest measured values are however lower than the average value measured for HOPG which is of the order of 4.3 ± 0.4 nN (continuous grey line in the figure).

Measured adhesive forces for the investigated experimental conditions, as a function of both flame equivalence ratio and average particle equivalent diameter derived from semi-contact topographic measurements, are reported in Fig. 5.23, together with the average measured values of adhesive force for HOPG (33 ± 3 nN) and mica (1.9 ± 0.6 nN). The distribution of F_{adh} shows a very similar trend to that of F_{att}, with an increase of measured force as equivalence ratio of investigated flame increases. For flame conditions Φ=1.85 and Φ=1.89, F_{adh} are of the order of 4 ± 2 nN.

Slightly higher values of F_{adh} are measured at Φ=1.95, in the range 5 ± 2 nN. Finally, at Φ=2.16 and Φ=2.58 the value of F_{adh} is 11 ± 3 nN and 13 ± 5 nN, respectively.

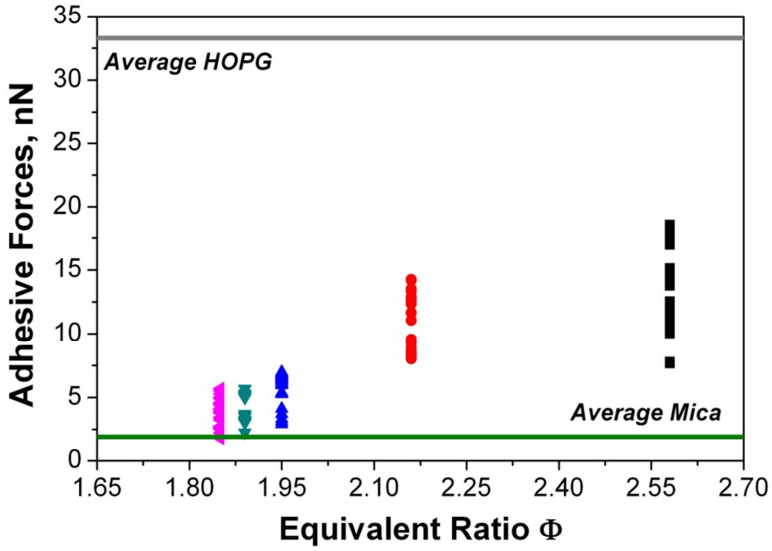

Figure 5.22. Adhesive forces between the particle and the probe-tip as a function of flame equivalence ratio. The average values measured on mica and HOPG are also reported as green and grey line respectively.

For each flame condition, the adhesive force is typically 6 to 8 times greater than the attractive force. This occurs in all the force-distance curves acquired during the experiments and is evidenced by the presence of a hysteresis as shown in Fig. 5.17. The larger F_{adh} is due to the formation of adhesive bonds between tip and particle surface during contact in addition to a possible deformation of the particle around the tip, which may be responsible of an increase in contact area (Burnham et al. 1990; Weisenhorn et al. 1992). In force-distance measurements, the presence of hysteresis can be also attributed to the interactions of capillary fluids covering both the tip and the sample due to ambient humidity (Hashemi et al. 2008). In order to exclude any interference of capillary forces during measurements the experiments were repeated using a flow of nitrogen in the AFM protective hood to keep relative humidity below 5%. No differences in the curves acquired in air and pure nitrogen atmosphere were noticed.

5.3.5. Hamaker constant of FFCNPs

From the measurement of attractive forces between the particle and the probe-tip, the Hamaker constant of carbon nanoparticles in the different experimental flame conditions was derived. The main assumption made is that van der Waals force F_{vdW} is the predominant contribution

to the interaction forces acting between tip and particle during approach phase. Indeed, since interactions were measured at small separation distances (less than 30 nm), electrostatic forces can be considered negligible (Gady et al., 1996). The method used to derive the Hamaker constant is based on fitting the curve of the attractive force measured by AFM as the cantilever approached the surface (Fig. 5) at small separation distance with the expression for the van der Waals forces between a sphere and a flat plane in the Derjaguin approximation (Hamaker, 1937; Israelachvili, 2011), given by:

$$F_{vdW} = -\frac{A_{tip-particle} R_{tip}}{6D^2} \tag{5.8}$$

where R_{tip} is the radius of the tip, D is the tip-particle separation distance and $A_{tip\text{-}particle}$ is the Hamaker constant corresponding to the system tip-particle. The Hamaker constant for the solely particles, $A_{particle}$, was obtained from the following equation (Eichenlaub et al., 2002):

$$A_{tip-particle} = \sqrt{A_{tip} * A_{particle}} \tag{5.9}$$

where A_{tip} is the Hamaker constant of titanium nitride TiN, $1.57*10^{-19}$ J, (Bergstrom 1997). The method was first tested by using Eq. 5.8 to fit the measured approach force-distance curves of freshly cleaved mica disks and HOPG. The resulting Hamaker constant was $0.90 \pm 0.03*10^{-19}$ J for mica and $4.6 \pm 0.5*10^{-19}$ J for HOPG. These values are in good agreement with the Hamaker constants reported in the literature, which are in the order of $0.99 \pm 0.01*10^{-19}$ J and $4.7 \pm 0.3*10^{-19}$ J, respectively for muscovite mica (Hamaker 1937; Hashemi et al. 2008) and HOPG (Sgro et al. 2003; Israelachvili 2011).

The same procedure was applied to all the force-distance curves acquired for the investigated particles, and an average value of the Hamaker constant for the five experimental conditions was calculated. The results are summarized in Table 5.6. For comparison, the table also reports the Hamaker constant for HOPG, benzene and aliphatic hydrocarbons as reported in the literature. Hydrocarbon combustion-generated particles of 2-4 nm are often considered to be comprised of few aromatic rings linked by aliphatic bonds, so the Hamaker constant of benzene and aliphatic hydrocarbons represents a lower limit given by the smallest building blocks of the particles. By contrast, the Hamaker constant of HOPG can be considered as an upper limit given by a perfect graphitized structure.

Table 5.6. Average Hamaker constants.

	Hamaker Constant A, 10^{-19} J
HOPG	4.7 ± 0.3 [a]
Particles at Φ=2.58	3.5 ± 1.6 [b]
Particles at Φ=2.16	2.2 ± 0.9 [b]
Particles at Φ=1.95	1.5 ± 0.5 [b]
Particles at Φ=1.89	0.98 ± 0.01 [b]
Particles at Φ=1.85	0.95 ± 0.01 [b]
Benzene	0.5 [c]
Aliphatic	0.1 [c]

[a] Lee et al., 2002
[b] This thesis
[c] Israelachvili, 2011

Soot particles produced in very fuel-rich flames (Φ=2.16 and Φ=2.58) have a Hamaker constant slightly lower than that of HOPG. Those particles and graphitic materials exert similar interaction forces as confirmed by the attractive force values reported in Fig. 6. On the other hand, carbon nanoparticles formed below the soot limit appearance, i.e. Φ=1.85-1.95, have a value of the Hamaker constant much lower than that of the soot particles, consistently with a less graphitic content due to smaller aromatic domains and probably the lack of staked aromatic domains. The trend of the Hamaker constants, as well as of both attractive and adhesive forces, with flame equivalent ratio, compared to values of benzene and HOPG, indicate a continuous increase of particle's aromatic domains and three-dimensional order by increasing the flame equivalent ratios.

6. Production and characterization of inorganic nanoparticles

In this chapter, results concerning the production via flame synthesis and the subsequent dimensional and physical-chemical characterization of pure magnesium oxide (MgO) nanoparticles and titanium dioxide (TiO_2) nanoparticles are reported, using the aerosol flame synthesis developed during this thesis work and described in section 4.1, operated in fuel-lean conditions.

6.1. Magnesium oxide nanoparticles

The first material we decided to produce and investigate was magnesium oxide. MgO is one of the most promising materials in the field of nanosized particles; the large surface area to volume ratio and the presence of reactive sites on the surface make MgO nanoparticles suitable for uses in a number of organic heterogeneous catalyst (Ganguly et al., 2011). Other possible fields of application are temperature and humidity sensors (Shukla et al., 2004) and cryosurgery (Di et al., 2012) due to low cost, electro-stability, non-toxic, and biodegradable properties of MgO nanoparticles.

6.1.1. Experimental set-up

The AFS system was operated using ethylene as fuel and air as oxidant, in order to generate a burned stabilized, flat, fuel-lean atmospheric premixed flame (equivalent ratio Φ =0.60, cold gas velocity=100 cm/s). A sheath flow of Argon (65 Nl/hr) was used to isolate the flame from the surrounding air. The flame was doped with precursor solutions of magnesium nitrate hexahydrate $Mg(NO_3)_2 \cdot 6H_2O$ (Aldrich, 99%) into ethanol (corresponding vapour flow rate 8.8 Nl/hr), at three different concentrations (4%, 6% and 8% by mass of Mg precursor). Resulting luminous flame height was 18 cm, corresponding to a particle residence time of 33 ms.

Particles were collected by means of the thermophoretic pneumatic actuator on mica sheets for AFM analysis and on aluminum substrates for SEM analysis. Samplings was performed at three different heights above the burner HAB (50 mm, 75 mm and 100 mm), corresponding to residence time inside the reactor of 6.3 ms, 10.3 ms and 15 ms.

AFM measurements were performed at room temperature and 30% relative humidity, operating the instrument in semi-contact mode in air using NANOSENSORS™ SSS-NCHR super-sharp silicon probes with nominal tip radius of 2 nm, over selected areas of 8 μm × 8 μm (1024 × 1024 pixel resolution).

Characterization of flame temperature was carried out using an R-type thermocouple (Pt/13%Rh vs. Pt), substituting precursor solutions with pure ethanol to prevent nanoparticles depo-

sition on thermocouple junction. Flame temperature was measured every centimeter above the burner from 18 cm down to 10 cm; below 10 cm the temperature reached a value higher than 2000 K, which is above the maximum operating level of the thermocouple. Therefore, the temperature in the flame front was first calculated as the adiabatic flame temperature by means of heat and mass balances, using the code GENPOL; then, temperature profile from flame front temperature to first measurable data was approximated by a linear interpolation between these two values. Flame temperature profile, obtained coupling experimental and modeled data, is reported in Figure 6.1.

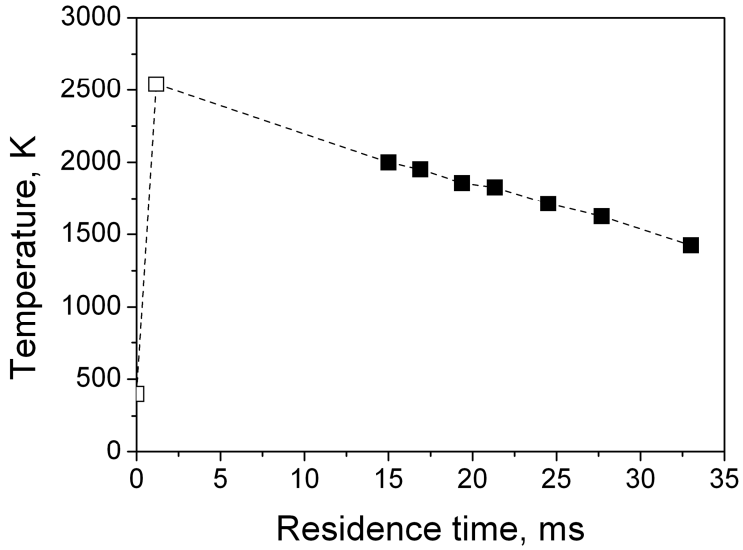

Figure 6.1. Flame temperature profile along the axis. Filled symbols are experimental data; open symbols are modeled data.

6.1.2. Particle characterization

The formation of Magnesium oxide particles in flame is attributed to the thermal decomposition of magnesium nitrate (Mu and Perlmutter, 1982). The evaporation of magnesium nitrate droplets (melting point 361.9 K; boiling point 603 K) firs occur, giving free gas phase molecules of $Mg(NO_3)_2$, which then form MgO according to the reaction: $2\ Mg(NO_3)_2 \rightarrow 2\ MgO + 4\ NO_2 + O_2$ (T=683 K).

Samples for SEM analysis were obtained by thermophoretic collection performed on aluminum substrates with high insertion times (70-100 ms) and a great number of insertions (50-100), due to the need to collect enough material for elemental composition analysis.

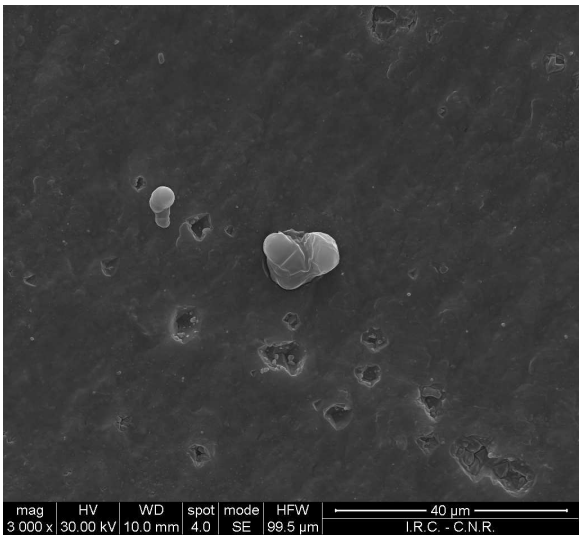

Figure 6.2 SEM image of particles collected on aluminum substrate by 100 insertions at 50 ms, HAB=100 mm, Mg Nitrate concentration=6%.

A typical SEM image, reported in Figure 6.2, shows the presence of big agglomerates, probably due to the long residence time of the substrate in flame, while ultrafine particles are not detectable, since their sizes are below the instrumental resolution. EDXS analysis of these particles confirmed that particles are composed by Magnesium (Mg) and Oxygen (O).

Dimensional characterization was performed by means of AFM on isolated particles collected by thermophoresys with a single insertion of 30 ms. AFM image analysis conducted on a statistically representative sample of about 50 particles over an area of 8 µm x 8 µm and then analyzed to obtain volume, base area and maximum height of the particles. Particle volume was evaluated from the base diameter and height considering a conical shape, and the distribution of the diameter D_p of spheres with equal volume was finally determined. The particle size distributions (PSDs) were then fitted by a sum of two lognormal distribution functions, shown in Equation 6.1.

$$\frac{1}{N}\frac{dN}{dD_p} = \frac{w}{D_p\sqrt{2\pi}\ln(\sigma_1)}\exp\left(-\frac{\ln(D_p/<D_{p1}>)}{2\ln(\sigma_1)}\right)^2 + \tag{6.1}$$

$$+\frac{1-w}{D_p\sqrt{2\pi}\ln(\sigma_2)}\exp\left(-\frac{\ln(D_p/<D_{p2}>)}{2\ln(\sigma_2)}\right)^2$$

Where D_p is the particle diameter, $<D_p>$ is the mean particle diameter, N is the number density of the particles, σ is the geometric standard deviation and w is the particle number fraction.

The parameters derived from the fit of the size distribution function, obtained at three different HAB (50 mm, 75 mm, 100 mm) for all the three concentrations (4%, 6%, 8% of Mg precursor), are reported in Table 6.1.

Table 6.1. Parameters used to fit the AFM log normal PSDs.

Mg Nitrate	*Residence time (ms)*	*Mean Diameter (nm)*		*Standard Deviation*		*First mode weight*
		$\langle D_{P1} \rangle$	$\langle D_{P2} \rangle$	σ_1	σ_2	w
4%	6.3	6.98	10.6	1.05	1.11	0.85
	10.3	9.1	29.6	2.12	1.2	0.75
	15	14.13	40	1.29	1.23	0.622
6%	6.3	9.41	12.8	1.01	1.19	0.8
	10.3	12.12	31.72	1.37	1.38	0.55
	15	16.49	42.33	1.54	1.3	0.72
8%	6.3	10.3	18.53	1.04	1.16	0.8
	10.3	13.54	33.85	1.06	1.5	0.62
	15	17.3	45	1.22	1.77	0.59

The geometric standard deviation ranged from a minimum of 1.01 to a maximum of 2.12; for increasing HAB and thus residence time, there was a noticeable increase of particle size. All three concentrations exhibit a bimodal size distribution with in increasing HAB; for higher concentrations, the bimodal nature of the size distributions is more pronounced.

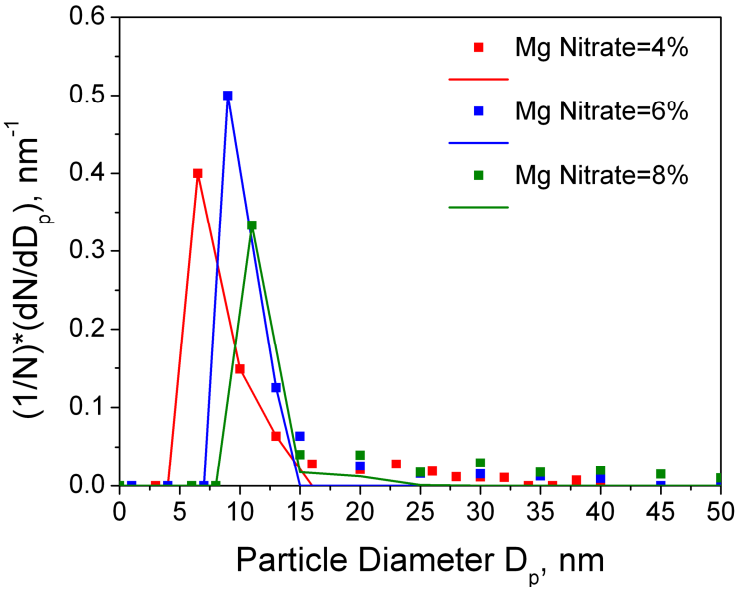

Figure 6.3. Particle size distributions at HAB=50 mm. Points are AFM experimental data, lines are best fit curves from Eq. 7.1.

Figure 6.3 shows particle size distributions obtained at HAB=50 mm, corresponding to a residence time inside the reactor of 6.3 ms, for the three concentrations. As can be seen, mostly

monodisperse particles with mean sizes of 7 nm, 9.5 nm and 11 nm are produced in these flame conditions.

Particle aspect ratio AR was calculated as the maximum height of the isolated particle divided by its base diameter. The results are shown in Figure 6.4 for 8% concentration of Mg precursors as a function of the particle equivalent spherical diameter, AR; a similar trend of the results was found for each concentration and residence time. The low aspect ratio, between 0.01 and 0.08, can be attributed to a plastic behavior of nanoparticles inside the flame, which are then subjected to a deformation when colliding to the substrate (Barone et al., 2003). Greatest particles exhibit the highest values of aspect ratio, probably due to a less plastic and more solid nature with respect to smaller particles.

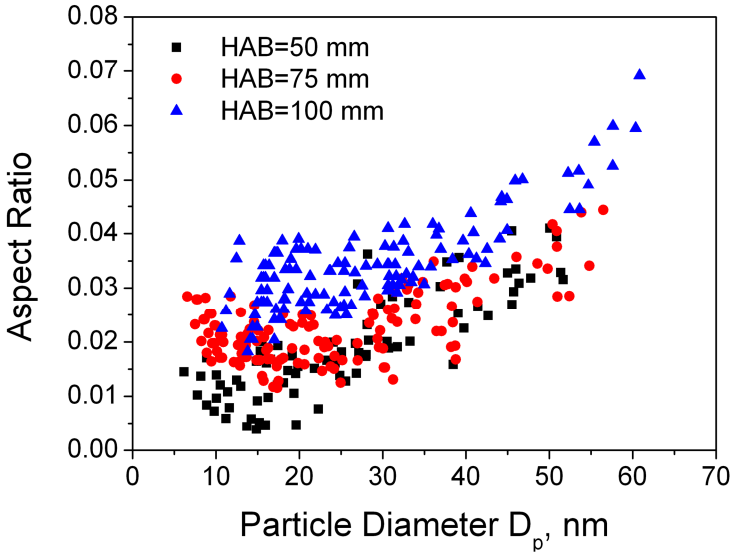

Figure 6.4. Particle aspect ratio; Mg Nitrate concentration=8%.

6.2. Titanium dioxide nanoparticles

6.2.1. Experimental set-up

The AFS system was operated using ethylene as fuel and air as oxidant, in order to generate a burned stabilized, flat, fuel-lean atmospheric premixed flame (equivalent ratio Φ =0.60, cold gas velocity=100 cm/s). A sheath flow of Argon (65 Nl/hr) was used to isolate the flame from the surrounding air. The flame was doped with precursor solutions of titanium tetraisopropoxide (TTIP, Aldrich, 97%) into ethanol (corresponding vapour flow rate 17.1 Nl/hr), at three different molar concentrations (TTIP=0.1 M, TTIP=0.3 M and TTIP=0.5 M). Resulting luminous flame height was 18 cm, corresponding to a particle residence time of 33 ms.

On-line measurements of the size distribution of the sampled particles were performed by using a differential mobility analyzer DMA (see Section 4.3.1).

For Raman analysis, flame products were collected by probe sampling method for *ex-situ* analysis on quartz filters. The sampling time was about one hour to allow the collection of enough material for the Raman analysis (0.7 mg).

For UV-Vis analysis, a colloid of as-synthesized particles in water was prepared by immersing filters in water and dispersing particles with the aid of an ultrasonic cleaning bath.

6.2.2. Particle characterization

Fig. 6.5 shows a family of particles size distribution functions (PSDs), measured online by DMA at the three different titanium tetraisopropoxide concentrations in the precursor solutions. As expected, particle size is sensitive to the amount of precursor fed to the flame reactor; particles prepared with higher TTIP concentration are larger than particles prepared with lower TTIP concentration. The average diameter is 2.2 nm for particles prepared with precursor concentration of 0.1 M, 3.7 nm for particles prepared with precursor concentration of 0.3 M and 4.1 nm for particles prepared with precursor concentration of 0.5 M.

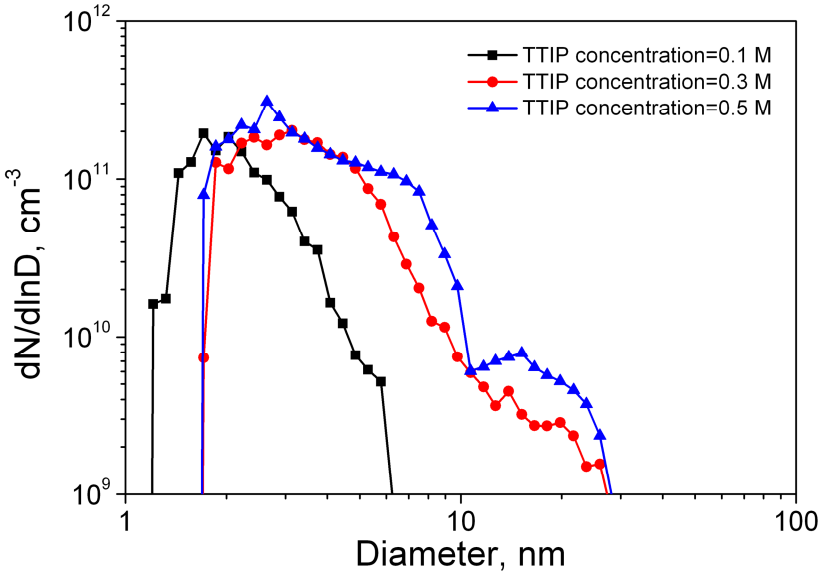

Figure 6.5. PSDs of TiO_2 nanoparticles synthesized at different precursor concentrations.

Raman analysis was performed on titania particles produced with a precursor concentration TTIP=0.3 M, and the resulting spectrum is reported in Fig. 6.6. Five Raman scattering peaks are observed, corresponding to the Raman bands assigned to the allowed modes of anatase phase TiO_2 (Balachandran and Eror, 1982): $E_g(1)$ at 143 cm^{-1}, $E_g(2)$ at 197 cm^{-1}, B_{1g} at 397 cm^{-1}, A_{1g} at 515 cm^{-}

[1] and Eg(3) at 637 cm^{-1}. No other bands were identified, showing that synthesized particles were pure anatase. This result is in agreement with thermodynamics studies conducted by Zhang and Banfield (1998), which revealed that anatase, due to its lower surface energy with respect to rutile, is the most stable phase of titania if the crystal size is less than 10 nm.

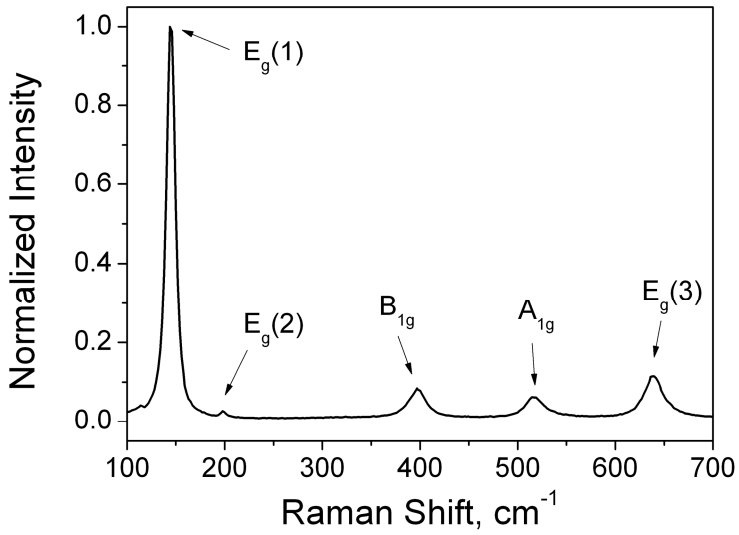

Figure 6.6. Raman spectrum of TiO_2 nanoparticles produced at TTIP=0.3 M.

Absorption spectrum of nanoparticles collected from TTIP=0.3 M flame and dispersed in ethanol, reported in left side of Fig. 6.7, shows the typical optical features of anatase nanoparticles, with a strong absorption in the UV region. For an indirect band gap semiconductor, the optical band gap can be determined from light absorption spectra by following Tauc's procedure (Tauc et al., 1966).

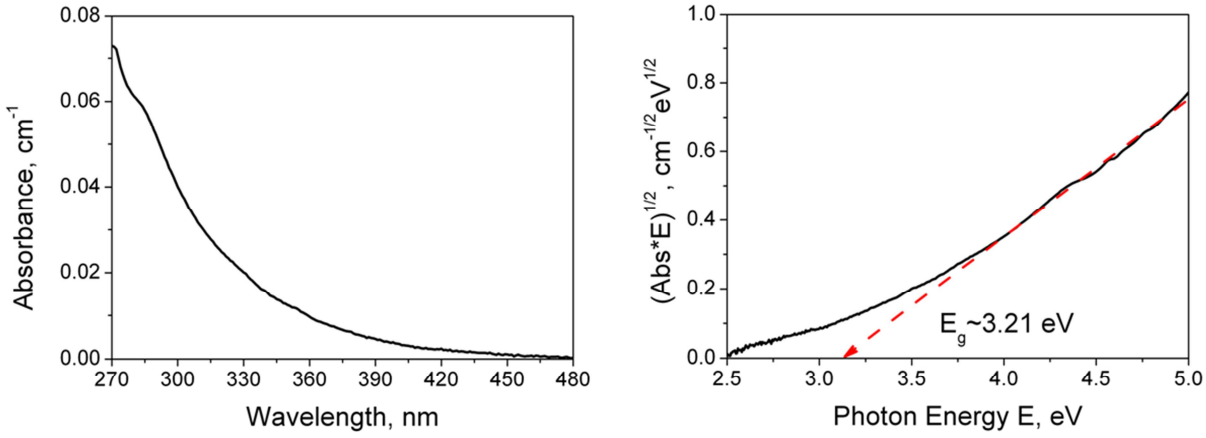

Figure 6.7. UV-Vis absorption spectrum (left side) and Tauc plot (right side) of TiO_2 nanoparticles produced at TTIP=0.3 M.

The estimated value of the optical band gap is about 3.21 eV, indicating that absorption band edge of flame-synthesized TiO_2 nanoparticles well matches the semiconductor band gap of crystalline bulk anatase (3.25 eV) (Linsebigler et al., 1995). The tail of the absorption curve in the visible spectral region can be attributed to the presence of oxygen vacancy states between the valence and the conduction bands in titania band structure (Abazovic et al., 2006).

7. Production and characterization of carbon-TiO_2 nanostructures

In this chapter, the results concerning the production via flame synthesis and the subsequent dimensional and physical-chemical characterization of pure and carbon-titania nanostructures are presented.

7.1. Carbon-TiO_2 nanoparticles for cosmetics applications

This final chapter reports the results concerning the work conducted about the synthesis and characterization of pure titania nanopowder and carbon-titania nanopowder in the aerosol flame synthesis system described in section 4.1, operated in fuel-rich conditions.

In section 2.2.1, an introduction about titanium dioxide was given, pointing out that TiO_2 nanoparticles possess unique properties in terms of structural, chemical, electronic and optical characteristics, which made TiO_2-based nanomaterials suitable for a wide range of applications, spanning from photocatalysis to food and cosmetics.

Concerning personal care products area, a widespread application is physical filter for sunscreen. Indeed, titania optical properties make it able to absorb both UVB (290–320 nm) and UVA (320–400 nm) radiations, which are mostly responsible of skin damages deriving from sun exposure (Smijs and Pavel, 2011). Also, advantages offered by sunscreens based on TiO_2 nanoparticles comprise the reduction of skin irritation and sensitization with respect to sunscreens made of organic compounds and the elimination of the natural opacity of microsized sunscreen without reducing UV blocking efficacy. It has been reported that the optimal particle/aggregate size for using titania in sunscreens is about 100-150 nm (Egerton and Tooley, 2012). The UV attenuation, i.e. the amount of UV radiation blocked by the filter, is affected by both absorption and scattering phenomena. Particles or aggregates of primary particles with dimension of about 100-150 nm give an additional scattering contribution with respect to particles with lower size, which enhance the extinction in the UVA region, offering a higher UVA protection and an effective protection in both UVA and UVB.

A fundamental requirement for using titania in sunscreens and other personal care products is photostability. Under UV illumination in aqueous media, photoactive TiO_2 can induce the formation of Reactive Oxygen Species (ROS), which are responsible of skin DNA and RNA damages (Hirakawa et al., 2004; Sayes et al., 2006). In the light of this, rutile is the preferable phase of titania when used in cosmetics applications, since it is characterized by a lower photocatalityc activity with respect to anatase phase.

Several methods have been studied to improve the stability of TiO_2 nanoparticles under UV

illumination, such as doping and coating of nanoparticles surface with inorganic and/or organic substances (Lee et al., 2007) and passivation of particle surface through thermally-assisted procedures (Serpone et al., 2005). Recently, a new method has been proposed for reducing the oxidative potential of titania. Although the doping of titanium dioxide with non-metals, and in particular carbon, is typically used as a way to obtain efficient photocatalysts exploiting solar energy, Livraghi et al. (2010) showed that the modification of TiO_2 nanoparticles with carbon induced the depression of ROS formation and so the reduction of nanopowder skin toxicity.

So, the aim of this study was to produce by flame synthesis and to characterize pure titania nanopowder and carbon-titania nanopowder for cosmetic applications, in order to investigate the possible reduced health effects in terms of ROS production given by the addition of carbon to titania nanopowder.

7.1.1. Experimental set-up

The aerosol flame synthesis system described in section 4.1 was operated using ethylene as fuel and air as oxidant, in order to generate a burned stabilized, flat, atmospheric premixed flame. The precursor solution was a 0.3 M solution of titanium tetraisopropoxide (TTIP, Aldrich, 97%) into ethanol. A sheath flow of Argon (65 Nl/hr) was used to isolate the flame from the surrounding air. Two different experimental flame conditions were investigated, as reported in Table 7.1, with very similar parameters and very similar residence times, by only varying the total flow rate of air, and so the global equivalent ratio Φ, and so the amount of carbon available in the system.

Table 7.1. Investigated flame reactor parameters

	Flame A	*Flame B*
Ethylene, Nl/hr	10	10
Air, Nl/hr	220	190
Ethanol, Nl/hr	17.5	17.5
Equivalence ratio Φ	1.52	1.73
Cold gas velocity (cm/s)	27	24

For XRD, SEM and Raman analysis, particles were collected by thermophoresis on the chilled stainless steel plate, placed at 10 cm above the burner's surface.

AFM measurements were performed at room temperature and 30% relative humidity, operating the instrument in semi-contact height mode and in phase mode in air using NANOSENSORS™ SSS-NCHR super-sharp silicon probes with nominal tip radius of 2 nm, over selected areas of 8 μm × 8 μm (1024 × 1024 pixel resolution). Height images and phase images were acquired simultaneously. Particles were collected by means of the thermophoretic pneumatic actuator.

On-line measurements of the size distribution of the sampled particles were performed by using electrical low pressure impactor (see Section 4.3.2 and Section 4.3.7).

For optical analysis, nanoparticles were collected on quartz substrates, and UV-visible spectra were measured in the wavelength range 200–700 nm.

ROS detection was performed on human keratinocytes cells (HaCaT), grown in Dulbecco's modified Eagle's medium (DMEM) medium with 1% L-glutamine (Lonza), 1% penicillin/streptomcyin (Lonza), and 10% foetal calf serum (Gibco). For control wells (untreated cells), a corresponding amount of compound buffer was added. To induce ROS, the cell plate was incubated in a 5% CO_2, 310 K atmosphere for one hour. Fluorescence intensity, proportional to the amount of ROS present, was measured at λ_{ex}=520 nm/ λ_{em}=605 nm with a Tecan Infinite 200 PRO Microplate Reader.

Characterization of flame temperature was carried out using an R-type thermocouple (Pt/13%Rh vs. Pt), substituting TTIP solutions with pure ethanol to prevent nanoparticles deposition on thermocouple junction. Flame temperature was measured every 5 millimeters above the burner from 7.5 cm (Flame A) and from 5 cm (Flame B) up to 9.8 cm; just below the sampling plate. Below 7.5 cm for Flame a and 5 cm for Flame B, temperature reached a value higher than 2000 K, which is above the maximum operating level of the thermocouple. Temperature measurements are corrected for radiation losses (McEnally et al., 1997). The profiles are reported in Fig. 7.1.

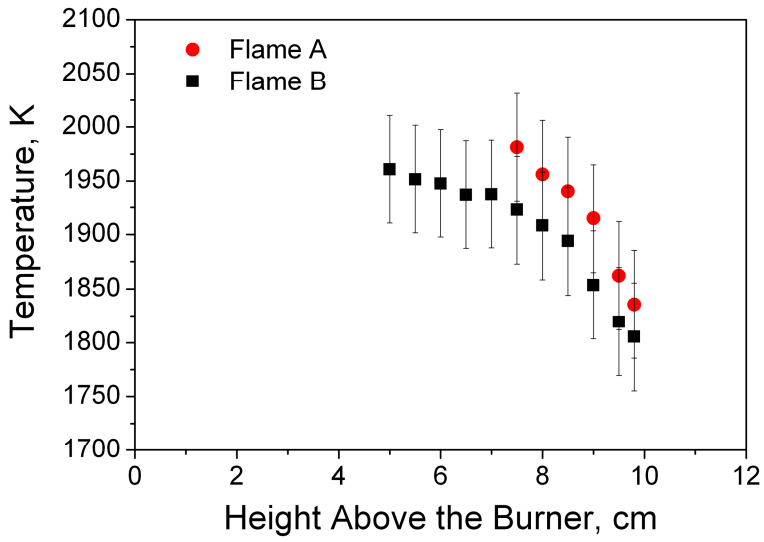

Figure 7.1. Temperature profiles measured for the studied flames. Error bars report the uncertainty in the temperature of ± 50 K.

7.1.2. Particle characterization

XRD is a well-established technique to determine the phase of TiO_2 particles. The XRD spectra measured for powders produced in the two different flame conditions are reported in Fig. 7.2. It can be observed that synthesized powders have both rutile and anatase phases, rutile being the predominant phase. The weight fraction of the rutile phase, W_R, has been calculated from the following equation (Spurr and Myers, 1957):

$$W_R = \frac{1}{1 + 0.8 * I_A / I_R} \tag{7.1}$$

Where I_A is the relative intensity of the peak corresponding to 101 reflection for anatase at $2\theta=25.4°$ and I_R is the relative intensity of the peak corresponding to 110 reflection for rutile at $2\theta=27.5°$.

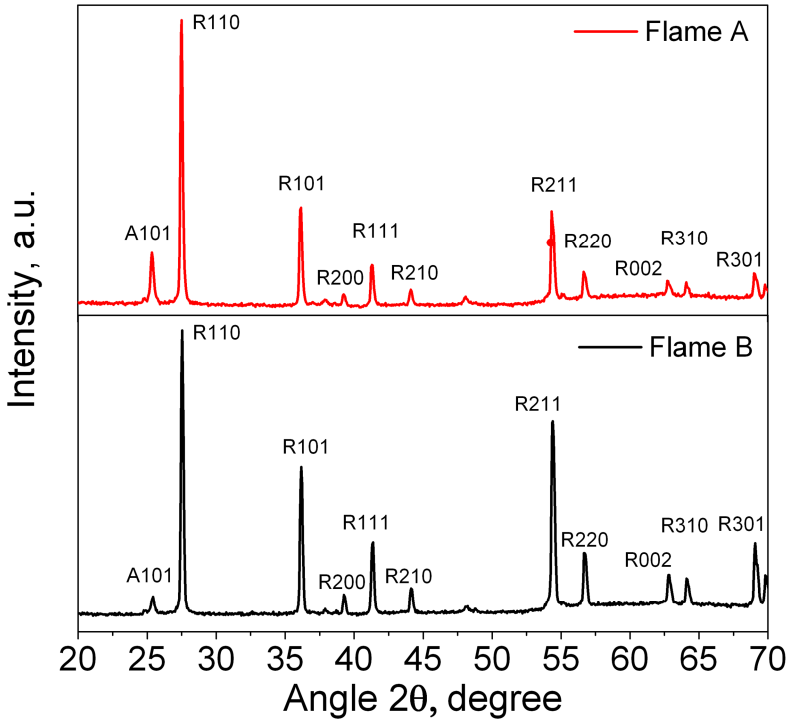

Figure 7.2. XRD patterns of titania powder produced from Flame A (red curve) and Flame B (black curve).

The weight percentage of rutile is equal to 85% for nanoparticles coming from Flame A and 91% for nanoparticles coming from Flame B. Those findings are in agreement with the results of Memarzadeh et al. (2011), which showed that fuel-rich conditions favor the formation of rutile phase, while anatase-phase TiO_2 particles typically grow in highly oxygen-rich environments (Kho

et al., 2011). The average crystal dimensions have been estimated from XRD analysis by the Scherrer equation (Cullity, 1978) to be 34 nm (rutile phase) and 30 nm (anatase phase) for particles produced in Flame A conditions and 31 nm (rutile phase) and 27 nm (anatase phase) for particles produced in Flame B conditions.

Figure 7.3 shows Raman spectra in the visible region of synthesized nanopowders. In both samples, the peaks corresponding to the two E_g modes (235 cm^{-1} and 447 cm^{-1}) and to the A_{1g} mode (612 cm^{-1}) of rutile, and to the E_g mode of anatase (143 cm^{-1}) are present (Oshaka et al., 1978). In addition, the sample coming from Flame B shows the presence of two additional peaks: the G-peak (1580 cm^{-1}), which has been observed in graphitic type structures, and the D-peak (1360 cm^{-1}), which occurs due to defects in graphitic structures. Those peaks show that carbon growth occurs together with titania nanoparticles synthesis when particles are produce in Flame B conditions.

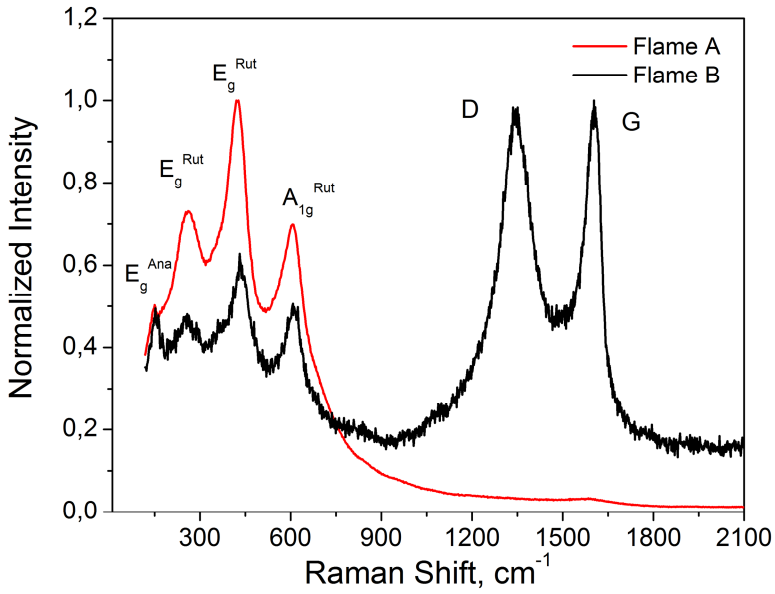

Figure 7.3. Raman spectra of titania powder produced from Flame A (red curve) and Flame B (black curve).

Dimensional characterization was performed by means of AFM on isolated particles collected by thermophoresys with a single insertion. AFM images were acquired over an area of 8 µm x 8 µm and then analyzed to obtain volume, base area and maximum height of the particles. Particle volume was evaluated from the base diameter and height considering a conical shape, and the distribution of the diameter D_p of spheres with equal volume was finally determined. The particle size distributions (PSDs) were then fitted by a lognormal distribution functions, shown in Equation 7.2.

$$\frac{1}{N}\frac{dN}{dlnD_p} = \frac{1}{\sqrt{2\pi}\ln(\sigma)}\exp\left(-\frac{\ln(D_p / < D_p >)}{2\ln(\sigma)}\right)^2 \qquad (7.2)$$

Where D_p is the particle diameter, $<D_p>$ is the mean particle diameter, N is the number density of the particles and σ is the geometric standard deviation.

Figure 7.4 reports the particle equivalent diameter distributions obtained from AFM for the two flame conditions, together with their best fit from Equation 7.2.

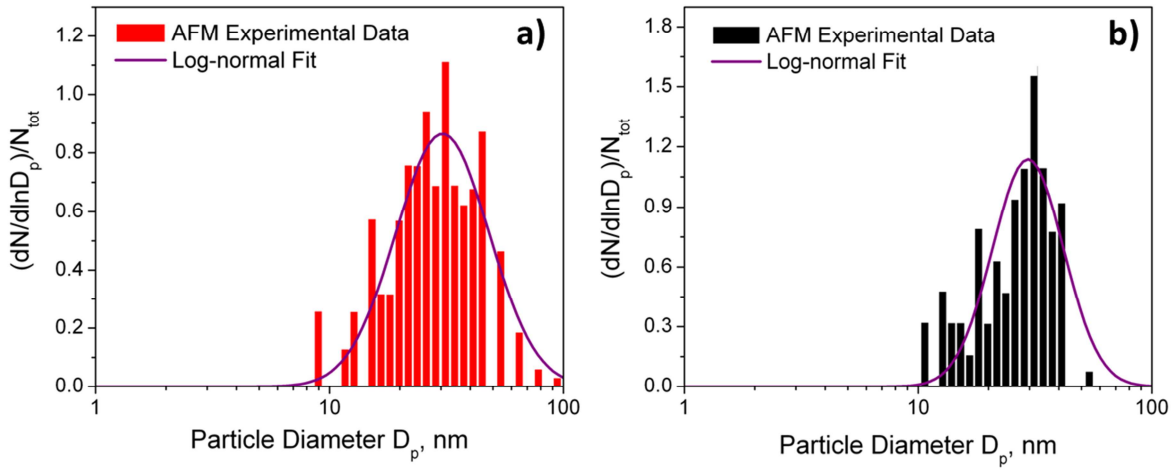

Figure 7.4. Particle size distributions from AFM of pure-titania powder from Flame A (a, red bars) and carbon-titania powder from Flame B (b, black bars), and best log-normal fit curves from Eq. 7.2 (purple lines).

Mean particle diameters were calculated to be 30.5 nm for Flame A and 29 nm for Flame B, in good agreement with average crystal dimensions obtained from XRD data.

Since particle with sizes of 100 nm or more could be difficult to detect and to properly quantify together with particle with lower sizes, when using AFM and thermophoretic sampling, an additional dimensional analysis was performed. Flame synthesized nanoparticles were collected by a suction probe and the aerosol analyzed on line by ELPI, which is characterized by an higher range of diameters extended to 1000 nm, for measuring the size distribution of the solid compounds suspended in the gas. The comparison of the two particle size distribution functions is reported in Fig. 7.5, showing a good agreement between AFM PSD and ELPI PSD.

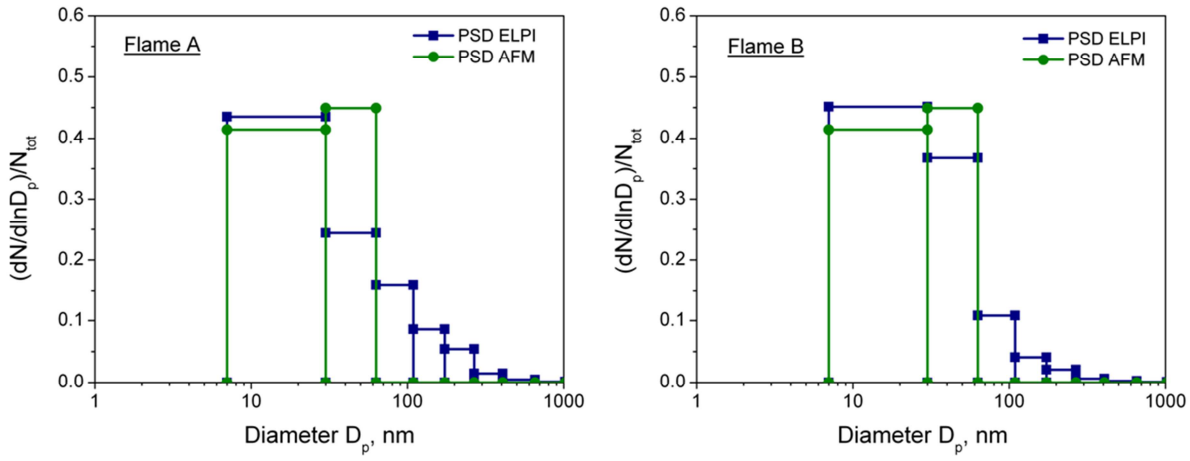

Figure 7.5. Particle size distributions obtained from ELPI (blue curve) and AFM measurements (green curve) of pure-titania powder from Flame A (left side) and carbon-titania powder from Flame B (right side).

Properties of synthesized particles were also investigated using phase mode imaging. AFM phase mode images of pure-titania and carbon-titania nanoparticles from Flame A and from Flame B are shown in Fig. 7.6. Changes in the phase of cantilever oscillation, caused by changes in the investigated material properties (viscoelasticity, hardness and stickiness), result in a relative phase lag map, in which dark areas correspond to a negative phase lag, while bright areas correspond to a positive phase lag.

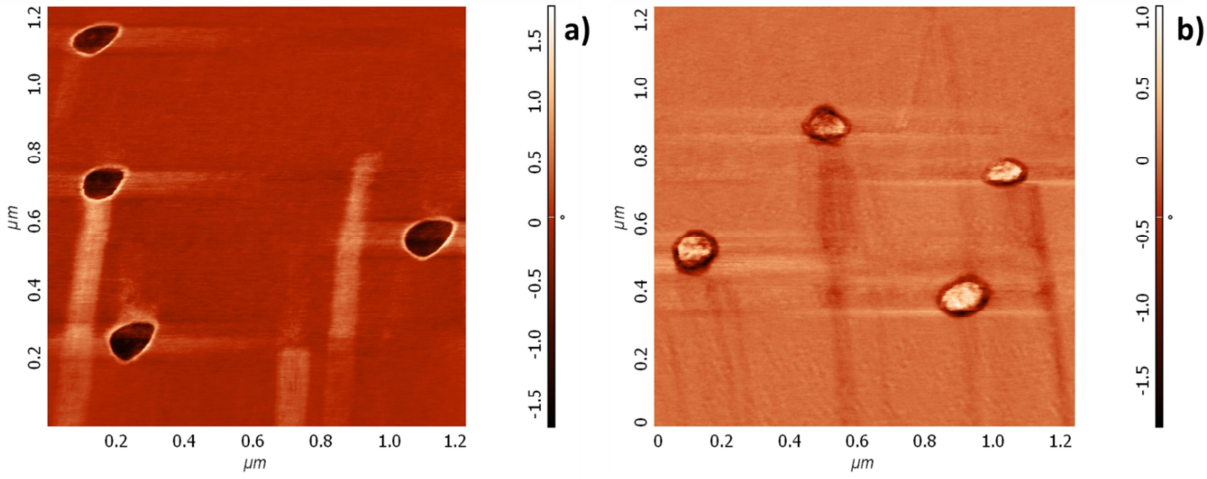

Figure 7.6. AFM phase mode images of pure-titania nanoparticles from Flame A (a) and carbon-titania nanoparticles from Flame B (b).

The images show that nanoparticles from Flame A are characterized by a negative phase lag, surrounded by a bright edge area, while nanoparticles from Flame B are characterized by a positive phase lag, surrounded by a dark edge area. Unfortunately, it is not possible to obtain quantita-

tive information from phase images, but they are a clear evidence of differences in surface properties between pure-titania and carbon-titania nanoparticles.

Particle morphology was investigated from SEM images, reported in Fig. 7.7, of pure-titania and carbon-titania powders synthesized from Flame A (a) and from Flame B (b). Spherical particles of diameters in the range 30-50 nm can be clearly seen, together with aggregates of primary particles with dimension of 100-200 nm. A similar degree of aggregation between the two nanopowders can be observed.

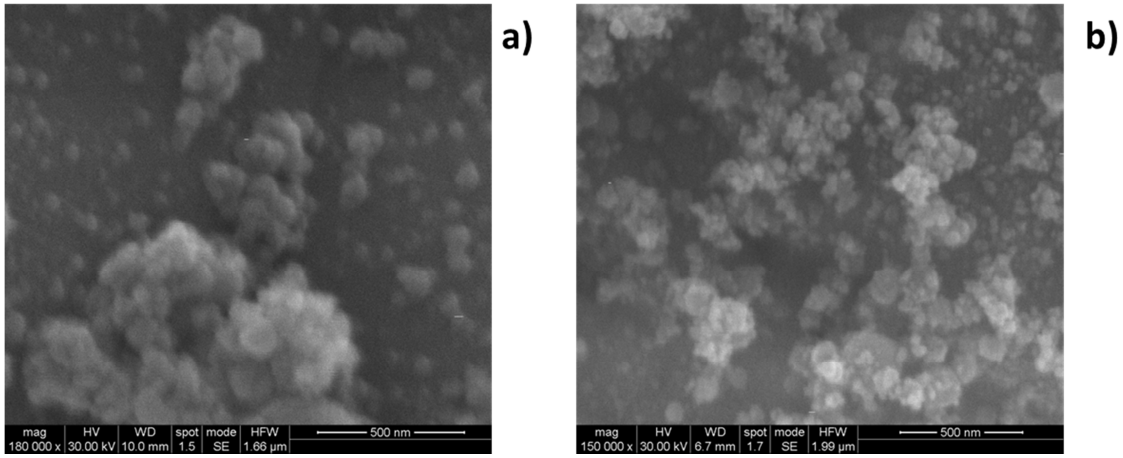

Figure 7.7. Scanning electron microscopy images of pure-titania powder from Flame A (a) and carbon-titania powder from Flame B (b).

UV-Vis absorption spectra of the two nanopowders are reported in Fig. 7.8. Both nanopowders show a high absorption efficiency in the UVA and in the UVB regions, while absorption in the visible region at λ>400 nm is significantly increased for carbon-titania nanopowder.

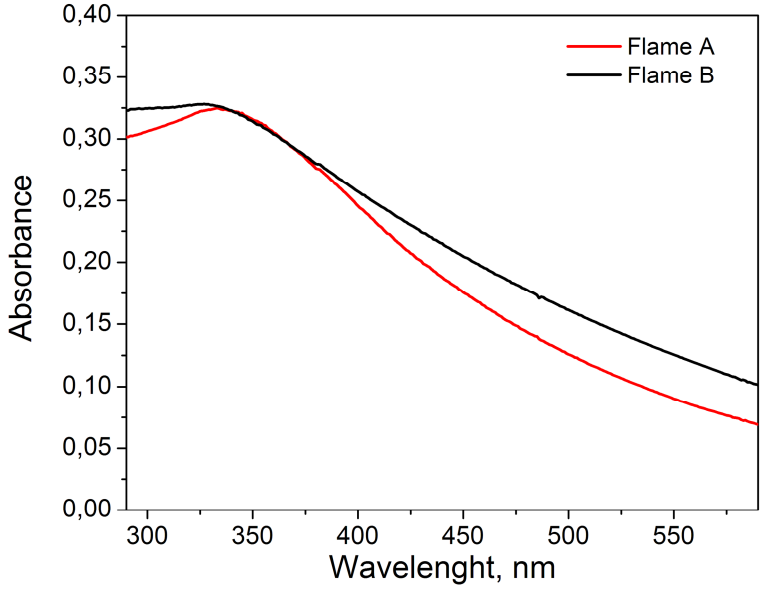

Figure 7.8. UV-Vis absorption spectra of pure-titania powder from Flame A and carbon-titania powder from Flame B.

7.1.3. Detection of ROS production

The analysis of Reactive Oxygen Species production was performed on HaCaT cells (human keratinocytes), grown in DMEM medium with 1% L-glutamine (Lonza), 1% penicillin/streptomcyin (Lonza) and 10% foetal calf serum (Gibco) at 37°C in humidified atmosphere containing 5% CO_2. The HaCaT cells were exposed to a concentration of 5 µg/ml of three different TiO_2 powders: pure TiO_2 powder produced in Flame A, carbon- TiO_2 powder produced in Flame B, and commercial titania nanopowder (Sigma Aldrich, <100 nm particle size). The stock solutions of TiO_2 nanopowders were prepared in deionized water, dispersed for 10 min by using a sonicator to prevent aggregation and vortexed for 1 min. Solutions were then kept at 4 °C and used within 1 week for the experiments. Prior to each experiment, the stock solution was sonicated on ice for 10 min, vortexed for 1 min and then immediately diluted into the working concentrations with medium. For control wells (untreated cells), a corresponding amount of compound buffer was added. To induce ROS, the cell plate was incubated in a 5% CO_2, 37 °C incubator for one hour. Fluorescence intensity was measured at λ_{ex}=520 nm / λ_{em}=605 nm with a Tecan Infinite 200 PRO Microplate Reader. All experiments were performed in triplicate and repeated at least 3 times.

Figure 7.9 reports the fluorescence intensity signals measured after one-hour treatment, which is proportional to the amount of generated ROS. It is possible to observe that flame-synthesized titania produces a lower amount of ROS with respect to commercial TiO_2. Also, the

presence of carbon induces a positive effect, which results in further reduction of the ROS produced by the cells.

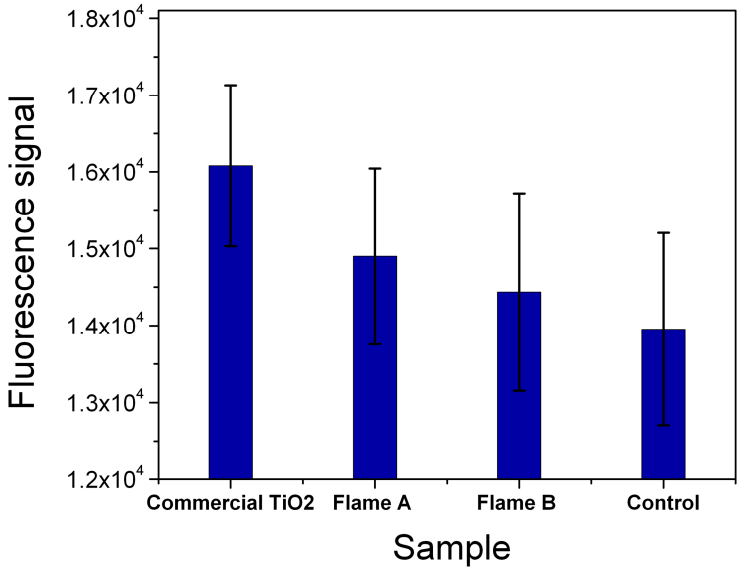

Figure 7.9. Intracellular ROS generation after treatment of HaCaT cells with commercial TiO_2 nanopowder, Flame A pure-TiO_2 nanopowder and Flame B carbon-TiO_2 nanopowder.

8. Conclusions

This thesis work has been focused on the flame synthesis of organic, inorganic and metal-organic nanoparticles. The production of carbon-based nanomaterials, TiO_2 nanoparticles and carbon-TiO_2 nanocomposites has been conducted.

The flame reactors used for the synthesis of carbon nanomaterials were constituted by un-doped flat laminar ethylene/air premixed flame, operated in fuel-rich condition, in which vapor carbon precursors are given by the unburned fuel. Different carbonaceous particles were produced by changing flame equivalent ratio and particle residence time (i.e, sampling position).

Operating the reactor in intermediate conditions (Φ=1.83) between near-stoichiometric fuel rich flames and sooting flames allowed to produce a new carbon nanostructure, composed by two-dimensional carbon nano-disks with atomic thickness, and in-plane lateral dimension of the order of tens of nanometers. The carbon nano-disks contain small aromatic islands with in-plane size L_a of about 1.2 nm. The quantum confinement in the aromatic islands and the small size of the disks make edges effects as a predominant source of disorder. However, other kind of disorder are also present, including chain-like bridges or dangling bonds or lattice distortion possibly caused by penta-rings or sp^3 inclusions.

When the reactor was operated in different sooting flame conditions (from slightly to fully sooting, $2.18<\Phi<2.58$), flame-formed carbon nanoparticles FFCNPs with different dimension and properties were synthesized. The characterization we conducted on FFCNPs has demonstrated that they can exhibit different electrical and optical properties, which are strongly related to their nanostructure, depending on the flame synthesis conditions. The variability of the electrical properties of those particles is of relevance for the development and the calibration of conductometric particle sensors. Simply conductometric sensors cannot be used for the correct determination of particulate matter emitted from different combustion sources because different types of particles can be emitted according to combustion technology, the fuel characteristics and the operating conditions. Moreover, our results can be useful for the development of conductometric sensors to be used in combustion exhausts where soot particles are not the only formed particles but also a relevant presence of nanoparticles of organic nature might be present. Further investigation needs to be performed in future works to explore the possibility to use the results here obtained for the development of a conductometric sensor for bluish flames and to develop calibrated conductometric sensors able to selectively detect different classes of FFCNPs at the combustion exhausts.

Finally, we performed a characterization of morphological and surface properties of a wide range combustion generated nanoparticles, which includes both carbon nanostructures synthesized in non-sooting fuel-rich conditions and carbon nanostructures synthesized in sooting fuel-rich conditions. Morphological and surface properties analyses were conducted by means of AFM, employing AFM force-spectroscopy technique for the first time to follow the graphitization trajectories of carbon nanoparticles in fuel-rich flames. The analysis of AFM topographic measurements, performed in semi-contact mode, has shown that particles formed in the flames with equivalence ratios less than 2 have a monomodal size distribution with the mean particle size moving from 3.7 to 5 nm as the equivalence ratio increases. The size distribution of particles sampled in richer flames are clearly bimodal with the first mode centered at about 2.5 nm and the second one which moves from 10 to 50 nm as flame richness increases. The height of particles deposited on mica plates is always much lower than particle base diameter, in whichever flame condition the particles were collected, showing that the shape of the particles collected on a sampling plate is never spherical. Moreover, increasing the flame richness, particle shape moves from an almost atomically thick disk-like object, with height of about 0.40 nm, to thicker compounds which may be characteristic of 2-3 stacked molecular layers. Those results are in agreement with the observation of the formation of aromatic plane stacks in coagulated primary particles obtained recently by using off-line cyclic voltammetry, Raman spectroscopy, and light absorption (Commodo et al., 2014). Soot particles produced in very fuel-rich flames exhibit adhesive and attractive forces lower, but comparable, to that of highly ordered pyrolytic graphite. Whereas, carbon nanoparticles formed below the soot limit appearance have values of attractive and adhesive forces much lower than those of the soot particles and more similar to those characteristic of aromatic molecules. From force vs. distance measurements we have determined the Hamaker constant of the particles in each flame. The trend of the Hamaker constant with flame equivalent ratio, compared to values of benzene and HOPG, confirm a continuous increase of particle aromaticity and three-dimensional internal ordering by increasing the flame equivalent ratios.

Regarding the production of metal oxides nanoparticles and carbon-metal oxides nanocomposites, an Aerosol Flame Synthesis (AFS) system was developed and successfully operated in VAFS mode to produce pure nanoparticles of magnesium oxide and titanium dioxide

MgO nanoparticles have been characterized by SEM, EDXS and AFM for elemental composition and particle morphology and size analysis. It has been found that both residence time and precursor concentration influence the size of formed nanoparticles. Specifically, at a residence time of 6.3 ms, almost monodisperse particles can be obtained with mean sizes ranging between 7 and 11

nm by varying the precursor concentration in the solution droplets.

TiO_2 nanoparticles have been characterized by Raman spectroscopy, UV-Vis absorption and DMA for phase composition, optical properties and particle size analysis. Pure anatase phase nanoparticles with a high degree of monodispersion and a very low dimension, ranging from 2.2 nm to 4.1 nm, and an optical band gap of 3.21 eV have been obtained by varying the precursor TTIP amount fed to the synthesis system.

Finally, the AFS system was operated in fuel-rich flame reactor conditions, in order to synthesize pure TiO_2 and carbon-TiO_2 nanoparticles with similar dimension and compositions. As expected, fuel-rich conditions favored the formation of anatase-rutile mixture in both nanopowders, with rutile being the predominant phase, which is the preferable phase for cosmetic application due to its lower photoactivity. The presence of carbon in the synthesized carbon-TiO_2 powder was confirmed by Raman spectroscopy.

Particle size and morphology, aggregation degree and aggregates dimension were derived from AFM, ELPI and SEM measurements. Both nanopowders showed to possess the optimal aggregates size for application as sunscreen physical filters. This finding was confirmed also by UV-Vis spectra, which showed that both nanopowders give a scattering contribution which enhances the protection in the UVA region.

ROS analysis showed that flame-synthesized titania produces a lower amount of ROS with respect to commercial TiO_2. The presence of carbon induces a further decrease of ROS production in human keratinocytes cells, leading to a reduction of nanopowder skin toxicity.

Further works will be performed to quantify the amount of carbon and to characterize how carbon and titania are structured in carbon-TiO_2 powders. Also, the mechanism of depression of ROS formation by carbon-TiO_2 nanopowders will be deeply investigated.

9. References

Abazović, N.D., Comor, M.I.,Dramićanin, M.D.,Jovanović, D.J.,Ahrenkiel, S.P.,Nedeljković, J.M., 2006. *J. Phys. Chem. B* **110**: 25366-25370.

Abid, A.D., Heinz, N., Tolmachoff, E.D., Phares, D.J., Campbell, C.S., Wang, H., 2008. *Comb. Flame* **154**: 775-788.

Adkins, C.J., 1982. *J. Phys. C* **15**: 7143-7155.

Arabi-Katbi, O.I., Wegner, K., Pratsinis, S.E., 2002.*Ann. Chim. Sci*. *Mat.* **27**: 37-46.

Athanassiou, E. K., Grass, R. N., Stark, W. J., 2006. *Nanotechnology* **17**: 1668-1673.

Balachandran, U., Eror, N.G., 1982. *J. Sol. State Chem.* **42** (3): 276–282.

Balberg, I., Wagner, N., Goldstein, Y., Weisz, S.Z., 1990. *Mater. Res. Soc. Symp. Proc.* **195**: 233–238.

Barone, A.C., D'Alessio, A., D'Anna, A., 2003. *Combust. Flame* **132** (1–2): 181-187.

Basile, G., Rolando, A., D'Alessio, A., D'Anna, A., Minutolo, P., 2002. *Proc. Comb. Inst.* **29** (2): 2391-2397.

Bhanwala, A.K., Kumar, A., Mishra, D., Kumar, J., 2009. *J. Aerosol Sci.* **40** (8): 720–730.

Bockhorn, H., 1994. *Soot Formation in Combustion: Mechanisms and Models*, Springer Verlag, Berlin.

Bruschi, P., Nannini, A., 1991. *Thin solid films* **201**: 29-38.

Burnham, N. A., Dominguez, D. D., Mowery, R. L., and Colton, R. J., 1990. *Phys. Rev. Lett.* **64** (16): 1931-1934

Butt, H.J., Cappella, B., Kappl, M., 2005. *Surf. Sci. Rep.* **59**: 1-152.

Camenzind, A., Caseri, W. R., Pratsinis, S. E., 2010. *Nano Today* **5**: 48-65.

Cançado, L.G., Takai, K., Enoki, T., Endo, M., Kim, Y.A., Mizusaki, H., et al., 2008. *Carbon* **46**: 272–275.

Cançado, L.G., Jorio, A., Martins Ferreira, E.H., Stavale, F., Achete, C.A., Capaz, R.B. et al., 2011. *Nano Lett.* **11**: 3190–3196.

Carbone, F., 2010. *Physicochemical characterization of combustion generated inorganic nanoparticles,* Ph.D. Thesis, Fridericiana Editrice Universitaria, Napoli.

Carbone, F., Beretta, F., D'Anna, A., 2011. *Fuel* **90**: 369-375.

Cecere, D., Sgro, L.A., Basile, G., D'Alessio, A., D'Anna, A., Minutolo, P., 2010.*Comb. Sci. Technol.* **174** (11-12): 377-398.

Chiarello, G. L., Rossetti, I., Forni, L., 2005. *J. Catal.* **236**: 251–261.

Choi, H.C., Jung, Y.M., Kim, S.B., 2005. *Vib. Spectrosc.* **37**: 33-38.

Chung, D.D.L., 2004. *J. Mater. Sci.* **39**: 2645-2461.

Choudhury, B., Borahm, B., Choudhury, A., 2013. *Mat. Sci. Eng. B* **178**: 239-247.

Commodo, M., Violi, S., D'Anna, A., D'Alessio, A., Allouis, C., Beretta, F., Minutolo, P., 2007. *Comb. Sci. Technol.* **179** (1-2): 387-400.

Commodo, M., Sgro, L.A., Minutolo, P., D'Anna, A., 2013. *J. Phys. Chem. A* **117** (19): 3980–3989.

Commodo, M., Tessitore, G., De Falco, G., Bruno, A., Minutolo, P., D'Anna, A., 2014. *Proc. Combust. Inst.* **35** (2): 1795-1802.

Cullity, B.D., 1978. *Elements of X-ray diffraction* (2nd ed.), Addison Wesley, Reading.

Dalzell, W.H., Sarofim, A.F., 1969. *J. Heat Transfer* **91**: 100-104.

D'Alessio, A., Barone, A.C., Cau, R., D'Anna, A., Minutolo, P., 2005. *Proc. Combust. Inst.* **30** (2): 2595–2603.

D'Alessio, A., D'Anna, A., Minutolo, P., Sgro, L.A., 2009. in *Combustion Generated Fine Carbonaceous Particle*, KIT Scientific Publication, Karlsruhe.

D'Anna, A., 2009a. *Proc. Combust. Inst.* **32**: 593-613.

D'Anna, A., 2009b. "Particle inception and growth: experimental evidences and a modelling attempt", in *Combustion Generated Fine Carbonaceous Particle*, KIT Scientific Publication, Karlsruhe.

De Filippo. A., Sgro, L.A., Lanzuolo, G., D'Alessio, A., 2009. *Combust. Flame* **156** (9): 1744-1754.

De Wolf, P., Brazel, E., Erickson, A., 2001. *Mat. Sci. Semicond. Proc.* **4**: 71-76.

Di, D.R., He, Z.Z., Sun, Z.Q., Liu, J., 2012. *Nanomed. Nanotech. Biol. Med.* **8**: 1233-1241.

Dobbins, R.A., 2007. *Aerosol Sci. Technol.* **41** (5): 485-496.

Dobbins, R.A., Megaridis, C.M., 1987. *Langmuir* **3:** 254-259.

Echavarria, C. A., Sarofim, A. F., Lighty, J. S., and D'Anna, A., 2009. *Proc. Combust. Inst.* **32**: 705-711.

Egerton, T.A., Tooley, I.R., 2012. *Int. J. Cosmet. Sci.* **34** (2): 117-122.

Eichenlaub, S., Chan, C., and Beaudoin, S. P., 2002. *J. Colloid Interface Sci.* **248**: 389–397.

Fernandez De La Mora, J.J., De Juan, L.L., Liedte, K., Schmidt-Ott, A., 2003. *J. Aerosol Sci.* **34**: 79-98.

Ferrari, A.C., Robertson, J., 2000*. Phys. Rev. B* **61**: 14095-14107.

Ferrari, A.C., Robertson, J., 2001*. Phys. Rev. B* **64**: 075414–075426.

Ferrari, A.C., 2007. *Solid State Commun.***143**: 47–57.

Ferrari, A.C., Meyer, J.C., Scardaci, V., Casiraghi, C., Lazzeri, M., et al., 2006*. Phys. Rev. Lett.* **97**: 187401.

Ferrari, A.C., Basko, D.M., 2013. *Nature Nanotech.* **8**: 235-246.

Formenti, M., Juiliet, F., Meriaudeau ,P., Teichner, S.J., Vergnon, P., 1972. *J. Colloid Interface Sci.* **39**: 79–89.

Francis, R. A., Mahmud, K., Belmont, J. A., Wang, M.J., 1996. Patent No. W09637547.

Friedbacher, G.,Grasserbauer, M., 1995. *J. Anal. Chem.* **67** (10): 1749-1754.

Fujishima, A., Rao, T.N.,Tryk, D.A., 2000. *Journ. Photochem. Photobiol. C* **1**: 1-21.

Gady, B., Schleef, D., Reifenberger, R., Rimai, D., DeMejo, L. P., 1996. *Phys. Rev. B.* **53** (12): 8065.

Ganguly, A., Trinh, P., Ramanujachary, K.V., Ahmad, T., Mugweru, A. ., 2011. *J. Colloid Interface Sci.* **353**: 137-142.

Grob, B., Schmid, J., Ivleva, N.P., Niessner, R., 2012.*Anal. Chem* .**84**: 3586-3592.

Hagen, G., Feistkorn, C., Wiegärtner, S., Heinrich, A., Brüggemann, D., Moos, R., 2010. *Sensors* **10** (3): 1589-1598.

Hamaker, H. C., 1937. *Physica* **4** (10): 1058-1072.

Hashemi, N., Paul, M. R., Dankowicz, H., Lee, M., Jhe, W., 2008. *J. Appl. Phys.* **104**: 063518.

Haynes, B.S., Wagner, H.Gg, 1981. *Prog. Energy Combust. Sci.* **7** (4): 229-273.

Hinds, W. C., 1999. *Aerosol technology: properties, behavior and measurements of airborne particles,* Wiley-Interscience, New York.

Hirakawa, K., Mori, M., Yoshida, M., Oikawa, S., Kawanishi, S., 2004. *Free Radical Res.* **38**: 439-447.

Howard, J. B., 1990. *Proc. Combust. Inst.* **23**: 1107-1127.

Hung, C.H., Katz, L. J., 1992. *J. Mater. Res.* **7**: 1861–1869

Hyeon, T., Lee, S.S., Park, J., Chung, Y. Bin Na, H., 2001. *J. Am. Chem. Soc.* **123**: 12798-12801.

Iijima, S., 1991. *Nature* **354**: 56-58.

Israelachvili, J. N., 2011. *Intermolecular and Surface Forces* (3rd ed.), Academic Press, London.

Jalili, N., Laxminarayana, K., 2004. *Mechatronics* **14** (8): 907–945.

Jander, H., Wagner, H. Gg. (Eds.), 1990. *Soot Formation in Combustion: an International Round Table Discussion.* Vandenhoeck and Ruprecht, Gottingen.

Jang, Y. J., Simer, C., Ohm, T., 2006. *Mater. Res. Bull.* **41**: 67–77.

Jorio, A., Lucchese, M.M., Stavale, F., Ferreira, E.H., Muotinho, M.V.O., Capaz, R.B., Achete, C.A., 2010. *J. Phys. Condens. Matter.* **22**: 334204.

Kamat, P.V., 2012. *J. Phys. Chem. C* **116**: 11849−11851.

Kammler, H.K., Mueller, R., Senn, O., Pratsinis, S.E., 2003. *AIChE J.* **47** (11): 1533-1543.

Kammler, H.K., Pratsinis, S.E., 2003. *J. Mater. Res.* **18** (11): 2670-2676.

Kasper, M., Siegmann,K., Sattler, K., 1997. *J. Aerosol Sci*. **28**: 1569-1578.

Keskinen, J., Pietarinen, K., Lehtimäki, M., 1992. *J. Aerosol Sci*. **23** (4): 353-360.

Khan, S.U.M., Al-Shahry, M., Ingler Jr., W.B., 2002. *Science* **297** (5590): 2243–2245.

Kho, Y.K., Teoh, W.Y., Mädler, L., Amal, R., 2011. *Chem. Eng. Sci.* **66** (11): 2409–2416.

Kodas, T.T., Hampden-Smith, M., 1999. *Aerosol Processing of Materials*, Wiley-VCH, New York.

Koc, R., Cattamanchi, S.V. *J. Mater. Sci.* **33**: 2537-2549.

Koch, W., Friedlander, S., 1990. *J. Colloid Interface Sci.* **140** (2): 419-427.

Kroto, H. W., Heath, J. R., O'Brien, S. C., Curl, R. F., Smalley, E., 1985. *Nature* **318**: 162-163.

Lakowicz, J.R., 2006. *Principles of Fluorescence Spectroscopy* (3rd Edition), Springer, New York.

Lee, S. I., Howell, S. W., Raman, A., Reifenberger, R., 2002. *Phys. Rev. B* **66**: 115409.

Lee, W.A., Pernodet, N., Li, B., Lin, C. H., Hatchwell, E., Rafailovich, M.H., 2007. *Chem. Commun.* **45:** 4815–4817

Lespade, P., Marchand, A., Couzi, M., Cruege, F., 1984. *Carbon* **22**: 375–85.

Li, C., Hu, Y., Yuan, W., 2010. *Particuology* **8**: 556–562.

Linsebigler, A.L., Lu, G.Q., Yates, J.T., 1995. *Chem. Rev.* **95**: 735-758.

Livraghi, S., Corazzari, I., Paganini, M.C., Ceccone, G., Giamello, E., Fubini, B., Fenoglio, I., 2010. *Chem. Commun.* **46** (44): 8478-8480.

Lomboy, G., Sundararajan, S., Wang, K., and Subramaniam, S., 2001. *Cem. Concr. Res.* **41**: 1157-1166.

Lucchese, M.M., Stavale, F., Martins Ferreira, E.H., Vilani, C., Moutinho, M.V.O., Capaz, R.B. et al., 2010. *Carbon* **48**: 1592–1597.

Madler, L., Krumeich, F., Burtscher, P., Moszner, N., 2006.*J. Nanopart. Res.* **8**: 323-333.

Mädler, L., Stark, W. J., Pratsinis, S. E., 2002. *J. Mater. Res.* **17**: 1356–1362.

Mafra, D.L., Samsonidze, G., Malard, L.M., Elias, D.C., Brant, J.C., Plentz, F., et al., 2007. *Phys. Rev. B* **76**: 233407.

Makela, J.M., Rihela, M., Ukkonen, A., Jokinen, T. Keskinen, J., 1996. *J. Chem. Physics.* **105**: 1562-1571.

Malard, L.M., Pimenta, M.A., Dresselhaus, G., Dresselhaus, M.S., 2009. *Phys. Repo.* **473**: 51–87.

Maricq M.M., 2004. *Combust. Flame* **137**: 340-350.

Maricq M.M., 2005. *Combust. Flame* **141**: 406-416.

Martins Ferreira, E.H., Moutinho, M.V.O., Stavale, F., Lucchese, M.M., Capaz, R.B., Achete, C.A. et al., 2010. *Phys. Rev. B* **82:** 125429.

McEnally, C.S., Koylu, U.O., Pfefferle, L.D., Rosner, D.E., 1997. *Combust. Flame* **109** (4): 701-720.

Memon, N. K., Tse, S. D., Chhowalla, M., Kear, B.H., 2013a. *Proc. Combust. Inst.* **34**: 2163–2170.

Memon, N. K., Anjum, D.H., Chung, S.K., 2013b. *Combust. Flame* **160** (9): 1848-1856.

Memarzadeh, S., Tomalchoff, E.D., Phares, D.J., Wang, H., 2011. *Proc. Combust. Inst.* **33**: 1917-1924.

Minutolo, P., Gambi, G., D'Alessio, A., Carlucci, S., 1999. *Atmos. Environ.* **33**: 2725-2732.

Minutolo, P., Commodo, M., Santamaria, A., De Falco, G., D'Anna, A., 2014. *Carbon* **68**: 138-148.

Mu, J., Perlmutter, D.D., 1982. *Thermochimica Acta* **56**: 253-260.

Narsimhan, G., and Ruckenstein, E., 1985. *J. Colloid Interface Sci.* 104 (2): 344-369.

Nemanich, R., Solin, S., 1979. *Phys Rev B* **20**: 392-401.

Ni, M., Leung, M.K.H., Leung, D.Y.C., Sumathy, K., 2007. *Renew. Sustain. Energy Rev.* **11**: 401-425.

Nikraz, S., Phares, D. J., Wang, H., 2012. *J. Phys. Chem. C* **116**: 5342−5351.

Novoselov, K. S., Geim, A. K., Morozov, S. V., Jiang, D., Katsnelson, M. I., Grigorieva, I. V., Dubonos, S. V., Firsov, A. A., 2005. *Nature* **438**: 197-200.

Okuyama, K., Lenggoro, I.W., 2003. *Chem. Eng. Sci.* **58**: 537-547.

Ohsaka, T., Izumi, F., Fujiki, Y., 1978. *J. Raman Spectrosc.* **7**: 321-324.

Pabst, G.W., Martin, L.W., Chu, Y.H., Ramesh, R., 2007. *Appl. Phys. Lett.* **90**: 072902.

Pagliaro, M., 2010. *Nano-Age: How Nanotechnology Changes our Future*, Wiley-VCH, Weinheim.

Pimenta, M.A., Dresselhaus, G., Dresselhaus, M.S., Cancado, L.G., Jorio, A., Saito, R., 2007. *Phys. Chem. Chem. Phys.* **9**: 1276–1291.

Pope, C. J., Marr, J. A., Howard, J. B., 1993. *J. Phys. Chem.* **97**: 11001-11013.

Pratsinis, S. E., 1998. *Prog. Energy Combust. Sci.* **24**: 197-219.

Pratsinis, S. E., Zhu, W., Vemury, S., 1996. *Powder Technol.* **86**: 87–93.

Richter, H., Granata, S., Green, W. H., Howard, J. B., 2005. *Proc. Combust. Inst.* **30**: 1397-1405.

Robertson, J., 2002. *Mat. Sci. Eng. R* **37**: 129-281.

Roth, P., 2007. *Proc. Comb. Inst.* **31**: 1773–1778.

Rybachuka, M., Bell, J.M., 2009. *Carbon* **47**(10): 2481 –2490.

Sader, J.E., Chon, J.W.M., Mulvaney, P., 1999. *Rev. Sci. Instrum.* **70**: 3967-3969.

Sadezky, A., Muckenhuber, H..Grothe, H., Niessner, R., Poschl, U., 2005. *Carbon* **43**: 1731–1742.

Sahm, T., Madler, L., Gurlo, A., Barsan, N., Pratsinis, S. E., Weimar, U., 2004. *Sens. Actuators B*. **98**: 148-153.

Sardar, R., Funston, A.M., Mulvaney, P., Murray, R.W., 2009. *Langmuir* **25:** (24), 13840-13851.

Sayes, C.M., Wahi, R., Kurian, P.A., Liu, Y., West, J.L., Ausman, K.D., Warheit, D.B., Colvin, V.L., 2006. *Toxicol. Sci.* **92**(1):174-185.

Schwarz, J. A., 1995. *Chem. Rev.* **95**: 477–510.

Senden, T. J., 2001. *Curr. Opin. Colloid Interface Sci.* **6**: 95-101

Seo, D. J., Ryu, K. O., Park, S. B., Kim, K. Y., Song, R. H., 2006. *Mater. Res. Bull.* **41**: 359-366.

Serpone, N., Salinaro, A., Horikoshi, S., Hidaka, H., 2005. *J. Photochem. Photobiol. A* **179**: 200–212.

Sgro, L. A., Basile, G., Barone, A. C., D'Anna, A., Minutolo, P., Borghese, A., D'Alessio, A., 2003. *Chemosphere* **51**: 1079–1090.

Sgro, L.A., De Filippo, A., Lanzuolo, G., D'Alessio, A., 2007. *Proc. Combust. Inst.* **31**: 631–638.

Sgro, L.A., D'Anna, A., Minutolo, P., 2010. *Aerosol Sci. Technol.* **44**: 651–662.

Sgro, L.A., D'Anna, A., Minutolo, P., 2011. *Combust. Flame* **158**: 1418–1425.

Shukla, S. K., Parashar, G. K., Mishra, A. P., Misra, P., Yadav, B. C., Shukla, R. K., Bali, L. M., Dubey, G.C., 2004. *Sensor Actuat. B Chem.* **98**: 5-11.

Sirignano, M., Kent, J.H., D'Anna, A., 2010. *Combust. Flame* **157**: 1211-1219.

Sirignano, M., 2012. *Nanoparticle in high temperature environment: experimental techniques and aspect of synthesis properties,* PhD Thesis, University of Naples Federico II, Napoli.

Sirignano, M., D'Anna, A., 2013. *Proc. Combust. Inst.* 34: 1877-1884.

Smijs, T.G., Pavel, S., 2011. *Nanotechnol. Sci. Appl.* **4**: 95-112.

Spicer, P.T., Artelt, C., Sanders, S., Pratsinis, S.E., 1998. *J. Aerosol Sci.* **29**: 647-659.

Spurr, R.A., Myers, H., 1957. *Anal. Chem.* **29**: 760– 762.

SRI International, 2001. *Chemical Economics Handbook*, SRI International, Merlo Park.

Stallinga, P., 2011. *Adv. Mater.* **23**: 3356-3362.

Stark, W.J., Pratsinis, S.E., 2002. *Powd. Technol.* **126**: 103-108.

Stauffer, D., Aharony, A., 1994. *Introduction to percolation theory*, Taylor and Francis, London.

Strobel, R., Baiker, A., Pratsinis, S. E., 2006. *Advanced Powder Technol.* **17** (5): 457-480.

Strobel, R., Pratsinis, S. E., 2007. *J. Mater. Chem.* **17**: 4743-4756.

Tauc, J., 1968. *Mater. Res. Bull.* **3**: 37-46.

Tauc, J., Grigorovici, R., Vancu, A., 1966. *Phys. Stat. Sol.* **15**: 627-637.

Teleki, A., Pratsinis, S. E., Kalyanasundaram, K., Gouma, P. I., 2006. *Sens. Actuators B.* **119**: 683-690.

Tolmachoff, E., Abid, A.D., Phares, D.J., Campbell, C.S., Wang, H., 2009. *Proc. Combust. Inst.* **32**: 1839-1845.

Tolmachoff, E., Memarzadeh, S., Wang, H., 2011. *J. Phys. Chem. C* **115**: 21620−21628.

Touhami, A., Nysten, B., and Dufre, Y. F., 2003. *Langmuir* **19**: 4539-4543.

Truchlý, M., Plecenik, T., Krško, O., et al., 2012. *Phys. C Supercond.* **483**: 61-65.

TSI Incorporated, 2002. *Model 3450 Vibrating Orifice Aerosol Generator-Instruction Manual*, TSI Incorporated, Shoreview.

Tuinstra, F., Koening J.L., 1970. *J. Chem.Phys.* **53**(3): 1126-1131.

Ulrich, G.D., 1984. *Chem. Eng. News.* **62** (32): 22-29.

Vander Wal, R.L., 2000. *Chem*. *Phys*. *Lett*. **324**: 217-233.

Vander Wal, R L., Tomasek, A. J., 2004. *Combust. Flame* **136** (1-2): 129-140.

Vemury, S., Pratsins, S. E., 1995. *Appl. Phys. Lett.* **66**: 3275–3277

Wang, H., 2011. *Proc. Comb. Inst.* **33**: 41-67.

Wang, J.J., Lin, S.Q., Yan, W., Tse, S.D., Yao, Q., 2011. *Proc. Combust. Inst.* **33**: 1925-1932.

Wegner, K., Pratsinis, S. E., 2003. *AIChE J.* **49** (7): 1667–1675.

Wegner, K., Pratsinis, S. E., 2005. *Powder Technol.* **150**: 117–122.

Weir, A., Westerhoff, P., Fabricius, L., Hristovski, K., von Goetz, N., 2012. *Environ. Sci. Technol.* **46**: 2242−2250.

Weisenhorn, A., Maivald, P., Butt, H. J., Hansma, P., 1992. *Phys. Rev. B* **45** (19): 11226-11232.

Winterer, M., 2002. *Nanocrystalline Ceramics: Synthesis and Structure*, Springer-Verlag, Berlin.

Wright, R.B., Varma, R., Gruen, D.M., 1976. *J. Nucl. Mater.* **63**: 415-421.

Yeh, C. L., Yeh, S. H., Ma, H. K., 2004. *Powder Technol*. **145**: 1–9.

Zachariah, M.R., Huzarewicz, S., 1991. *Combust. Flame* **87**: 100-103.

Zhang, H., Banfield, J.F., 1998. *J. Mater. Chem.* **8**: 2073-2076.

Zhang, L.W., Fu, H.B., Zhu, Y.F., 2008. *Adv. Funct. Mater.* **18** (15): 2180-2189.

Zhao, B., Yang, Z., Johnston, M. V., Wang, H., Wexler, A. S., Balthasar, M., Kraft, M., 2003. *Combust. Flame* **133**: 173-188.

Zhao, B., Uchikawa, K., McCormick, J.R., Chen, J., Wang, H., 2005. *Proc. Combust. Inst.* **30**: 2569-2576.

Zheng, F., 2002. *Adv. Colloid Interface* **97**: 255-278.

10. Appendix

Publications on peer-reviewed journals

1. G. De Falco, A. Morgan, M. Commodo, P. Minutolo, A. D'Anna. Flame synthesis of MgO nanoparticles in a FASP reactor. *Materials Research Society Symposium Proceedings* **1506**: 21-26 (2013). *DOI: 10.1557/opl.2013.1052*
2. P. Minutolo, M. Commodo, A. Santamaria, G. De Falco, A. D'Anna. Characterization of flame-generated 2-D carbon nano-disks. *Carbon* **68**: 138-148 (2014). *DOI: 10.1016/j.carbon.2013.10.073*
3. M. Commodo, G. Tessitore, G. De Falco, P. Minutolo, A. D'Anna. Photoionization study of soot precursors nanoparticles in laminar premixed ethylene/ethanol flames. *Combustion Science and Technology* **186** (4-5): 621-633 (2014). *DOI: 10.1080/00102202.2014.883262*
4. G. De Falco, M. Commodo, C. Bonavolontà, G.P. Pepe, P. Minutolo, A. D'Anna. Optical and electrical characterization of carbon nanoparticles produced in laminar premixed flames. *Combustion and Flame* **161** (12): 3201-3210 (2014). *DOI: 10.1016/j.combustflame.2014.05.021*
5. M. Commodo, G. Tessitore, G. De Falco, A. Bruno, P. Minutolo, A. D'Anna. Further details on particle inception and growth in premixed flames. *Proceedings of the Combustion Institute* **35** (2): 1795-1802 (2015). *DOI: 10.1016/j.proci.2014.06.004*
6. G. De Falco, M. Commodo, P. Pedata, P. Minutolo, A. D'Anna. Carbon-TiO_2 Nanostructures: Flame Synthesis and Characterization. *Materials Research Society Symposium Proceedings* **1747** (2015). *DOI: 10.1557/opl.2015.195*
7. G. De Falco, M. Commodo, P. Minutolo, A. D'Anna. Flame-formed carbon nanoparticles: morphology, interaction forces and Hamaker constant from AFM. *Aerosol Science and Technology* **In press** (2015). *DOI: 10.1080/02786826.2015.1022634*

Conference presentations

1. G. De Falco, M. Commodo, P. Minutolo, A. D'Anna. Flame synthesis of metal oxide nanoparticles. *34th International Symposium on Combustion – Warsaw, Poland, August 2012.*
2. G. De Falco, M. Commodo, P. Minutolo, A. D'Anna. Electrical Properties of Carbonaceous Particles Collected from Fuel-Rich Premixed Laminar Flames. *Convegno Nazionale GRICU 2012 – Montesilvano (PE), September 2012.*

3. G. De Falco, A. Morgan, M. Commodo, P. Minutolo, A. D'Anna. Flame synthesis of MgO nanoparticles in a FASP reactor. *XXXV Meeting of the Italian Section of The Combustion Institute – Milan, October 2012.*
4. G. De Falco, M. Commodo, P. Minutolo, A. D'Anna. Scanning Spreading Resistance Microscopy for Electrical Characterization of Flame Generated Particles. *XXXV Meeting of the Italian Section of The Combustion Institute – Milan, October 2012.*
5. G. De Falco, M. Commodo, P. Minutolo, A. D'Anna. Flame synthesis of metal oxide nanoparticles. *MRS Fall Meeting 2012 – Boston, USA, November 2012.*
6. G. De Falco, M. Commodo, A. Santamaria, P. Minutolo, A. D'Anna. Ultrafine nano-TiO_2 produced in a Vapour-Fed Aerosol Flame Reactor. *XXXVI Meeting of the Italian Section of The Combustion Institute – Procida (NA), June 2013.*
7. G. De Falco, M. Commodo, A. Santamaria, G. P. Pepe, P. Minutolo, A. D'Anna. Optical and electrical characterization of carbon nanoparticles produced in laminar premixed flames. *8th Mediterranean Combustion Symposium – Izmir, Turkey, September 2013.*
8. G. De Falco, M. Commodo, P. Minutolo, A. D'Anna. An experimental study of adhesion and attractive forces of different flame-formed carbon nanoparticles using atomic force microscopy. *XXXVII Meeting of the Italian Section of The Combustion Institute – Pisa, April 2014.*
9. G. De Falco, M. Commodo, P. Minutolo, A. D'Anna, Carbon coated TiO_2 Nanostructures: Gas-phase Synthesis and Characterization. *I Congresso Nazionale della Società Italiana di Nanotossicologia – Napoli, June 2014.*
10. G. De Falco, M. Commodo, P. Minutolo, A. D'Anna. Adhesion and attractive forces of flame-formed carbon nanoparticles by Atomic Force Microscopy. *35th International Symposium on Combustion – San Francisco, USA, August 2014.*
11. G. De Falco, M. Commodo, P. Pedata, P. Minutolo, A. D'Anna, Carbon-TiO_2 Nanostructures: Flame Synthesis and Characterization. *MRS Fall Meeting 2014 – Boston, USA, November 2014.*